Ultrafast, Scalable Manufacturing of

Holey Graphene for High-Performance Electrochemical Applications

by

Dini Wang

A Dissertation Presented in Partial Fulfillment
of the Requirements for the Degree
Doctor of Philosophy

Approved April 2021 by the
Graduate Supervisory Committee:

Qiong Nian, Chair
Terry Alford
Qing Hua Wang
Houlong Zhuang

ARIZONA STATE UNIVERSITY

May 2021

ABSTRACT

Nanoholes on the basal plane of graphene can provide abundant mass transport channels and chemically active sites for enhancing the electrochemical performance, making this material highly promising in applications such as supercapacitors, batteries, desalination, molecule or ion detection, and biosensing. However, the current solution-based chemical etching processes to manufacture these nanoholes commonly suffer from low process efficiency, scalability, and controllability, because conventional bulk heating cannot promote the etching reactions. Herein, a novel manufacturing method is developed to address this issue using microwave irradiation to facilitate and control the chemical etching of graphene. In this process, microwave irradiation induces selective heating of graphene in the aqueous solution due to an energy dissipation mechanism coupled with the dielectric and conduction losses. This strategy brings a remarkable reduction of processing time from hour-scale to minute-scale compared to the conventional approaches. By further incorporating microwave pretreatment, it is possible to control the population and area percentage of the in-plane nanoholes on graphene. Theoretical calculations reveal that the nanoholes emerge and grow by a repeating reduction–oxidation process occurring at the edge-sites atoms around vacancy defects on the graphene basal plane. The reduced holey graphene oxide sheets obtained via the microwave-assisted chemical etching method exhibit great potentials in supercapacitors and electrocatalysis. Excellent capacitive performance and electrocatalytic activity are observed in electrochemical measurements. The improvements against the non-holey counterpart are attributed to the enhanced kinetics involving ion diffusion and heterogeneous charge transfer.

TO MY LOVED ONES

ACKNOWLEDGMENTS

I sincerely thank my advisor, Dr. Qiong Nian, for his kind guidance and support for my doctoral study at Arizona State University. I also thank my academic committee members, Dr. Houlong Zhuang, Dr. Qing Hua Wang, and Dr. Terry Alford, for the assistance throughout my research.

I thank all the people who contributed to this research. My lab colleagues, Mr. Rui Dai helped in molecular dynamics calculations, and Mr. Yan Dou and Mr. Kun Bi assisted in materials preparation and electrochemical measurements. Dr. Houlong Zhuang and Dr. Lei Liu offered contributions in density functional theory calculations. Dr. Qing Hua Wang, Dr. Duo Li, Dr. Ximo Chu, and Mr. Yuqi Guo provided helps in Raman spectroscopy. Dr. Yiliang Liao, Dr. Yongfeng Lu, and their group members participated in research-related discussions and helped in reviewing manuscripts.

This research is partially supported by ASU startup funds, NSF grant CMMI-1825576. I would like to acknowledge Diana Convey, David Wright, David Lowry, Emmanuel Soignard, and Shery Chang from the Eyring Materials Center at Arizona State University supported in part by NNCI-ECCS-1542160. They offered helps in materials preparation and characterization.

I thank my parents and my girlfriend for their unconditional support and understanding during my doctoral study.

I thank Science and human's free, rational minds for preventing craziness from dragging us into its swirl many times.

TABLE OF CONTENTS

CHAPTER Page

APPENDIX Page

LIST OF TABLES

Table Page

LIST OF FIGURES

Figure Page

Figure Page

Figure Page

Figure Page

Figure Page

NOMENCLATURE

Abbreviation	Definition
GO	Graphene oxide
rGO	Reduced graphene oxide
pGO	Pretreated graphene oxide
hGO	Holey graphene oxide
rhGO	Reduced holey graphene oxide
rhGO-PS	rhGO with short-time pretreatment
rhGO-PL	rhGO with long-time pretreatment
rhGO-ES	rhGO with short-time etching
rhGO-EL	rhGO with long-time etching
rhGO-M	rhGO with medium-time pretreatment and etching
TMDC	Transition metal dichalcogenide
TMO	Transition metal oxide
LMO	Lithium transition metal oxide
MXene	Transition metal carbides, nitrides, and carbonitrides
LDH	Layered double hydroxide
$EMIMBF_4$/AN	1-Ethyl-3-methylimidazolium tetrafluoroborate/acetonitrile
FEP	Fluorinated ethylene propylene
PC	Propylene carbonate
PMMA	Poly(styrene–block–methyl methacrylate)
PPDA	*p*-Phenylenediamine
PTFE	Polytetrafluoroethylene
PVA	Poly(vinyl alcohol)

SSC	Symmetric supercapacitor
ASC	Asymmetric supercapacitor
FSSC	Flexible symmetric supercapacitor
SSSC	Solid-state supercapacitor
MSC	Micro-supercapacitor
FMSC	Fiber-based micro-supercapacitor
HSC	Hybrid supercapacitor
SEI	Solid electrolyte interphase
OER	Oxygen evolution reaction
ORR	Oxygen reduction reaction
HER	Hydrogen evolution reaction
FET	Field-effect transistor
MACE	Microwave-assisted chemical etching
DFT	Density functional theory
MD	Molecular dynamics
AFM	Atomic force microscopy
BET	Brunauer–Emmett–Teller
FWHM	Full width at half-maximum
TEM	Transmission electron microscopy
XPS	X-ray photoelectron spectroscopy
EDLC	Electrical double-layer capacitor
GCE	Glassy carbon electrode
RHE	Reversible hydrogen electrode
CV	Cyclic voltammetry

GCD	Galvanostatic charge and discharge
EIS	Electrochemical impedance spectroscopy
CPE	Constant phase element

PREFACE

One of the most apparent demands in the internet era is the lighter, smaller, more efficient, and intelligent devices. Two-dimensional materials are playing a vital role in this new technology revolution. Recently, holey graphene has become a hot topic in material research. It enhances the versatility of graphene and broadens the application range. In-plane nanoholes on holey graphene improve both mass transport and charge transfer and also bring a new dimension for nanomodification. The electrochemical application is the primary field of holey graphene research, while the effective, controllable, and fast manufacturing of holey graphene is still a big challenge. Through a year's effort, my advisor, Dr. Qiong Nian and I were very excited to preliminarily confirm the feasibility of utilizing microwave-assisted chemical etching to achieve the ultrafast, controllable manufacturing of holey graphene. Starting then, I began to fully dedicate myself to the systematic research on this topic until this dissertation was finished.

The presented dissertation is composed of six chapters. It starts with a thorough introduction of the holey graphene research and the microwave–graphene interaction. Chapter 2 describes the experimental procedures and calculation methods. Chapter 3 presents the ultrafast, controllable manufacturing of holey graphene using the microwave-assisted chemical etching method. Chapter 4 probes the graphene–microwave interaction in the solution-based environment. Chapter 5 demonstrates the improvement in electrochemical energy storage and electrocatalytic activity, respectively, by effectively tuning the properties of holey graphene by the microwave-assisted chemical etching method. Chapter 6 concludes the research.

Dini Wang

March 31, 2021 in Xiangtan

CHAPTER 1

INTRODUCTION

1 Holey Two-dimensional Materials

The rise of two-dimensional (2D) materials launches a new wave of the science and technology revolution in a wide range of fields, involving energy storage and conversion, electronics, biochemistry, biomedicine, and environmental applications.[1, 2, 3] The large specific surface area of 2D materials increase the utilization ratio and makes lighter and smaller devices becoming possible. The atomic-level thickness of 2D materials makes them very versatile to fit in various applications by encapsulating, wrapping, sandwiching, directly mixing with, or stacking as building blocks with other materials to obtain diverse nanostructures with both high performance and complex functions. These materials also exhibit distinct and unusual properties with their thickness decreasing down to atomic thin, e.g., the quantum hall effect, spin–valley locking effect, which can be employed to fabricate novel devices.

Although the history of 2D materials is still relatively short, the next stage of research, nanomodification of 2D materials, has already begun. It involves heteroatom doping, attachment of functional groups, anchoring of nanoparticles, nanowires, or nanofibers, immobilization of enzymes and biomolecules, defect control, topological manipulation, magic-angle stacking, etc.[4, 5, 6, 7] Nanomodification of 2D materials improves the crucial properties to enhance the application performance, further broadens the application range of 2D materials, or even embarks new research areas and branches. Meanwhile, new types of nanomodification are constantly emerging.

An increasing number of studies show that after creating nanoholes on the basal plane, the 2D materials can exhibit better performance than their pristine forms and become

more versatile to realize various functions.[8, 9, 10, 11] With nanoholes, these holey 2D materials possess much more mass transport channels, which are significant for the applications relying on the mass exchange process, e.g., batteries, biosensors, and desalination devices. Moreover, the edge-sites of the nanoholes can exhibit much higher electrochemical activity than the in-plane sites to further improve the performance. More importantly, holey 2D materials can broaden the versatility or application range by providing a whole new dimension of structural diversity. They enable obtaining the desired properties for distinctive applications by tuning multiple structural variations, such as

i) the diameter, population, and distribution pattern of nanoholes;

ii) the number, alignment, and heteroatom doping of the edge-site atoms around nanoholes;

iii) the interactions between nanoholes and foreign nanomaterials.

The current family of holey 2D materials (**Figure 1**) mainly includes graphene, transition metal dichalcogenides (TMDCs), transition metal oxides (TMOs), lithium transition metal oxides (LMOs), transition metal carbides, nitrides, and carbonitrides (MXene), layered double hydroxides (LDHs), nitrogenated carbon (C_2N), phosphorene (the monolayer of black phosphorus), and hexagonal boron nitride (h-BN). The research on holey 2D materials covers the field of supercapacitors, metal-ion batteries, Li–S batteries, metal–air batteries, metal–CO_2 batteries, water splitting, thermocells, ion detection, desalination, biosensors, drug carriers, and various electronic devices.

2 Holey Graphene and Its Applications

Graphene is the most representative material among 2D materials with its attractive properties, including high strength and stiffness, high electrical and thermal conductivity, and high specific surface area.[12] It has been leading the surging development of nanotechnologies

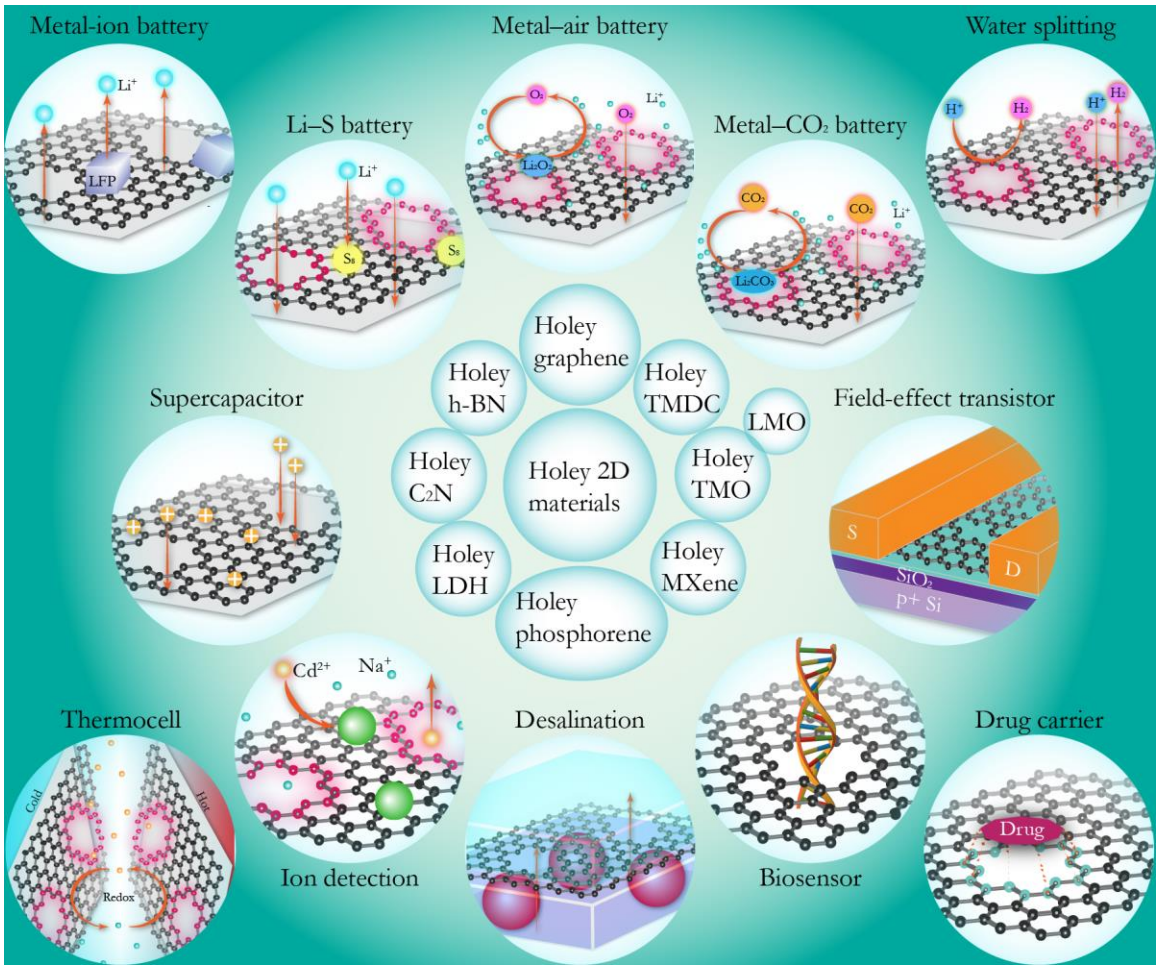

Figure 1. Current Family of Holey 2D Materials, Including Graphene, Transition Metal Dichalcogenides (TMDCs), Transition Metal Oxides (TMOs), Lithium Metal Oxides (TMOs), Two-dimensional Transition Metal Carbides, Nitrides, and Carbonitrides (MXene), Phosphorene, Layered Double Hydroxides (LDHs), Nitrogenated Carbon (C_2N), and Hexagonal Boron Nitride (h-BN), and Schematics of Their Applications in Metal-ion Batteries, Li–S Batteries, Metal–Air Batteries, Metal–CO_2 Batteries, Water Splitting, Supercapacitors, Field-effect Transistors, Thermocells, Ion Detection, Desalination, Biosensors, and Drug Carriers.

since its discovery in 2004.[13, 14, 15, 16] Now, it is estimated that the volume of sales related to graphene and its derivatives can reach 100 million USD.[17]

Holey graphene is the graphene with holes on its basal plane (**Figure 2**). The holes are mostly in nanoscale or sub-nanoscale and can be randomly or periodically distributed. The nanoholes allow ions and molecules to directly pass through the graphene basal plane. This characteristic fascinates the researchers to use it in enhance the mass transport kinetics

of various applications. Also, the nanoholes change the electronic structure of pure graphene, introducing a new handle to tune the electronic properties of graphene and making this material more useful in semiconducting applications. Besides the nanoholes themselves, the edge-sites carbon atoms by nanoholes are also an essential feature of holey graphene. They are more chemically active than those in the defect-free regions and better in charge transport. Moreover, they can be doped or attached by heteroatoms, functional groups, nanoparticles, or nanostructures to obtain distinct properties while retaining the superior properties of pure graphene. The versatility of the edge-sites encourages the development of new holey graphene applications involving electrochemistry, catalytic chemistry, biochemistry, electronic, optoelectronic, thermoelectric, etc.

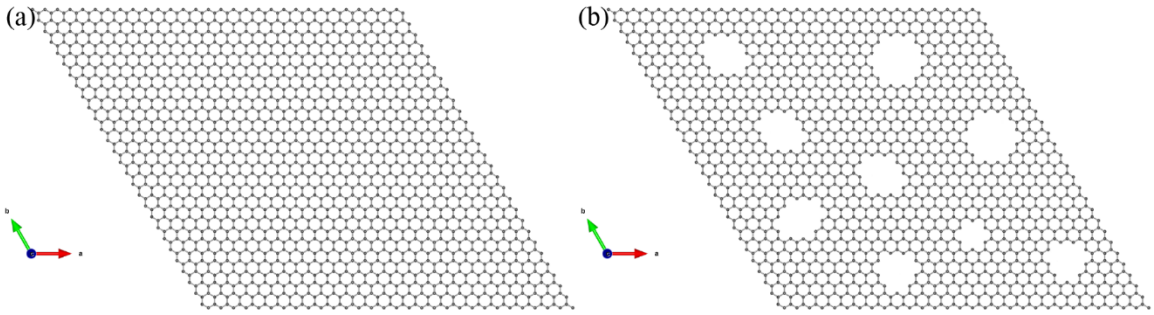

Figure 2. Crystalline Structures of (a) Graphene and (b) Holey Graphene.

Although the research of holey graphene does not have a long history, it has seen a significant surge of progress in recent years. This material was first reported and prepared by J. Bai et al.[18] in 2010 to provide a semiconductive graphene structure that could replace graphene nanoribbons in field-effect transistors. The material was referred to as graphene nanomesh at that time because of the periodic pattern of the nanoholes. The periodic distribution of nanoholes with controlled diameters and neck widths were significant factors affecting the in-plane charge transport of graphene in 2D field-effect transistors. In 2011, X. Zhao et al.[19] first proposed making graphene holey for the energy storage devices with

enhanced performance. They demonstrated that compared to that of pure graphene, the faster cross-plane ion diffusion brought by the nanoholes overcame the restacking issue of graphene and resulted in better lithium-ion storage and power delivery. These two studies enlightened researchers to further discover the great potential of holey graphene and embarked on the exponential growth of studies on this fascinating material.

2.1 Supercapacitors

Supercapacitors highlight the advantage in power delivery due to the rapid charge and discharge processes on electrodes and have become a complementary energy storage solution for batteries, which show a bottleneck in further promoting the power density. Nevertheless, supercapacitors generally have relatively low energy storage, and therefore the improvement of the energy density is vital to promote their application. Based on the charging mechanism, supercapacitors can be divided into three groups: electrical double-layer capacitors (EDLCs), pseudocapacitors, and hybrid capacitors.[20] In EDLCs, the charging is fulfilled by the electrostatic adsorption of electrolyte ions on the electrode surface without exchanging charges (i.e., the non-faradaic process). Pseudocapacitors are charged by exchanging charges with the electrolyte through redox reactions (i.e., the faradaic process). The different charging mechanisms generally make the EDLCs more reversible and possessing longer cycling life. In contrast, the pseudocapacitors are less reversible but have larger specific capacitance. Thus, the requirements for the electrode materials of the two supercapacitors are also different. For EDLCs, the specific surface area of the electrode material is a predominant factor affecting the specific capacitance, while for pseudocapacitors, the electrochemical activity, which can be characterized by charge transfer resistance, of the electrode material is also a significant factor besides the specific surface area. Hybrid capacitors refer to the supercapacitors that combine the above two charging

mechanisms. In a different context, it can also mean the energy storage devices coupled by a supercapacitor-type electrode and a battery-type one (e.g., lithium-ion capacitors) to introduce the crystalline-confined charging process.

Graphene has been broadly used in the research of novel supercapacitors due to its high specific surface area and electrical conductivity. The studies on holey graphene fast spread in this field. In a supercapacitor, holey graphene can be used as the electrode material, the conductive additive incorporating with other capacitive materials, or the three-dimensional (3D) freestanding framework in the form of aerogels to provide hierarchical porous structures. The EDLC and pseudocapacitor charging mechanisms (**Figure 3**a,b) coexist in holey graphene-based supercapacitors, contributed by the larger accessible surface area enabled by nanoholes and the lower charge transfer resistance resulted from the edge-site atoms around nanoholes. Pseudocapacitance can be further enhanced by heteroatom doping, functional group modification, polymer modification, transition metal compound incorporation, etc. **Appendix A** summarizes the crucial data of holey graphene-based supercapacitors reported in recent years.

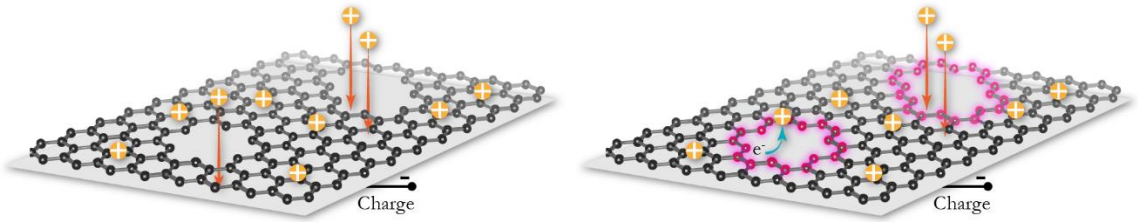

Figure 3. Schematics of Energy Storage Mechanisms of Holey Graphene Supercapacitors: (a) Electrical Double-layer Capacitor and (b) Pseudocapacitor.

2.1.1 Electrode Property

To preliminarily evaluate the energy density, the specific capacitance of the electrode material is a major indicator. So far, the highest reported specific capacitance of pure holey graphene is 330 F g^{-1} at a scan rate of 5 mV s^{-1} in the butyl methyl pyrrolidinium–

dicyanamide ionic liquid electrolyte, about 1.4 times that of pristine graphene (235 F g^{-1}).[21] In aqueous electrolytes, the highest record of pure holey graphene is 329 F g^{-1} at a current density of 0.5 A g^{-1}, about 1.5 times that of pristine graphene (208 F g^{-1}).[22] In organic electrolytes, the highest record of pure holey graphene is 298 F g^{-1} at a current density of 1 A g^{-1} in the $EMIMBF_4$/AN electrolyte.[23] Doping holey graphene with heteroatoms, such as B, N, S, and P, the specific capacitance can be improved mostly because of the higher contribution from the pseudocapacitance, which provides more energy storage chemically through the redox reactions between the electrode material and electrolyte ions. The highest reported value of the heteroatom-doped holey graphene is 362 F g^{-1} at a current density of 1 A g^{-1} (B, N, and P co-doped holey graphene). Under the same doping level, the non-holey version showed a lower value of 318 F g^{-1}.[24] To prevent restacking, graphene can be modified by the crosslinking molecules, such as *p*-phenylenediamine. The specific capacitances of *p*-phenylenediamine incorporated holey and pristine graphene are 375.5 and 311.8 F g^{-1} at a current density of 0.5 A g^{-1}, respectively.[25] The addition of carbon nanotubes can achieve the same goal while enhancing the electric conductivity of the electrode, bringing a specific capacitance of 557 F g^{-1} at a current density of 0.5 A g^{-1}.[22] Some polymers including polyaniline and polypyrrole can contribute pseudocapacitance to enhance the specific capacitance with the highest reported value of 746 F g^{-1} at a current density of 1 A g^{-1}, higher than that of the non-holey version reported in the same paper (618 F g^{-1}).[26] Transition metal compounds, including oxides, dichalcogenides, MXene, are employed to endow higher pseudocapacitance to holey graphene. The highest reported specific capacitance for these nanocomposite electrodes is 693 F g^{-1} at a scan rate of 2 mV s^{-1}, obtained by the RuO_2-incorporated holey graphene fiber.[27] Due to the ability of holey graphene in realizing the electrodes with higher packing densities without much performance

sacrifice, the volumetric specific capacitances of holey graphene-based electrode materials are also significantly higher than those of non-holey versions. The highest reported volumetric specific capacitances of pure,[28] heteroatom-doped,[29] crosslinked,[30] polymer-incorporated,[31] and transition metal compound-incorporated[32] holey graphene are 165, 807, 516, 1,058, and 1,445 F cm^{-3}, respectively.

2.1.2 Device Performance

Compared to the electrode performance, the device performance is closer to the actual application and generally evaluated by the energy and power densities of a full supercapacitor device, which are more reliable than the specific capacitance measured from a single electrode and more comparable across different papers due to the generally acknowledged calculation method.[33] Based on the distinct requirements on the application end, the holey graphene-based supercapacitors can be further categorized into more groups, including the symmetric supercapacitor (SSC), asymmetric supercapacitor (ASC), flexible symmetric supercapacitor (FSSC), solid-state supercapacitor (SSSC), micro-supercapacitor (MSC), fiber-based micro-supercapacitor (FMSC), and hybrid supercapacitor (HSC).

The SSC is the most common supercapacitor device and made of two identical electrodes with a separator. The highest reported energy density in holey graphene-based SSCs is 124 Wh kg^{-1} at a power density of 18.0 W kg^{-1}, about 1.4 times that of pristine graphene (86 Wh kg^{-1} with 17.5 W kg^{-1}).[21] The capacitance retained 90% after 2,000 charge and discharge cycles. The SSC in this study employed the butyl methyl pyrrolidinium–dicyanamide ionic liquid electrolyte, which also led to the higher performance stability of the SSC under elevated temperatures. The energy and power densities of the SSC at 60 °C increased to 140 Wh kg^{-1} and 52.5 W kg^{-1}, respectively. A similar magnitude of energy densities is reported by Y. Xu et al.[34] Generally, without trading off the power density and

keeping it at higher than 10^3 W kg^{-1}, the energy densities of the holey graphene-based SSCs are in the magnitudes of 10^0–10^1 Wh kg^{-1}. Under an ultrahigh level of power densities (10^4 W kg^{-1}), the highest reported energy density is 38.5 Wh kg^{-1} at a power density of 83,000 W kg^{-1} using 1 M 1-ethyl-3-methylimidazolium tetrafluoroborate/acetonitrile ($EMIMBF_4$/AN) electrolyte.[24] In terms of volumetric properties, the highest volumetric energy density of the holey graphene-based SSCs is 87 Wh L^{-1} with a volumetric power density of 10^2 W L^{-1} achieved in an $EMIMBF_4$/AN electrolyte with an ultrahigh electrode density of 10 mg cm^{-2}.[23] When the volumetric power density of the holey graphene-based SSC is higher than 10^3 W L^{-1}, the highest reported volumetric energy density is 31.3 Wh L^{-1} using the MXene/holey graphene nanocomposite electrode.[32]

Unlike an SSC, an ASC is generally composed of an EDLC electrode (e.g., activated carbon and mesoporous carbon spheres) and a pseudocapacitive electrode (e.g., MnO_2 and Co_3O_4) aiming to provide a better energy density than an SSC while maintaining a favorable power density. Graphene was often used as the conductive additive in the pseudocapacitive electrode and a framework material with a high specific surface area, and the graphene-based nanocomposite electrode generally exhibited superior performance than the electrode solely made of pseudocapacitive metal oxides.[35] Holey graphene can be used in the same manner with the expectation of bringing better performance than pristine graphene due to the faster ion transport behavior. However, as far as we know, there is no study on the holey graphene-based ASC yet.

An FSSC is a flexible version of an SSC and has become increasingly demanded with the fast development of portable, wearable, and foldable electronic devices. Besides the energy and power densities, the performance stability of an FSSC under high-angle distortion is a critical factor in evaluating the electrode material. 2D nanomaterials, especially

graphene, have natural advantages in terms of flexibility. Thus, holey graphene is highly promising in this field. P. Du et al.[25] reported a holey graphene-based FSSC, which showed energy densities of 5.59–11.71 Wh kg^{-1} at power densities of 249–20,110 W kg^{-1} and maintained 74% of its initial specific capacitance after 5,000 cycles at a high current density of 10 A g^{-1}. Most importantly, the cyclic voltammetry of the FSSC showed little changes under bending and twisting, as well as after restoring to its original flat status. After bending to 180° for 250 cycles, the device kept 85% of its initial capacitance. Z. Pan et al.[24] fabricated an FSSC using the B, N, and P co-doped holey graphene hydrogel as the electrode, which showed little changes in the cyclic voltammetry under bending at 60°, 120°, and 180°, and the device retained 91.6% of its initial specific capacitance after 20,000 cycles under 180° bending. Y. Xu et al.[34] reported a holey graphene FSSC with negligible changes in the cyclic voltammetry under bending with curvature radii of 2–12 mm, and the specific capacitance retained 90% after 20,000 cycles under 2-mm bending.

Because of using solid-state electrolytes (mainly polymer-based gels), the SSSC not only inherit the high power density of the SSC and also avoid the leakage of harmful electrolytes, thus making them promising in wearable devices and appliable in other supercapacitors including FSSCs[24, 25, 34] and MSCs[36]. A. C. Lokhande et al.[37] fabricated a holey graphene-based SSSC using poly(vinyl alcohol) (PVA)/KOH gel electrolyte. The device exhibited energy densities of 9.25–10.37 Wh kg^{-1} at power densities of 1388–4166 W kg^{-1}. M. Kotal et al.[29] fabricated an SSSC using the sulfur and nitrogen co-doped holey graphene aerogel as the electrode and PVA/LiCl gel as the electrolyte. The holey graphene SSSC exhibited an areal energy density of 17.4 μWh cm^{-2} at a power density of 4,457 μW cm^{-2}, higher than that of the non-holey version (11.1 μWh cm^{-2} at 3,134 μW cm^{-2}), and also a higher power density at the same energy density. The holey graphene SSSC retained 95.7%

of its initial areal capacitance after 1,100 cycles. This study also investigated the structurally resilient solid-state supercapacitor (SRSS) based on holey graphene. The areal capacitance of the SRSS was only 7 mF cm^{-2} less than that of the SSSC at the same current density of 1 mA cm^{-2}, and it increased by 3% and 3.12% even under high compression of 50% and 85%, respectively.

MSCs are thin-layer energy storage devices possessing many advantages over micro-batteries and have great potential as the energy storage component of fast-developing wearable electronics. An MSC is composed of alignments of two or more 2D micro-electrodes deposited or printed on a substrate. Holey graphene offers extraordinary areal energy density because the holey structure allows the relatively thicker electrode films without compromising the rate performance while maintaining flexibility. A. Lu et al.[36] reported a holey graphene MSC using the PVA/H_2SO_4 gel electrolyte, exhibiting volumetric energy densities of 2.43–4.24 Wh L^{-1} at a power density of 120–21,840 W L^{-1}, and the device retained 88.6% of its initial specific capacitance after 10,000 cycles.

FMSCs are state-of-the-art fiber devices that can be further fabricated as the clothes and textiles providing energy for the wearable electronics or storing energy from the thin-film energy harvest devices. Holey graphene is an excellent material for this application due to the simultaneous need for high packing density (or mass loading) and rate capability. S. Zhai et al.[27] reported an FMSC using the RuO_2 nanoparticle (Ru content: 42.5%) decorated holey graphene fiber as the electrode. The fiber diameter was about 38 μm. With a high mass loading of 1.52 g cm^{-3}, the FMSC exhibited high volumetric energy densities of 15.9–27.3 Wh L^{-1} at the power density of 147.7–2,954.1 W L^{-1}, and the specific capacitance of the device retained 78.7% of its initial value after 10,000 cycles. C. Wang et al.[38] fabricated an FMSC using the MoS_2 decorated holey graphene fiber electrode, which has a core of

graphite fiber bundles. The fiber diameter was about 173 μm. The FMSC showed energy densities of 4.1–8.2 Wh L^{-1} at the power density of 40–2,000 W L^{-1}, and the device retained 92% of its initial specific capacitance after 3,000 cycles.

An HSC is similar to an ASC, but the difference is that the ASC often refers to a capacitor combining an EDLC electrode and a pseudocapacitive one, while the HSC generally specifies a battery-like capacitor, which has a well-defined anode and cathode, a capacitor-type one and a battery-type one (**Figure 4**). Holey graphene was proved effective in enhancing the performance of both of the electrodes in an HSC. Besides improving the capacitor-type electrode (as discussed above), holey graphene has great potential in improving the battery-type electrode due to its contribution to the ion diffusion rate, which is a major limitation of the battery-type electrode towards higher power capability. J. H. Jeong et al.[39] fabricated an HSC using a holey graphene cathode and a $Li_4Ti_5O_{12}$/holey graphene anode. The device exhibited energy densities of 43.1–117.3 Wh kg^{-1} at power densities of 100–19,700 W kg^{-1}, higher than those with the non-holey crumpled rGO and its nanocomposite. The simultaneous improvements of the energy and power densities are attributed to the high specific capacitance of the holey graphene cathode and the high rate capability of the holey graphene-based anode. The HSC retained 89.7% and 81.7% of its initial specific capacitance after 1,000 and 2,000 cycles at 2 A g^{-1}.

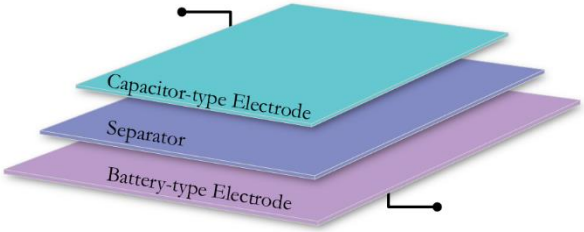

Figure 4. Schematic of the Hybrid Supercapacitor Composed by a Capacitor-type and a Battery-type Electrode.

2.1.3 Factors Contributing to The Performance Improvement

According to the studies on holey graphene-based supercapacitors, the superior electrochemical properties of holey graphene against pristine graphene are coming from the improvements in two aspects: i) the number of ion diffusion channels (**Figure 5**a) and ii) the number of electrochemically active sites (**Figure 5**b). The two aspects further affect the kinetics of ion diffusion and charge transfer, respectively.

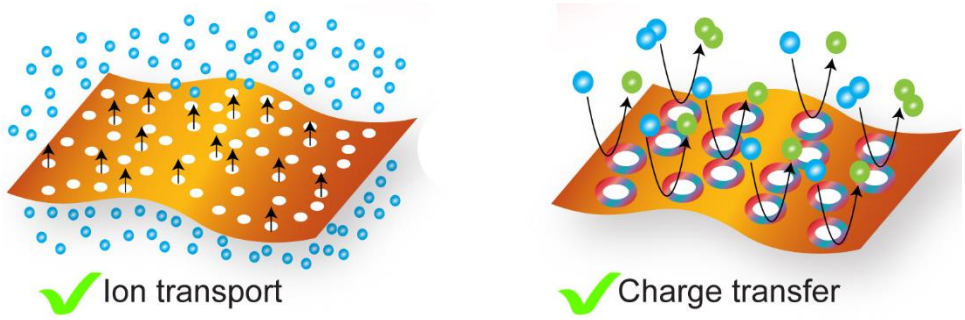

Figure 5. Mechanisms of Performance Enhancements Brought by Nanoholes On Holey Graphene: (a) Ion Transport and (b) Charge Transport Enhanced by Nanoholes and Edge-site Atoms Around Nanoholes.

2.1.3.1 Enhancement of Ion Transport

The nanoholes bring a larger number of ion diffusion channels and, therefore, a larger surface area can be accessible to the electrolyte ions. From a perspective of the process, the nanoholes create more through-the-plane channels for ion transport inside the electrode, thus promoting the kinetics of the electrochemical process. From a perspective of the result, the electrolyte ions can pass through the diffusion channels to the nanosheets that stay deep in the electrode so more nanosheets can participate in the energy storage process.

The current studies on holey graphene generally lack a deeper investigation of ion diffusion kinetics. S. Zhai et al.[27] reported the holey graphene fiber exhibited an ion diffusion rate of 1.33×10^{-15} cm^2 s^{-1}, higher than that of the RuO_2 (42.5 wt.%) decorated holey

graphene fiber electrode (8.80×10^{-15} cm^2 s^{-1}). However, they did not compare the ion diffusion rate between holey graphene and pristine graphene.

Many studies demonstrated the improvement in the specific surface area brought by the nanoholes. Y. Bai et al.[40] reported that the Brunauer–Emmett–Teller (BET) surface area of reduced holey graphene oxide was 763 m^2 g^{-1}, and that of the reduced non-holey graphene oxide sheets reported in the same paper was only 552 m^2 g^{-1}. Note that the products were degassed under 180 °C for 12 h before the nitrogen adsorption/desorption measurements. C. Yang et al.[21] reported that the reduced holey graphene oxide powder obtained via annealing in argon exhibited BET surface areas of 750 and 800 m^2 g^{-1} for annealing temperatures of 300 and 1100 °C, respectively, while that of the non-holey counterpart was 550 m^2 g^{-1}. For 3D holey graphene frameworks, Y. Xu et al.[23] reported the BET surface area of the freeze-dried holey graphene framework was 830 m^2 g^{-1}, while that of the non-holey counterpart was only 260 m^2 g^{-1}. The specific surface areas characterized by the methylene blue adsorption/desorption were consistent with the BET results, 1,560 and 1,030 m^2 g^{-1} for the freeze-dried holey graphene framework and the non-holey counterpart. For heteroatom doped holey graphene, a record high BET value was 1,216 m^2 g^{-1} from a study on N-doped holey graphene sheets by Z. Jiang et al.[41] That of the non-holey counterpart in the same paper was 630 m^2 g^{-1}. M. Kotal et al.[29] reported that the BET surface area of the N,S-doped holey graphene aerogel was 395 m^2 g^{-1}, and that of the N,S-doped graphene aerogel prepared via the same conditions was only 183 m^2 g^{-1}. Another study by Z. Pan et al.[24] showed that the B,N,P-doped holey graphene aerogel had a BET surface area of 980 m^2 g^{-1}, 2 times of that of the non-holey counterpart. Similar results on the specific surface area of holey graphene for supercapacitors can be found in **Appendix A**.

With the improvement in ion diffusion brought by the nanoholes, it is possible to fabricate thicker or denser devices. E. D. Walsh et al.[42] reported that the areal capacitance of the holey graphene electrode showed a near-linear increase with the areal mass loading ranging ~1–30 mg cm^{-2} at high current densities up to 30 mA cm^{-2}. Z. Pan et al.[24] fabricated a high-mass-loading supercapacitor (10 mg cm^{-2}) by B,N,P-doped holey graphene aerogels delivering ultrahigh gravimetric and volumetric energy densities of 38.5 Wh kg^{-1} and 57.4 Wh L^{-1} with ultrahigh power densities of 83 kW kg^{-1} and 55 kW L^{-1} and a long cycle life (81.3% retention after 50,000 cycles). A Ti_3C_2 MXene@holey graphene symmetric supercapacitor reported by Z. Fan et al.[32] retained a volumetric capacitance of 998 F cm^{-3} at an ultrahigh mass loading of 12.6 mg cm^{-2}. In contrast, the pure graphene version of this material had only about 400–500 F cm^{-3}. The enhanced ion transport kinetics also leads to the realization of hybrid energy storage devices that combine the advantages of supercapacitors and batteries with both high energy and power densities. H. Sun et al.[43] manufactured a 3D holey graphene/Nb_2O_5 composite with highly efficient electrode kinetics. It was used to fabricate a high mass loading electrode, which exhibited high energy densities without compromising the rate performance. At a high mass loading of 11 mg cm^{-2}, it showed a specific capacity of 139 mAh g^{-1} at a high rate of 10 C, which was only 7% less than that of the low-mass loading electrode (1 mg cm^{-2}). The composite exhibited specific capacity retention of 93%, with the mass loading changing from 1 to 11 mg cm^{-2}, while the graphene/Nb_2O_5 composite showed only 61%.

2.1.3.2 Enhancement of Charge Transfer

Holey graphene improves the charge transfer resistance, leading to faster kinetics during the charge and discharge process at the electrode–electrolyte interface. Y. Xiang et

al.[44] shows that the charge transfer resistance of the nanocomposite of a lithium titanate and holey graphene is a quarter of that of the one with pristine graphene.

The nanoholes enhance further nanomodification of holey graphene. P. Xu et al.[45] compared the specific surface area, conductivity, and electrochemical capacitance of holey graphene aerogel and holey N-doped graphene aerogel and found that N doping effectively improved all the three properties of holey graphene aerogel. X. Ye et al.[30] added *p*-phenylenediamine (PPDA) molecules in between holey graphene sheets, which avoided restacking and exhibited both high gravimetric and volumetric capacitances of 300 F g^{-1} and 516 F cm^{-3} at 0.5 A g^{-1}. In comparison, pristine graphene had only 235 F g^{-1} and 357.2 F cm^{-3}. The FSSC assembled using this material showed energy and power densities of 2.18–2.72 Wh L^{-1} and 146.5–3,313.6 W L^{-1} with a total volume of 3.8–4.2 × 10^{-3} cm^{-3}.

The coupling effect of holey graphene and active materials is an intriguing phenomenon. Research shows that the nanocomposite composed of both metal oxides and holey graphene can bring performance even higher than the sum of each material.[44]

2.2 Metal-ion Batteries

Metal-ion batteries are mainly based on Li-, Na-, K-, and Mg-ions. In metal-ion batteries (**Figure 6**), holey graphene can be directly used as the anode material, incorporate with TMOs to prepare the anode material, or incorporate with LMOs to prepare the cathode material. Either way, holey graphene brings better specific capacity, rate capability, and cycling performance. The crucial data of the electrode and device performance of the holey graphene-based metal-ion batteries are summarized in **Appendix B**.

D. Wu et al.[46] reported a nanocomposite Li-ion battery electrode composed of hollow Co_3O_4 particles and holey graphene sheets, which exhibited an improvement of about 1.5 times in the specific capacity (631 mAh g^{-1}) at a high current density of 10 A g^{-1}

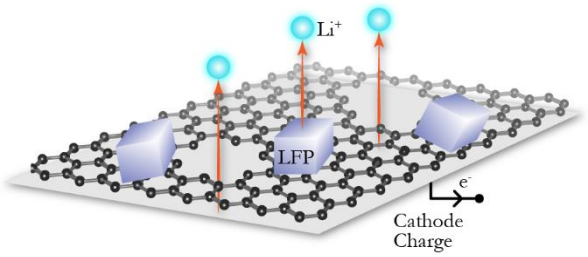

Figure 6. Schematic of Holey Graphene-based Metal-ion Batteries: Charge Process of a Holey Graphene–$LiFePO_4$ Cathode.

compared to the electrode using regular graphene (406 mAh g^{-1}). After 250 cycles at 0.2 A g^{-1}, the discharge capacity of the former was about 1.3 times higher than that of the latter (1,015 and 762 mAh g^{-1}, respectively). When assembled as the anode in a lithium-ion battery with a $LiFePO_4$ cathode, the energy and power densities were 353 Wh kg^{-1} and 1,370 W kg^{-1}, respectively. As the electrode of sodium-ion batteries, holey rGO exhibited the capacity of 365 mAh g^{-1} at 0.1 A g^{-1}, while rGO had only 251 mAh g^{-1}.[47]

It is a common concern that the volumetric specific capacity of the battery might be compromised when adding low-density porous materials like graphene. The same concern falls upon holey graphene. Nevertheless, studies have shown that the gravimetric and volumetric specific capacities can be improved simultaneously. Y. Xiang et al.[44] reported a lithium titanate ($Li_4Ti_5O_{12}$)–holey graphene nanocomposite. At a low current density of 0.035 A g^{-1}, it had a specific capacity of 200 mAh g^{-1} based on the weight of $Li_4Ti_5O_{12}$, which was higher than that of the one with pristine graphene (190 mAh g^{-1}). At higher current densities up to 7 A g^{-1}, the former still retained 78%, and the latter had lost almost all the capacity. A similar trend was found in the change of the volumetric specific capacity, and the $Li_4Ti_5O_{12}$–holey graphene nanocomposite retained 98 mAh cm^{-3} at 17.5 A g^{-1}.

From a perspective of the device fabrication process, holey graphene enables the fabrication of binder-free graphene structures with densities notably higher than that of

pristine graphene. This is because holey graphene allows gases to escape from the powder mixture during compressing. D. Kirsch et al.[48] reported the free-standing, binder-less holey graphene–$LiFePO_4$ electrode by roll-to-roll dry compression with a high areal mass loading of 11.6 mg cm^{-2}. X. Han et al.[49] used holey graphene to achieve the manufacturing of graphene monolithic architectures with a high density of 1.4 g cm^{-3} while maintaining the outstanding specific mechanical strength (18 MPa cm^3 g^{-1}), electric conductivity, (13,000 S m^{-1}) and thermal (20,000 W K^{-1}) conductivity. Nevertheless, the study did not show the energy storage performance of the high-density holey graphene disk.

In batteries, a faster ion diffusion rate can be more beneficial to performance than a higher conductivity within a certain range. D. Wu et al.[46] found that the capacity of the nanocomposite of hollow Co_3O_4 and holey graphene was much higher than that of the one using nitrogen-doped graphene, which possessed even higher conductivity than pristine graphene. Y. Xiang et al.[44] indicated that the ion diffusion coefficient of lithium ions in the holey graphene-based nanocomposite (10^{-10} cm^2 s^{-1}) was two orders of magnitude higher than that in the pristine graphene-based one (10^{-12} cm^2 s^{-1}), which was one order of magnitude lower than the blank active material (10^{-11} cm^2 s^{-1}). The result also suggested that the graphene without in-plane nanoholes strongly hindered the ion transport in the electrode of batteries. Molecular dynamics simulations indicated that holey graphene brought a higher lithium-ion diffusion coefficient than pristine graphene and improved the uniformity and quality of the solid electrolyte interphase (SEI) layer.[50]

2.3 Metal–Air Batteries

Metal–air batteries, such as the Li–air and Zn–air batteries, are attractive energy storage devices due to the ultrahigh theoretical capacity (about 3500 Wh kg^{-1} for Zn–air). The operation of these batteries relies on the oxygen reduction reaction (ORR) and the

oxygen evolution reaction (OER) processes occurring on the air cathode, which is currently made of Pt/C. Due to its favorable electrochemical activity, holey graphene is introduced in these applications to reduce the cost of the electrode and improve the ORR and OER performance.

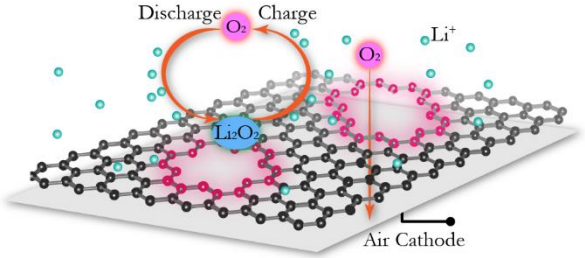

Figure 7. Schematic of Holey Graphene as the Oxygen Evolution Reaction and Oxygen Reduction Reaction Platform for Metal–Air Batteries.

D. Yu et al.[51] reported that the N-doped holey graphene aerogel was comparable to the Pt/C electrode in both the oxidation of hydrazine and ORR. Y. Bian et al.[52] prepared N-doped holey graphene with a specific surface area of 1170.05 $m^2 g^{-1}$ and 5.1 at.% N doping. The ORR performance of this material (an onset potential of 0.91 V and a half-wave potential of 0.833 V) was higher than N-doped rGO and close to the Pt/C electrode. P. Du et al.[53] found that the ORR and OER performance of N,Mo-doped holey graphene was better than not only N,Mo-doped graphene but also Pt/C. They discovered that the higher number of nanoholes promoted the onset and half-wave potentials in the ORR process. In OER process, the nanoholes enhanced both the electrochemical surface area and the heteroatom doping. The Zn-air battery with this material as the air cathode exhibited higher maximum power density and discharge voltage and better cycling stability than the Pt/C–IrO_2-based batteries. W. Kong et al.[54] reported a Co,N-codoped holey graphene aerogel which exhibited ORR activity comparable to the commercial Pt/C electrode due to efficient mass transport and abundant active sites around holey and doped areas. $Co_{5.47}N$@holey N-

graphene[55] exhibited high catalytic activity for both ORR and OER due to the holey structure and strong connection between nanoparticles and holey graphene. The composite electrode brought a power density of 120.7 mW cm^{-2} and a specific capacity of 610 mAh g^{-1} (calculated by the weight of Zn) when assembled in Zn-air batteries. Ni–NiO@holey graphene had a higher specific surface area (166.1 m^2 g^{-1}) and lower charge transfer resistance (101 Ω) compared to its counterpart of pristine graphene (72.3 m^2 g^{-1} and 143 Ω), so the former showed better OER performance with an overpotential of only 0.308 V, much lower than that of the latter (0.403 V).[56]

2.4 Metal–CO_2 Batteries

As a solution to the energy storage for Mars explorations (where the atmosphere contains about 96% CO_2), the Li–CO_2 battery draws massive attention from researchers interested in this field. Similar to the Li–air battery, as shown in **Figure 8**, this battery relies on the reduction and revolution of a gas source, CO_2 in this case, on the cathode. The electrochemical activity of the cathode material plays a vital role in these processes. Holey graphene exhibits prominent specific capacity, rate performance, and cycling stability in this battery due to the high electrochemical activity offered by the abundant active edge-sites atoms around the nanoholes.

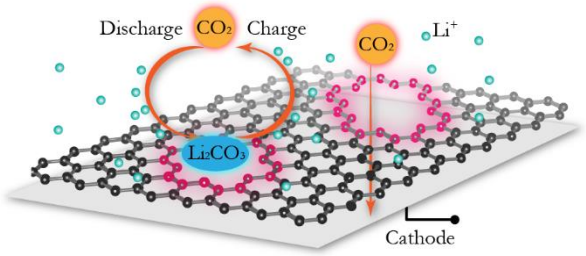

Figure 8. Schematic of Holey Graphene as the Cathode Material for Li–CO_2 Batteries.

L. Qie et al.[57] prepared B,N-doped holey graphene with 4.1 at.% N and 2.6 at.% B and used it as the cathode in a Li-CO_2 battery. The device exhibited significant improvement

in irreversible polarization, rate performance, and cycle life. By incorporating single Fe atoms in N,S-doped holey graphene, the cathode made of this material in a Li-CO_2 battery exhibited an initial discharge capacity of 23,174 mAh g^{-1}, significantly higher than that of its counterpart of pristine graphene (15,280 mAh g^{-1}), due to the simultaneous improvement in gas or ion diffusion and catalytic activity brought by the nanoholes.[58]

2.5 Water Splitting

Water splitting may be a significant energy conversion technology in the near future as it produces a green energy resource, hydrogen. The hydrogen evolution reaction (HER) during water splitting converts protons to hydrogen molecules. This process strongly relies on the electrocatalytic activity of the electrode material. Similar to the fuel cells introduced above, the edge-site carbon atoms on holey graphene (**Figure 9**) also bring higher electrocatalytic activity in the HER.

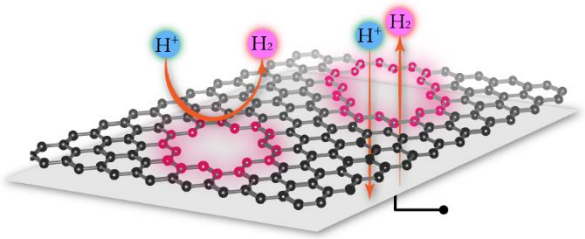

Figure 9. Schematic of Holey Graphene as the Hydrogen Evolution Reaction Catalyst for Electrochemical Water Splitting.

Y. Ito et al.[59] reported that holey graphene incorporated NiMo showed the HER activity comparable to the commercial Pt/C electrode, demonstrating the potential application of holey graphene in electrochemical water splitting. A. Kumatani et al.[60] compared the HER activity of various holey doped graphene, including holey N,P-doped graphene, holey N-doped graphene, holey P-doped graphene, and non-holey N,P-doped graphene, and found that N,P co-doping led to the HER activity of holey graphene close to

that of Pt electrode. Although the specific surface area of the holey N,P-doped graphene (622.5 $m^2 g^{-1}$) was lower than that of the non-holey one (821.5 $m^2 g^{-1}$), the charge transfer resistance of the former (21.5 Ω) was only half of that of the latter (48.1 Ω). This result implied that the higher electrochemical activity led to better HER performance. The operando electrochemical measurement, scanning electrochemical cell microscopy, was employed to obtain the current mapping of undoped and N,P-doped holey graphene under a potential of −0.2 V versus RHE. The result demonstrated that heteroatom doping was beneficial to the electrochemical activity of holey graphene. K. Savaram et al.[61] prepared holey graphene with high conductivity of 17,500 S m^{-1} for hydrogenation. They found that the abundant zigzag edges around the nanoholes on holey graphene largely increased the catalytic activity, thus making it a potential metal-free catalyst in hydrogenation.

2.6 Thermocells

Thermocells convert temperature-dependent electrochemical redox potential to electric power (**Figure 10**). As the electrode material of the thermocell, holey graphene improves the cell performance by facilitating ion diffusion and charge transfer within the device. As reported by G. Li et al.,[62] the power density of a single holey graphene-based thermocell reached 3.6 W m^{-2}, about three times that of activated carbon cloth electrodes, or 6.8 W kg^{-1}, increased by about 76% compared to that of rGO electrodes. The energy conversion efficiency of a single cell relative to the Carnot engine was 0.7%, much higher than that of other electrochemical thermocells (0.4%).

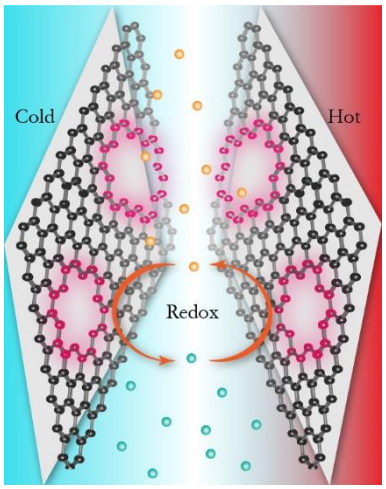

Figure 10. Schematic of Holey Graphene as the Electrodes for Thermocells.

2.7 Water Desalination

In water desalination, holey graphene can offer channels for water molecule transport while separating the impurities and ions by capacitive adsorption. W. Kong et al.[63] reported a holey graphene aerogel with an MB specific surface area of 1,216.7 $m^2 g^{-1}$. When it was used as the capacitive deionization electrode for water desalination systems, it exhibits a high desalination capacity of 26.8 mg g^{-1} in a 5 mg mL^{-1} NaCl solution due to the high capacitive absorption, which is confirmed by the high specific capacitance of 148 F g^{-1} in a 0.5 $_M$ NaCl solution.

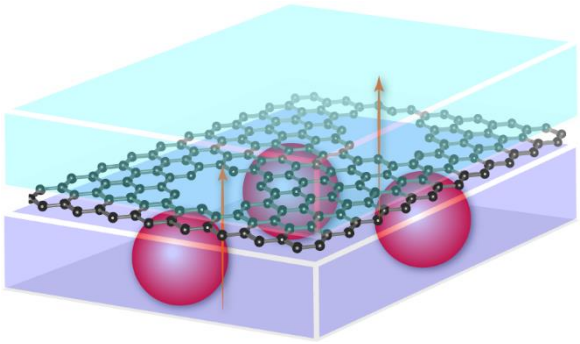

Figure 11. Schematic of Holey Graphene as the Filtration Membrane for Desalination.

M. Mi et al.[64] prepared a composite framework of holey graphene nanosheets and N-doped mesoporous carbon spheres via hydrothermal synthesis, and it had a specific surface

area of 337.7 $m^2 g^{-1}$ and a specific capacitance of 226.5 F g^{-1} in a 0.5 M NaCl solution. Its electro-sorption capacity was 6.8, 17.8, and 32 mg g^{-1} in 0.05, 0.5, and 2.5 mg mL^{-1} NaCl solutions, respectively, which did not obviously decline after 35 desalination cycles.

Y. Yang et al.[65] prepared a composite membrane of holey graphene nanosheets and carbon nanotubes with an average nanohole size and density of 0.63 nm and about 1.0×10^{12} cm^{-2}. The composite membrane showed water permeance of 7.5–37.2 L m^{-2} $hour^{-1}$ bar^{-1} in a device based on cross-flow forward osmosis measurements, while the non-holey version had negligible permeance. In a reverse osmosis cross-flow filtration apparatus, the composite membrane exhibited hydraulic permeance of 110 L m^{-2} $hour^{-1}$ bar^{-1} with high salt rejection percentages in a range of 85.2–93.4% for NaCl, KCl, $MgCl_2$, and Na_2SO_4 and high rejection percentages of larger than 96% for methylene blue, rhodamine B, and fluorescein isothiocyanate. Moreover, the composite membrane withstood the 24 h osmotic operation while keeping a high salt rejection percentage.

2.8 Biochemical Applications

Because of the chemical activity in the region around the nanoholes is different from that of the conjugated region, holey graphene can be used as the biomass carriers by adsorbing biomolecules on the nanoholes. J. Jiang et al.[66] used holey graphene as the carrier for the 5-fluorouracil anticancer drug and found that B-doped holey graphene had the lowest electrostatic adsorption energy to this drug compared to pristine, N-doped, and B,N-doped holey graphene. J. Liu et al.[67] used holey graphene to enhance the Raman response to rhodamine B and found that the nanoholes improved the local charge transfer and adsorption of rhodamine B molecules, suggesting the potential of holey graphene for environment monitoring and food security detection.

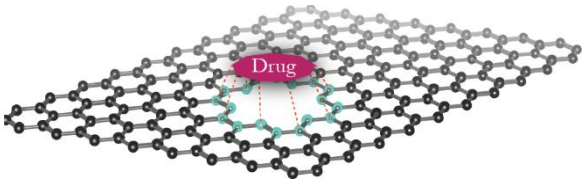

Figure 12. Schematic of Holey Graphene as the Drug Carrier.

2.9 Electronic Applications

Holey graphene obtains the tunable bandgap that pristine graphene does not possess, making it an attractive 2D semiconducting nanomaterial for electronic applications, including field-effect transistors (FETs) and optoelectronics devices.

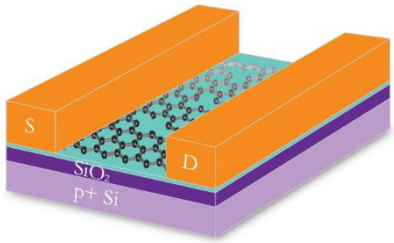

Figure 13. Schematic of the Holey Graphene Field-effect Transistor.

J. Bai et al.[18] prepared holey graphene with a precisely patterned distribution of nanoholes aiming to replace graphene nanoribbons in FET, which have low driving currents and require high-cost processing. They found that the holey graphene-based FET could support significantly higher currents than graphene nanoribbon devices, and the electronic properties, such as the on–off ratio, could be effectively tuned by adjusting the neck width of holey graphene. X. Liang et al.[68] found that the bandgap of holey graphene and the on–off ratio of the holey graphene FET increases with the inverse of the neck width of holey graphene. Z. Zeng et al.[69] proposed a different route to obtain the patterned holey graphene. D. Yang et al.[70] fabricated a holey graphene FET with n-type behaviors and a high on–off ratio of c.a., 2.5. O. Akhavan[71] prepared the patterned holey graphene with p-type behaviors.

D. Singh et al.[72] calculated the electronic, optical, and thermoelectric properties of the holey graphene structure that had two mirrored holes. The direct band gap and optical

gap were 0.95 eV and 1.28 eV, and the thermopower was 1662.59 μV K^{-1}, suggesting that holey graphene was a promising material in optoelectronic and thermoelectric applications.

3 Methods for Manufacturing Holey Graphene

The current manufacturing methods for holey graphene are summarized in this section based on the distinct hole-formation mechanisms. According to the distribution of nanoholes on graphene, these methods can be categorized into two main groups: i) the methods for graphene with the random distribution of nanoholes and ii) the methods for graphene with the periodic distribution of nanoholes. Manufacturing graphene with the random distribution of nanoholes is mostly by partially removing (i.e., etching) atoms from the 2D nanomaterial. The etching process can be induced by oxidation, hydrogenation, and high-energy shock. The etchant can be very distinctive for each specific method, ranging from aggressive chemicals to high-energy particles and from substances to electromagnetic waves. Manufacturing graphene with the periodic distribution of nanoholes is mainly through lithography or bottom-up synthesis. **Appendix C** lists all the reviewed methods.

3.1 Oxidative Etching

Currently, oxidative etching is the most adopted method for holey graphene manufacturing because the carbon atoms on graphene lattice are inert to acid or alkali but vulnerable under the oxidative environment. Many studies use O_2 or other oxidants, such as H_2O_2, HNO_3, Co_3O_4, and Fe_2O_3, as the etchant to directly react with the carbon atoms of graphene.

3.1.1 Etching by HNO_3

The earliest solution-based method to manufacture holey graphene was by using HNO_3 as the etchant, first seen in the study by X. Zhao et al.[19] They mixed 1 mg mL^{-1} GO (prepared by the Hummers method) aqueous dispersion and a 70% HNO_3 aqueous solution

with GO-to-HNO_3 volume ratios of 1:5–1:12.5 and then ultrasonicated the mixture for 1 h to obtain the solution of holey GO, which was filtered, dried, and finally reduced by annealing under Ar or H_2/Ar atmosphere at 700 °C for 1 h. The randomly distributed nanoholes on holey rGO had the average diameters of 7, 20, 80 and 600 nm determined by the fraction of HNO_3 added in the mixture before reaction, and higher fractions led to larger average diameters. The authors perceived this idea referring to the process of cutting carbon nanotubes into fullerene pipes using concentrated acid, and then they proposed that nitric acid as a strong oxidant can oxidize the carbon atoms in the active areas including the existing edge sites of graphene sheets and the damaged sites created by ultrasonication. In two studies using the same method, the average diameters of nanoholes on holey rGO were 2–5 nm under the GO-to-HNO_3 volume ratio of 1:5[51] and 0–90 nm under a different set of parameters[73], respectively.

M. Petal et al.[74] used graphite powder as the starting material to fabricate holey GO in a one-step oxidative etching method. With microwave irradiation (300 W) to achieve simultaneous oxidative exfoliation and etching, the vigorous reactions between the graphite powder and the mixture of HNO_3 and $KMnO_4$ led to the formation of holey GO in just 40 s. They confirmed that non-holey GO was obtained if the duration of the microwave treatment was 30 s.

3.1.2 Etching by H_2O_2

The method using H_2O_2 as the etchant are currently the most popular one for holey graphene manufacturing attributed by a series of works from UCLA. As reported in their first work on this subject,[23] 2 mg mL^{-1} GO (prepared by the Hummers method[75]) aqueous dispersion and a 0.3% H_2O_2 aqueous solution were mixed with a GO-to-H_2O_2 volume ratio of 10:1, and the mixture was directly used in the hydrothermal treatment at 180 °C for 12 h

to obtain the holey GO hydrogel, which was reduced in 1 M sodium ascorbate aqueous solution at 100 °C for 2 h. The obtained holey rGO framework showed a remarkably high BET specific surface area (about 830 $m^2 g^{-1}$), even after being compressed into holey graphene films (about 810 $m^2 g^{-1}$). This method was originated and adapted from a catalytic etching method proposed in an earlier work by J. G. Radich et al.,[76] which will be discussed in Section 3.1.2. The etching mechanism of using H_2O_2 is very similar to that of using HNO_3 since the oxidation of the carbon atoms in the active sites plays the vital role. It is believed that as the etchant, H_2O_2 are more attractive over HNO_3 given that the former is similarly effective, less corrosive, greener, and more easily to be fully removed from the prepared materials. In the subsequent studies by the same group in UCLA,[34] the method was slightly altered by separating the mixture reaction and hydrothermal treatment, increasing the H_2O_2 concentration, and lowering etching temperature and duration. Specifically, GO aqueous dispersion of 2 mg mL^{-1} and a 30% H_2O_2 aqueous solution were mixed with a GO-to-H_2O_2 volume ratio of 10:1 and heated under stirring at 100 °C for 4 h to obtain the holey GO solution. The obtained holey GO showed a BET specific surface area of about 430 $m^2 g^{-1}$ and a prominent pore size distribution in 2–3 nm determined by the Barrett–Joyner–Halenda method. Many studies adopted the H_2O_2 method to obtain holey GO for further development of new nanocomposites, and the size distribution was confirmed in the range of 1–10 nm by either the nitrogen adsorption measurement or TEM observation.

3.1.3 Etching by O_2

The oxidative etching by directly using O_2 as the etchant is another facile method to fabricate holey graphene since it is commonly known that carbon degrades above 450 °C. Therefore, this method is mostly achieved through calcination under atmosphere. Generally, 1 g graphene powder is placed in an open-ended tube furnace and heated under ambient to

450 °C for 10 h to obtain holey graphene with nanohole diameters of 5–20 nm.[58, 77, 78] The long processing time is not very economical and thus limits this method having larger users, while it is practicable for the researchers seeking for obtaining gram-scale holey graphene through simple operations.

K. Savaram et al.[61] reported a microwave-assisted method using graphite intercalation compounds as the staring material instead of GO. Under rapid heating by microwave irradiation, the oxygen-rich intercalation molecules reacted with carbon atoms and escaped the system, the oxygen in air also participated in the oxidative etching, resulting in simultaneous formation of nanoholes and expansion of graphite layers. Compared to that of the tube furnace heat treatment, the processing time of the microwave method was largely reduced to tens of minutes.

Besides the dry methods, holey graphene can also be fabricated through O_2 etching under wet conditions. P. Zang et al.[79] reported a solvothermal method to fabricate holey graphene, during which the GO solution was purged with air for 1 h before the solvothermal reaction at 180 °C for 36 h. Whereas this is similar to the H_2O_2 etching method through hydrothermal synthesis proposed by the UCLA group as mentioned above, this method required even longer reaction time possibly due to the lower oxygen concentration in the solution.

3.1.4 Etching by Oxides or Nitrides

Though not strongly oxidative, oxides or nitrides, such as Fe_2O_3,[80] SnO_2,[81] Co_3O_4,[82] $FeN_{0.056}$,[83] MoO_2,[84] ZnO[85], were found to be successful etchants for creating nanoholes on graphene. By dispersing nanoparticles or precursors of oxides or nitrides onto GO[81, 82, 84, 85] sheets or within inner cells of graphene aerogels[80], the carbon atoms of graphene or GO can be oxidized and partially removed by the oxides or nitrides under annealing at high

temperatures. Both inert[80, 82, 84, 85] and ambient[81, 82] atmospheres during annealing are found effective for the etching. To obtain pure holey graphene, the nanoparticles are removed by acids[80, 81, 82] or evaporation[85]. The as-prepared holey graphene has randomly distributed nanoholes with diameters in a range of 2–50 nm. Changing the annealing temperature brings different products and morphologies due to the change of the reactions between the oxides or nitrides and the carbon atoms on graphene, especially for the oxides or nitrides with transition metal atoms of various valance states, e.g. Co_3O_4.[82] This method offers a good solution for the control over the diameter and population of nanoholes on graphene sheets via adjusting the diameter of nanoparticles and the concentration during dispersing, while it requires more delicate processing steps, which often bring more variables and uncertainties during fabrication. Moreover, the annealing time is hours-long, and the process for dispersing or in situ formation of nanoparticles is complicated. This method is favorable to the fabrication of metal oxides-incorporated holey graphene nanocomposites.[84] If the ultimate goal is to obtain just holey graphene, nevertheless, the introduction of foreign nanomaterials can be difficult to eliminate.

3.2 Catalytic Etching

Catalytic etching use medium materials to facilitate the etching of carbon atoms from graphene sheets. The reactions can be either photocatalyzed or electrochemically catalyzed, and they also can be oxidative or reductive.

3.2.1 Catalyzed Oxidation

The catalyzed oxidative etching is one of the earliest methods for holey graphene fabrication and was first seen in the paper by O. Akhavan[71], who perceived this idea referring to the studies on photodegradation of graphene sheets using semiconducting TiO_2 or ZnO. In this paper, the vertically aligned ZnO nanorods were first grown on a seed layer, and then

the nanorods layer was placed on the GO sheet above on a quartz substrate. Upon UV irradiation for 10 h, holey GO was obtained with nanohole diameters of about 200 nm, slightly larger than the diameter of the ZnO nanorods. The author proposed that the UV photons excited electronic holes on the surface of the ZnO nanorods and caused the oxidation of hydroxyl groups initially attached to the ZnO nanorods, forming hydroxyl (OH•) radicals, which etched the carbon atoms around the contacting regions between the ZnO nanorods and GO sheet. J. G. Radich et al.[76] used Au nanoparticles as the photocatalysis medium absorbing laser irradiation and catalyzing the transformation of H_2O_2 to OH• radicals, which oxidize and etch the carbon atoms on the rGO sheets. The catalyzed etching process lasted 2 h, and the as-prepared holey rGO had nanohole diameters of 5–100 nm. It was also proposed that the irradiation-caused decomposition of H_2O_2 to O_2 and H_2O was a competing process that reduced the formation of OH• radicals for etching.

Y. Lin et al.[86] employed Ag nanoparticles as the medium to catalyze the oxidative etching of graphene sheets. The etching was carried out in an open-ended furnace, and the Ag-anchored graphene powders were heated at 300 °C for 3 h in the air to obtain holey graphene with nanohole diameters of 10^1–10^2 nm. Different from the photocatalyzed etching, the Ag-catalyzed oxidative etching relies on O_2 instead of OH• radicals. The nanoholes were not always in a round shape. Some of them appeared as tracks due to the traveling of Ag nanoparticles above the graphene sheet, and longer etching time caused the formation of longer tracks. C. Guo et al.[87] reported that the average nanohole diameters of about 5, 20, 25, 100, and 150 nm were obtained with the ratio of the Ag precursor to GO of 1:20, 2:20, 3:20, 6:20, and 8:20. E. Alsharaeh et al.[88] prepared Ag@rGO via the microwave-assisted method and obtain similar holey graphene structures using the same etching process.

3.2.2 Catalyzed Hydrogenation

While most catalytic etching reactions induced by metals are oxidative, some studies show that metals can also lead to catalytic etching of graphene through hydrogenation.[67] By direct observation of Fe nanoparticles etching graphene along with its crystallographic directions, S. S. Datta et al.[89] propose that the exitance of Fe nanoparticles catalyzes the reaction between carbon atoms on the graphene lattice and hydrogen atoms from the annealing atmosphere. The same phenomena are observed in the annealing of Ni[90] or Cu[91] nanoparticle-deposited graphene.

3.3 High-energy Shock

3.3.1 Rapid Gas Release

Y. Peng et al.[92] reported that the rapid heating of graphene powder in the air led to the formation of holey graphene due to fast accumulated gaseous products punching through the basal planes of graphene sheets. In this study, the quartz tube was first heated to 300 °C and held for 30 min before directly dropping graphene powder in the tube, resulting in the rapid heating with an ultra-high rate of 100 °C s^{-1} (or 6,000 °C min^{-1}). The randomly distributed nanoholes with diameters of 10–250 nm could form in just about 2–3 s. They also confirmed that for the final temperature of 300 °C during the tube furnace heating of graphene powder, the heating rate lower than 60 °C min^{-1} could not bring the obvious formation of nanoholes. C. Yang et al.[21] reported that by directly transferring graphene powder to the heated tube under 300 °C with an estimated heating rate of >6,000 °C min^{-1}, the holey graphene with nanohole diameters of 50–100 nm was obtained. For the final temperature of 1,100 °C during the tube furnace heating of graphene powder, the increase of the heating rate between 300 and 3,000 °C min^{-1} caused the formation of nanoholes with higher diameters and populations.

3.3.2 Focused Electron Beam Bombarding

Focused electron beam bombarding is a highly delicate processing method used to create a single nanohole with a designed diameter on 2D materials for single-molecule processing such as DNA sensing, translocation, and sequencing. G. F. Schneider et al.[93] reported using the focused electron beam to bombard single nanoholes with diameters of 2–40 nm on graphene. During the process, a mechanically exfoliated graphene sheet with a lateral size larger than 10 μm was transferred onto a 20 nm SiN_x coated 90 nm Si/SiO_2 substrate with a preformed 5 μm hole and then shot by a 300 kV focused electron beam in a TEM with a beam diameter of 15 nm at full width at half maximum and a beam density of 10^6 electrons s^{-1} nm^{-2}. Both single-layer and multilayer (≤8) graphene nanosheets were successfully bombarded to form single nanoholes.

3.4 Bottom-up Synthesis

3.4.1 Templated Chemical Vapor Deposition

Templated CVD is a bottom-up method for synthesizing high-quality holey graphene by presetting nanoparticles on the template to block local growth. Y. Ito et al.[59] first decorated NiMo nanofibers with 18–27 nm SiO_2 nanoparticles and then used them as the templates to grow graphene via CVD. The existence of SiO_2 nanoparticles prevented the growth of graphene lattice in these regions, and therefore the nanohole features could be effectively controlled by the concentration and size of SiO_2 nanoparticles on the NiMo template. A. Kumatani et al.[60] also used the same method to prepare holey graphene@NiMo nanofibers and found the nanohole diameter ranged from 0.01 to 1 μm.

3.4.2 Solvothermal Chemical Synthesis

J. Mahmood et al.[94] reported a simple and scalable chemical synthesis route of holey nitrogenated graphene by slowly adding NMP and a few drops of sulfuric acid or

trifluoromethanesulfonic acid into the mixture of hexaaminobenzene (HAB) trihydrochloride and hexaketocyclohexane (HKH) octahydrate and then heating with oil bath at 175 °C for 8 h. The obtained nanosheets exhibited a layered structure with an inter-planar distance of 0.328 nm, periodically distributed sub-nanoscale holes with an inter-distance of about 0.824 nm, and a semiconductive bandgap of 1.96 eV (measured by the UV-vis spectroscopy). The BET surface areas before and after annealing under argon at 700 °C were 26 and 281 $m^2 g^{-1}$, respectively.

3.5 Lithography

The block copolymer lithography with O_2 plasma as the etchant (also referred to as reactive ion etching, RIE) is generally employed to fabricate the semiconductor-level graphene nanomesh. This method was first reported by J. Bai et al.[18] They placed a mechanically peeled graphene sheet on a silica substrate and then coated a SiO_x intermediate layer and a poly(styrene–block–methyl methacrylate) (P(S–b–MMA)) block copolymer thin film. The UV exposure and glacial acid development removed PMMA from the block copolymer layer leaving the cylinder domains constructed by PS frames. Then, O_2 plasma was used to remove exposed random copolymer and control the thickness of PS frames. The underneath SiO_x film was further etched by CHF_3 plasma to expose the templated regions of the graphene sheet, which was finally etched by O_2 plasma to form periodical in-plane nanoholes with average diameters of 17.7–31.9 nm and average neck widths (the shortest distance between the edges of two nanoholes) as low as 5 nm. This method aims to create high-density nanoholes on graphene with precisely controlled diameters and neck width, significantly affecting the charge transport behavior of graphene and its performance in field-effect transistors. The O_2 plasma etching is much more energized than the oxidative etching methods mentioned above, reducing the etching time down to seconds. Meanwhile,

it requires much more time for the pretreatment and posttreatment relative to the latter. The vital point of this method is templating, which determines the distribution and pattern of nanoholes and the neck width. Though expansive and complicated, this method is effective in fundamental explorations of novel properties of holey 2D materials, especially in electronics. X. Liang et al.[68] used a male copolymer layer to create an imprinted template on a polymeric intermediate layer for creating nanoholes on graphene. The average neck width was controlled between 7 and 17 nm by adjusting the plasma etching time from 10 to 30 s. To avoid using toxic etchants like CHF_3 and CF_4 and degrading the SiO_2/Si substrate, as well as to lower the cost, Z. Zeng et al.[69] used an anodic aluminum oxide mask as the template for creating nanoholes on graphene with neck widths of 33 or 15 nm by etching for 30 or 40 s under O_2 plasma. Y. Yang et al.[65] employed the block copolymer lithography to etch the high-quality graphene sheets synthesized via CVD. Average hole sizes of about 0.55, 0.63, and 1.41 nm can be obtained by O_2 plasma exposure of 5, 10, and 20 s, respectively.

4 Microwave Heating of Graphene

The last section reviews the current methods for manufacturing holey graphene, and it is found that efficient, controllable, and scalable manufacturing is still a challenge. One of the issues is the heating process, which often requires many hours for a single batch. Microwave heating could be a good solution for that. It can bring many advantages:

i) non-contact heating;

ii) effective energy transfer rather than heat transfer;

iii) rapid heating;

iv) selective heating;

v) volumetric heating;

vi) instant on and off;

vii) ease in safety control and automation.[95]

In this section, the microwave heating of graphene is reviewed to assist in understanding the interaction between graphene and microwave.

4.1 Dielectric Loss-induced Heating of Graphene under Microwave Irradiation

Like water molecules under microwave heating, the external alternating electromagnetic field forces the molecular dipoles of water to oscillate and rotate, causing frictions among the dipoles and molecules and generating heat. It is called dielectric heating, which can also occur during microwave heating of GO or rGO since oxygen-containing groups and in-plane defects disturb the π–π conjugation of the pristine graphene lattice and cause polarization.[96]

In dielectric heating, the dielectric constant, ε', and the dielectric loss factor, ε'', are two essential contributors. The former describes the polarizability of a material under an electromagnetic field, meaning the capacity to absorb the energy, and the latter determines the heat converted from the dissipation of the electric energy. They are the real and imaginary parts of the relative complex permittivity ($\hat{\varepsilon}$), respectively, given by

$$\hat{\varepsilon} = \varepsilon' - j\varepsilon'' \quad (1)$$

The dielectric loss tangent, tan δ, correlates the two factors above and is given by the equation,[97]

$$\tan\delta = \frac{(\sigma_e + \sigma_i)/\omega\varepsilon_0 + \varepsilon''}{\varepsilon'} \quad (2)$$

where the phase angle of dielectric loss, δ, relates to the time lag of polarization, σ_e and σ_i are the electronic and ionic conductivity, respectively, ω is the angular frequency of the electromagnetic field ($\omega = 2\pi f$, f = 2.45 GHz), and ε_0 is the permittivity of free space (8.854 $\times 10^{-12}$ F m^{-1}). Since the electronic and ionic dipoles move too fast with the frequencies

much higher than the microwave frequency, the net polarization is always in phase with the electromagnetic field of the microwave, and thus the contribution of σ_e and σ_i can be neglected. Therefore, a simplified dielectric loss tangent can be written as

$$\tan\delta = \frac{\varepsilon''}{\varepsilon'} \tag{3}$$

By solving the Maxwell equations of electric and magnetic fields, the average power of field energy converting to heat per unit volume, P_{ave} (W m^{-3}), can be described by the equation below.

$$P_{\text{ave}} = \frac{1}{2}\omega\varepsilon_0\varepsilon' \tan\delta\, E^2 = \frac{1}{2}\omega\varepsilon_0\varepsilon'' E^2 \tag{4}$$

where E is the magnitude of the electric field (V m^{-1}). The attenuation constant, α, describing the energy dissipation rate of the electromagnetic wave traveling through a material, is given by

$$\alpha = \frac{1}{2}\omega\sqrt{\varepsilon_0\mu_0\mu'}\frac{\varepsilon''}{\sqrt{\varepsilon'}} = \frac{\pi}{\lambda}\frac{\varepsilon''}{\sqrt{\varepsilon'}} \tag{5}$$

where μ_0 is the permeability of free space (1.256 × 10^{-6} H m^{-1}), μ' is the permeability, and λ is the wave constant and written as

$$\lambda = \frac{2\pi}{\omega\sqrt{\varepsilon_0\mu_0\varepsilon'\mu'}} \tag{6}$$

Given by the above equations, ε' and ε'' of GO are vital input variables for the theoretical calculation of microwave heating of GO. B. Kuang et al.[98] suggested that the higher reduction level of rGO obtained via chemical reduction resulted in more vacancy defects and higher conductivities, which enhanced the microwave absorbing and dielectric loss, ε' and ε'', of rGO. They also found that the dielectric loss increased with the mass loading of rGO, especially around the frequency of the commonly seen microwave ovens

(2.45 GHz), and they attributed this phenomenon to the electrons hopping across rGO sheets during microwave irradiation.

However, it is noted that ε' and ε" of GO vary largely in value from sample to sample[99] and thus must be measured by experiments to predict the microwave heating behavior of GO. K. I. Rybakov et al.[100] made efforts in building an analytic model to describe microwave heating of conductive powder materials, however, the calculation results hardly explained the experimental data. H. K. Khattak et al.[101] indicated that the diameter, geometry, and ionic conductivity all contributed to the distinctive locations of hotspots within the heating materials. Therefore, in actual cases, the microwave heating in conductive materials is inhomogeneous, making the first-principal calculation more difficult.

F. Meng et al.[102] reviewed the microwave absorbing of graphene-based materials and suggested that graphene can induce a high conduction loss. The polarization loss was not evident and should be enhanced by doping heteroatoms and defects to increase the polarization centers.

4.2 Conduction Loss-induced Heating of Graphene Under Microwave Irradiation

Many studies on the microwave heating of graphene, graphite, and their derivatives generally observed the fast and intense heating process, which was proposed as the reason causing the rapid GO reduction. Y. Zhu et al.[103] studied the simultaneous exfoliation and reduction of GO induced by microwave heating. The GO powder underwent dramatic volume expansion during microwave heating at a power of 700 W for 1 min under the ambient condition, producing a darker, more fluffy powder. The C/O ratio increased from 0.79 to 2.75 after the microwave heating, indicated by the combustion elemental analysis. The XPS peaks in 286–289 eV assigned to epoxy, hydroxyl, and carboxyl groups dropped obviously. The I(D)/I(G) ratio in Raman spectra decreased, and an obvious 2D peak

emerged. In this paper, they also tried to reduce GO in solutions by microwave heating. 10 mL GO suspension in anhydrous propylene carbonate (PC) with a concentration of 1 mg mL^{-1} was heated under microwave at 700 W for 10 s, and the dried product showed lower electrical resistance, suggesting a higher reduction level. They accredited the successful reduction of GO to the solution temperature of above 100 °C. This was confirmed by a comparison study, where the GO suspension in a DMF/H_2O (9:1) solvent was not successfully reduced with a lower boiling temperature. The TGA results suggested the removal of oxygen-containing groups on GO mainly took place at 120–150 and 170–250 °C.

Another study on the GO reduction under microwave heating by H. Hu et al.[104] investigated the effect of the oxygen content ranging 25–50 wt.%, and they demonstrated the heating process of GO under microwave depended on the local Joule heating. They found that a lower oxygen content resulted in higher microwave-induced temperature elevation. Due to this reason, the GO sheets with lower oxygen contents could remove more oxygen-containing groups during microwave heating. Similarly, the GO sheets that had been treated by microwave exhibited higher temperature elevation than those had not. The influence of the oxygen content was attributed to the difference in the conductivity. Generally, the conductivity of GO increases inversely with the oxygen content. The lower conductivity of GO manifests in the lower local Joule heating caused by the movement of free charge carriers, and therefore the temperature increase is less evident. The authors applied this rule to upgrade the microwave reduction of GO by mixing a fraction of graphene sheets in GO sheets before microwave treatment, and the product showed much higher conductivity.

D. Voiry et al.[105] reported that the local Joule heating induced by microwave could generate high-temperature plasma arcs in graphene powders within 1–2 s. A similar phenomenon is generally observed in microwave heating of metals. The free electrons hop out of the conductive material, causing ionization of the surrounding gas molecules. They used this technique to reduce GO and obtained the semiconductor-level product. The FET based on the microwave-reduced GO exhibited high carrier mobility over 1000 $cm^2 V^{-1} s^{-1}$. Similar results can also be found in another paper by W. Jiang et al.[106]

Interestingly, S. Kang et al.[107] directly compared the microwave heating and Joule heating of graphene obtained by CVD and found that the former was more efficient under the same heating power. The four-layer graphene sample on a quartz substrate reached the saturated temperature at about 20 s under microwave heating, while it took 60 s for Joule heating. Moreover, the temperature distribution across the graphene sheet was more uniform under microwave heating. By tuning the electron mobility of the graphene sheet by the self-assembled monolayers, the study further demonstrated that the carrier mobility of graphene was more vital than the conductivity to achieve efficient heating under microwave irradiation.

5 Research Objectives and Potential Contributions

This research proposes a novel synthesis route for holey graphene, using microwave irradiation to assist the chemical etching of GO sheets by H_2O_2. It aims to achieve the fast and controllable synthesis of holey graphene with tunable structural features and electrochemical properties. Both experimental and computational studies are carried out to investigate the synthesis mechanism of holey graphene via the MACE method, reveal the structural evolution during synthesis, and finally probe and improve the performance in electrochemical energy storage and electrocatalysis.

The detailed research is divided into three parts:

i) the development of an ultrafast, controllable method for holey graphene manufacturing;

ii) the mechanism study on microwave heating of GO;

iii) the electrochemical performance evaluation.

The goal the first part, which is presented in Chapter 3, is to understand the thermal chemical mechanism during MACE and utilize it to achieve rapid manufacturing and effective control over the nanohole microstructure. The mechanism study on microwave heating of GO in Chapter 4 is to explore this complex process from the macroscopic to the microscopic level and from phenomena to fundamental physics. The third part of the research aims to demonstrate the potential of holey graphene manufactured via MACE in various electrochemical applications and provide guidance for property optimization of holey graphene.

This research provides a scalable and fast route for holey graphene manufacturing. The explorations regarding fundamental material science benefit to the understanding of the manufacturing process of holey 2D materials. The investigation on microwave heating is favorable to the realization of large-scale holey graphene manufacturing and provides insights for developing efficient, microwave-assisted methods for a wide range of materials having similar dielectric and structural properties. The electrochemical study paves the way for developing high-performance energy storage devices with rapid charge and discharge capabilities. Moreover, it facilitates further broadening the application range of holey graphene by decoding the complicated relationships among processing, nanohole microstructure, and electrochemical kinetics involving mass transport and charge transfer.

CHAPTER 2

METHODS

1 Raw Materials

The chemicals used in this research included graphite flakes (50+ mesh, powder), potassium permanganate ($KMnO_4$, powder), sulfuric acid (H_2SO_4, 98 wt.%), phosphoric acid (H_3PO_4), hydrogen peroxide aqueous solution (H_2O_2, 30 wt.%), chloride acid (HCl, 1 M), sodium sulfate (Na_2SO_4, powder), potassium ferricyanide ($K_3[Fe(CN)_6]$, powder), potassium chloride (KCl, powder), anhydrous hydrazine, ammonia solution, and ethanol, all purchased from Sigma-Aldrich.

2 Materials Preparation Procedures

2.1 Preparation of Graphene Oxide

GO was prepared by the improved Hummer's method.[108] Graphite flakes (3 g) and $KMnO_4$ powder (18 g) were mixed with a weight ratio of 1:6. H_2SO_4 (360 mL) and H_3PO_4 (40 mL) with a volume ratio of 9:1 were mixed in a flask (500 mL) and added into the mixed powder in a borosilicate glass flat-bottom flask (1 L) with an exotherm to 35–40 °C. The mixture was stirred at 600 rpm and heated to 50 °C for 12 h using a hotplate (Corning PC420) with an FEP-coated stainless-steel thermocouple monitoring the center temperature. After the acidic mixture cooled to room temperature, it was poured on ice (400 mL) and H_2O_2 (3 mL depending on the consumption of $KMnO_4$) loaded in a borosilicate glass beaker (1 L). The exotherm quickly caused the melting of water, and the color of the acidic suspension gradually changed from dark green and purple to yellow, companied with gas bubbling. After bubbling stopped, the suspension was transferred to a group of PC tubes (100 mL) and centrifuged twice at 500 rpm for 15 min in a centrifuge (Frontier FC5714) with a swing-bucket rotor. This step of centrifugation was to remove the thick graphite

flakes that were not sufficiently reacted, so the precipitate was removed. The supernatant was then centrifugated at 4,000 rpm for 30 min to remove impurities and ions. After the supernatant was decanted, the precipitate was added with 1 M HCl for another centrifugation. The precipitate was then washed like this with ethanol and water (twice), successively, and dissolved in water. The aqueous solution was dialyzed in 1-L water using a dialysis membrane (Spectrum, 68 kD MWCO) for 1 d to achieve a pH value of 7. The as-obtained GO aqueous solution was saved in capped glass bottles for further use.

2.2 Microwave Pretreatment of Graphene Oxide

Typically, the GO aqueous solution (3 mL) with a concentration of 3 mg mL^{-1} was added into a borosilicate glass tube sealed by a poly(ether-ether-ketone) cap and loaded in the chamber of a microwave reactor (Anton Paar Monowave 400, 2.45 GHz). The GO solution was pretreated by microwave irradiation to obtain the pretreated GO (denoted as pGO) solution. The treatment was performed at a constant output power of 50 W for 90–360 s with magnetic stirring at a speed of 600 rpm. The setup of the microwave reactor is illustrated in **Figure 14**. Briefly, an infrared thermometer recorded the temperature profile per second, and a pressure sensor collected the variation of pressure inside the reaction tube. Compressed air flow was used to cool down the solution to room temperature after microwave irradiation.

2.3 Preparation of Holey Graphene Oxide

The as-obtained pGO solution (typically 3 mL) with a concentration of 3 mg mL^{-1} were mixed with the 30 wt.% H_2O_2 aqueous solution with a volume ratio of 5: 2 in a capped glass tube. The glass tube was placed in the microwave reactor and irradiated at a constant power of 50 W for 45–180 s. After cooling with compressed air, the solution was transferred to a group of PC tubes (10 mL) and centrifuged at 12,000 rpm for 15 min in a high-speed

centrifuge (Labocon LBHC). The supernatant was decanted to remove residual hydrogen peroxide. The precipitate was then re-dispersed in deionized water, forming the holey GO (denoted as hGO) aqueous solution.

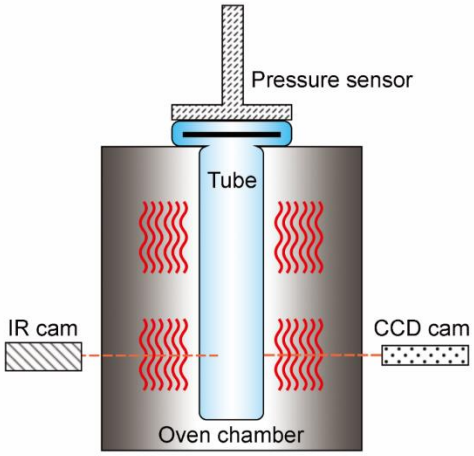

Figure 14. Schematic of the Microwave Reactor Setup.

2.4 Reduction of Holey Graphene Oxide

For rapid manufacturing of reduced hGO (denoted as rhGO), the as-obtained hGO aqueous solution was added into a glass tube without any reduction agent and irradiated in the microwave reactor to 220 °C and held for 90 s with the output power not exceeding 800 W. The process results in a mild reduction of hGO sheets. The rhGO suspension was directly stored for further use.

For obtaining rhGO with a higher reduction level, the hGO solution (typically 10 mL) with a concentration of 0.25 mg mL^{-1} was added with hydrazine (40 μL) and ammonia solution (135 μL) and heated without stirring at 95 °C for 1 h. The product should be filtered immediately after reduction and immersed in deionized water to avoid excessive reactions, which could lead to agglomeration or restacking of rhGO sheets.

3 Materials Characterization

3.1 Transmission Electron Microscopy

The morphologies of graphene sheets were characterized on an aberration-corrected transmission electron microscopy (TEM, FEI Titan 300/80) using the electron beam with an acceleration voltage of 300 kV. Beam alignment and spherical aberration correction were performed under a magnification factor of 215k. A magnification factor of 8,800 is used to search the region of interest (ROI). High-resolution TEM images were taken at magnification factors above 100k.

For preparing the TEM samples, the ethanol solutions of GO, pGO, and hGO were first prepared with concentrations ranging 1–10 $\mu g\ mL^{-1}$. For each specimen, 1–2 μL of the solution was drop-cast on a copper 400 mesh grid coated with a lacey carbon film (Pacific-grids, Cu-400LC) or a holey carbon film (Electron Microscope Sciences, HC400).

For collecting the statistical data of the nanoholes in the TEM images, the contrast was first enhanced, and a threshold was applied to emphasize the nanoholes in TEM images. Then, the pixel area of each nanohole was measured in ImageJ. The smallest area for measuring was defined per image resolution to avoid mistaking the image noises as nanoholes. The statistics data, including total area (%) and population (μm^{-2}), were calculated using the effective area that excluded the regions covered by other objects, e.g., the TEM grid and overlaying graphene sheets.

3.2 Scanning Electron Microscopy

Scanning electron microscopy (SEM) images were taken from a field-emission SEM (FEI XL30). Samples were prepared by dropping powder or drop-casting solutions on conductive carbon or copper tape on a stainless-steel stand.

3.3 Atomic Force Microscopy

The lateral sizes and thicknesses of graphene samples were measured by atomic force microscopy (AFM) on a Bruker Multimode 8 system under the contact mode. AFM tip (Bruker) was 0.01-0.025 Ohm cm Antimony doped Si with 320 kHz resonance frequency and 42 N m^{-1} spring constant. A scanning rate of 96 Hz was used for ROI searching and 256 Hz for data collecting.

The exact sample solutions prepared for TEM were used for the sample preparation for AFM. For each specimen, a few microliters of the sample solution were drop-cast on the surface of a square piece (5 × 5 mm) of a 300-nm SiO_2/Si wafer or a mica disk (reducing the wrinkling of graphene sheets) using a spin-coating device.

3.4 Raman Spectroscopy

Raman spectroscopy was used to scan the Raman scattering features of graphene samples. Raman spectra were taken with a 532 nm laser under a low level of laser intensity to reduce the spot size and the influence of the laser on graphene sheets. The spectrum center and filter gratings were 2050 cm^{-1} and 600 g mm^{-1}, respectively. Each Raman spectrum was scanned 10 times with 1 s duration per each scan. The obtained Raman spectra were peak-fitted using the Lorentz function. The fitting was completed in Origin software.

The exact sample solutions prepared for TEM were used for the sample preparation for Raman spectroscopy. A few microliters of the sample solution were drop-cast on the surface of a square piece (5 × 5 mm) of a 300-nm SiO_2/Si wafer for each specimen.

3.5 X-ray Photoelectron Spectroscopy

The chemical composition of graphene samples was analyzed using the X-ray photoelectron spectroscopy (XPS, VG Escalab 220i-XL) with a monochromatic Al K-alpha source.

The same sample solutions prepared for TEM were used for the sample preparation for XPS. For each specimen, a few milliliters of the sample solution were drop-cast on the surface of a square piece (5 × 5 mm) of a 300-nm SiO_2/Si wafer.

4 Density Functional Theory Calculation

The Vienna Ab-initio Simulation Package was used for all the density functional theory (DFT) calculations.[109] The plane waves used in the calculations had an energy cutoff of 500 eV. We also used the Perdew-Burke-Ernzerhof functional[110] and the corresponding version of standard potential data sets generated by the projector augmented-wave method.[111, 112] All the supercells have a vacuum spacing of 18.0 Å, and a single k point (Γ) was used for the k-point sampling. The atomic coordinates were fully optimized until the forces were converged to 0.01 eV $Å^{-1}$.

5 Molecular Dynamics Calculation

The reactive force-field (ReaxFF) is utilized to describe the bond association/disassociation process during the thermal annealing of GO. Structure optimization with ReaxFF was performed at room temperature. A Berendsen thermostat with a damping parameter of 100 time-steps was used to control the system temperature. The time step is 0.05 fs. Molecular by-products released from the GO sheet were removed periodically every 10 fs to mimic the experimental reduction environment against vacuum.

6 Electrochemical Measurement

6.1 Electrode Property

The measurements of the three-electrode cells were carried out on an electrochemical workstation (CH Instruments 660E) at ambient condition. The setup used a 0.5 mm Pt wire as the counter electrode, a Ag/AgCl reference electrode in 1 m KCl (+0.235

V vs. RHE), and a glassy carbon working electrode (GCE). The working electrode was prepared by drop-casting 10 μg of the active material (1–2 μL per drop) on a freshly polished GCE (polished with 1.0, 0.3, and 0.05 μm alumina powder, successively, and thoroughly rinsed by deionized water after each time polishing). The electrolyte was 1 M Na_2SO_4 solution or 5 mM $K_3[Fe(CN)_6]$ solution with 0.1 M KCl, depending on the purpose of the measurement, which is explained in Chapter 5.

Cyclic voltammetry (CV) was measured in a potential window from −0.2 to 0.8 V vs. Ag/AgCl at scan rates of 5–100 mV s^{-1} with iR compensation performed at the open-circuit potential. Generally, the stabilized curve could be obtained after three CV cycles. Galvanostatic charge and discharge (GCD) curves were measured in a potential window from −0.2 to 0.8 V vs. Ag/AgCl at current densities of 0.5–100 A g^{-1}. Electrochemical impedance spectroscopy (EIS) was performed in a frequency range from 1 MHz to 1 Hz at the open-circuit potential with a bias voltage of 5 mV. For the frequency ranges of 0.01–1 MHz, 24 data points were collocated and repeated one more time, and for the rest frequency range of the measurement, 12 data points were collocated.

The specific capacitance obtained from CV ($C_{S,CV}$, F g^{-1}) and GCD ($C_{S,GCD}$, F g^{-1}) measurements were calculated from the equations,

$$C_{\mathrm{S,CV}} = \frac{\int I_{\mathrm{V}}\mathrm{d}V}{2mv\Delta V} \tag{7}$$

where I_V is the instant current at a specific voltage (A), m is the mass of the active material (g), v is the scan rate (V s^{-1}), and ΔV is the potential window (V);

$$C_{\mathrm{S,GCD}} = \frac{I_{\mathrm{D}}\Delta t_{\mathrm{D}}}{m\Delta V_{\mathrm{D}}} \tag{8}$$

where I_D is the discharge current (A), Δt_D is the discharge time (s), m is the mass of the active material (g), and ΔV_D is the discharge potential change (V).

6.2 Symmetric Supercapacitor Performance

The rhGO suspension reduced by hydrazine and ammonia was filtered by a vacuum filtration kit to prepare the rhGO paper with a diameter of 15 mm. The symmetric supercapacitor was assembled using two identical rhGO papers as the electrodes, which were soaked in the electrolyte (1 M H_2SO_4) for 1 d. A surfactant-coated microporous membrane separator (Celgard 3501) soaked by the electrolyte was placed in between the electrodes, which two titanium current collectors then sandwiched. The whole device was finally wrapped by Parafilm onto a glass slide and clapped by binder clips.

The electrochemical measurements of the symmetric supercapacitor were carried out on a workstation (Gamry Potentiostat IFC1010-28088) at the ambient condition. CV was measured in a potential window of 0–1 V at scan rates of 20–200 mV s^{-1}. Generally, the stabilized curve could be obtained after three CV cycles. GCD curves were measured in a potential window of 0–1 V at current densities of 1–20 A g^{-1}. EIS was measured in a frequency range from 1 MHz to 1 Hz at the open-circuit potential with a bias voltage of 5 mV.

The specific capacitance of the electrode using CV data ($C_{S,CV}$, F g^{-1}) was calculated from the equation,[33]

$$C_{\mathrm{S,CV}} = \frac{\int I_{\mathrm{V}}\mathrm{d}V}{mv\Delta V} \tag{9}$$

where I_V is the instant current at a specific voltage (A), m is the mass of the electrode (g), v is the scan rate (V s^{-1}), and ΔV is the potential window (V). The specific capacitance of the electrode using GCD data ($C_{S,GCD}$, F g^{-1}) was calculated from

$$C_{\mathrm{S,GCD}} = \frac{2I_{\mathrm{D}}\Delta t_{\mathrm{D}}}{m\Delta V_{\mathrm{D}}} \tag{10}$$

where I_D is the discharge current (A), Δt_D is the discharge time (s), m is the mass of the electrode (g), and ΔV_D is the discharge potential change (V).

The gravimetric energy density (E_{wt}, Wh kg^{-1}) and power density (P_{wt}, W kg^{-1}) of the SSC device are calculated from the equations,[23, 37]

$$E_{wt} = \frac{1}{3.6} \times \frac{C_{S,GCD} V_{op}^2}{8} \quad (11)$$

$$P_{wt} = 3600 \times \frac{E_{wt}}{\Delta t_D} \quad (12)$$

where V_{op} is the operating voltage, which is the discharge potential window subtracted by the IR drop potential, and Δt_D is the discharge time (s).

CHAPTER 3

HOLEY GRAPHENE MANUFACTURED VIA MICROWAVE-ASSISTED CHEMICAL ETCHING

1 Introduction

This chapter reports a novel method for manufacturing holey graphene via MACE. Section 2 provides the details of the manufacturing process, which reduced processing time from hour-scale to minute-scale by coupling vigorous chemical attack with rapid electromagnetic wave irradiation. Parameter studies in Section 3 demonstrate that the two-step manufacturing strategy can effectively control the population and area percentage of the nanoholes on graphene. The microstructural evolutions during each step, including the changes in the atomic ratio, defect density, and the number of functional groups, are analyzed by TEM, AFM, Raman, and XPS to understand the mechanisms in the formation and growth of nanoholes on GO sheets. Section 4 unveils the thermal chemical mechanism during the fabrication of holey graphene using multiscale calculations.

2 Microwave-assisted Chemical Etching

The schematic diagram of the two-step MACE method for holey graphene fabrication is illustrated in **Figure 15**a. The bare GO aqueous solution is first pretreated under microwave irradiation for 90–360 s using a microwave reactor without any etchant to obtain the pGO solution. This step can mildly reduce GO before etching. In the reduction of GO, when the oxygen-containing functional groups are removed from the graphene lattice, the surrounding carbon atoms can be taken away at the same time, forming CO or CO_2 and leaving behind vacancies on the lattice.[113] Thus, single- and few-atom vacancy defects on GO sheets emerge during this step. In the second step, the pGO solution is mixed with H_2O_2 and irradiated again in the microwave reactor for 45–180 s. Assisted by

microwave irradiation, the hydrogen peroxide molecules react with GO and remove carbon atoms from the lattice, especially the carbon atoms around vacancy defects, since they are more chemically active.[60, 114, 115] The atom removal leads to the formation of nanoholes on the graphene basal plane. The ultra-high process efficiency is ascribed to the unique selective heating by microwave irradiation on the GO–etchant interface, which will be explained in the following sections. Eventually, a certain amount of hGO solution is obtained depending on the vessel volume.

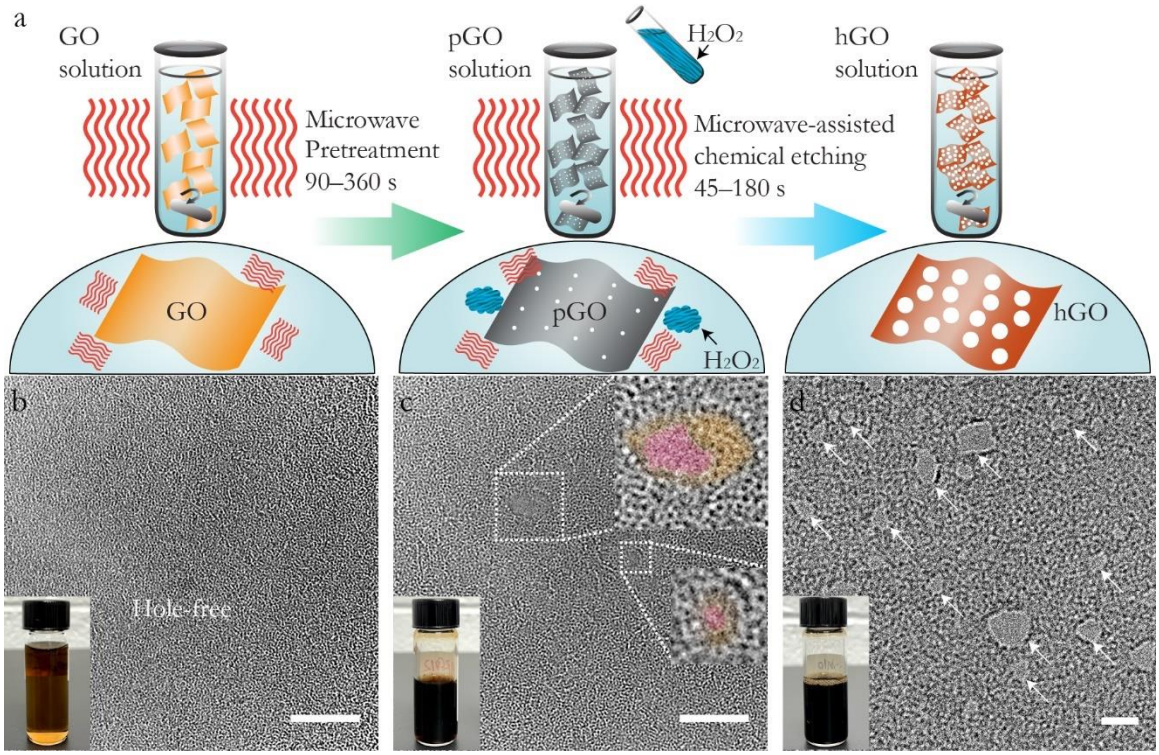

Figure 15. Holey Graphene Fabrication via Microwave-Assisted Chemical Etching with a Two-step Strategy. (a) Schematic of the Fabrication Process; TEM Images of (b) Pristine Graphene Oxide (GO), (c) Pretreated Graphene Oxide (pGO), and (d) Holey Graphene Oxide (hGO). Insets in The Bottom-Left Corners of d–d Are the Digital Images of The Aqueous Solutions. Insets in c Magnify the Locations of Nanoholes and Highlight the Holes (Red) and Functional Group-Depleted Regions (Yellow). Scale Bars in b,c, 5 nm; d, 20 nm.

The morphology evolution of the pristine GO, pGO, and hGO sheets at different stages of fabrication was characterized by TEM. The pristine GO sheet (**Figure 15**b) does

not show any recognizable holey region on the basal plane, and the color of its aqueous solution is light brown (the inset in **Figure 15**b). Within an area of the same size on the pGO sheet (**Figure 15**c), two nanoholes with diameters of about 0.5 and 3.0 nm (the insets in **Figure 15**c) are found, and the color of the pGO solution turns darker (the inset in **Figure 15**c) due to the reduction of GO by the microwave pretreatment.[103, 116] The yellow regions in the insets of **Figure 15**c show that the functional groups are depleted in the areas around the nanoholes, while they still cover other areas of the pGO sheet. This suggests that the formation of the nanoholes on the pGO sheets are strongly related to the removal of functional groups. However, the sole reduction process (i.e., the removal of functional groups) cannot bring the formation of abundant nanoholes, and an etching reagent such as hydrogen peroxide is necessary. With the coupling effect of microwave irradiation and chemical etching, the nanoholes with a high density and diameters up to about 25 nm are observed on the basal plane of the hGO sheet (**Figure 15**d). According to the AFM images (**Figure 16**), no apparent change is identified from GO to hGO in both thickness (about 1 nm) and size (μm-scale), implying that both the microwave exposure and etchant concentration are in the appropriate ranges to avoid disintegrating the GO sheets into small pieces.

The XPS spectra of the pristine GO, pGO, and hGO sheets (**Figure 17**a) show that they are mainly composed of C, O, S, and N atoms. We can analyze the constituent change during each fabrication step by calculating the C/O or C/(O+N+S) atomic ratio from the XPS spectra. As indicated by the higher C/O ratio of pGO relative to GO (**Figure 17**b), the microwave irradiation during the pretreatment causes a partial removal of the oxygen-containing functional groups from GO sheets. If the sulfur- and nitrogen-containing groups are considered, the pretreatment still brings an increase in terms of C/(O+N+S) from 2.05

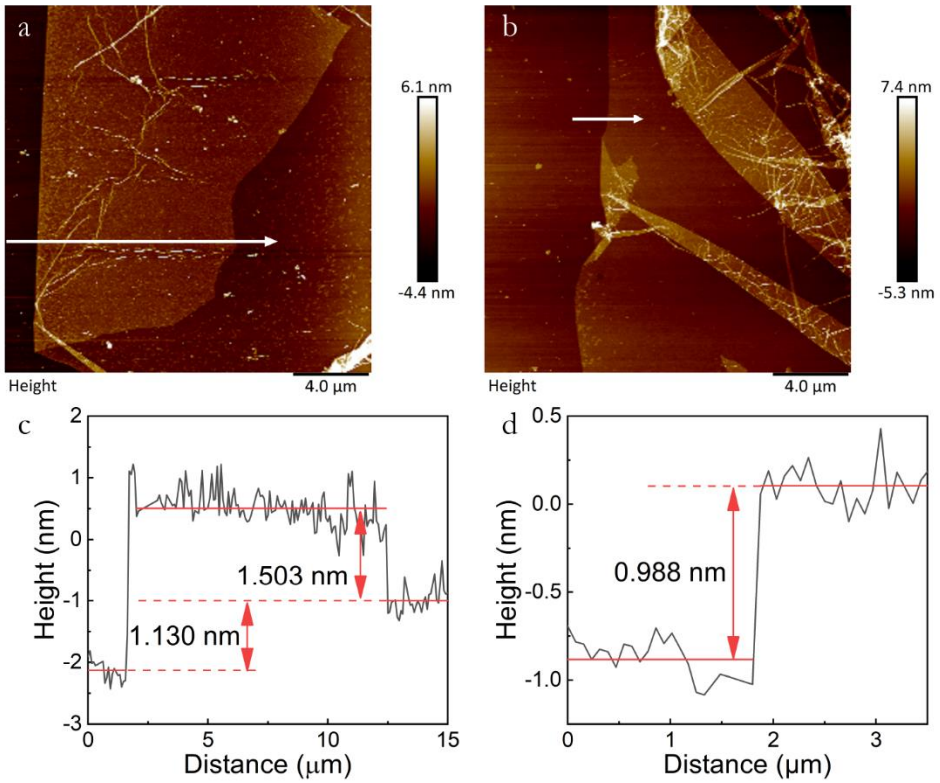

Figure 16. AFM Images of (a) Pristine Graphene Oxide and (b) Holey Graphene Oxide Sheets on 300 nm SiO_2/Si Substrate. (c,d) Height Profiles of the Arrow Lines in a,b, Respectively.

to 2.23. Such microwave-induced partial reduction of GO is also observed in other studies.[103, 117] After the MACE, the hGO sheets show a negligible increase of the C/O ratio from 2.40 to 2.41, suggesting that the losses of carbon and oxygen atoms were balanced during this step. The oxygen supply of hydrogen peroxide led to the formation of new oxygen-containing groups on GO sheets, equalizing the removal of oxygen-containing groups caused by microwave irradiation. This is an obvious distinction between the MACE and conventional chemical-etching methods, which generally show a lower C/O ratio after etching.[23, 26, 43, 118] The increase of the C/(O+N+S) ratio from 2.23 to 2.33 after the MACE indicates that the removal of sulfur- and nitrogen-containing groups on GO sheets are significant in this step.

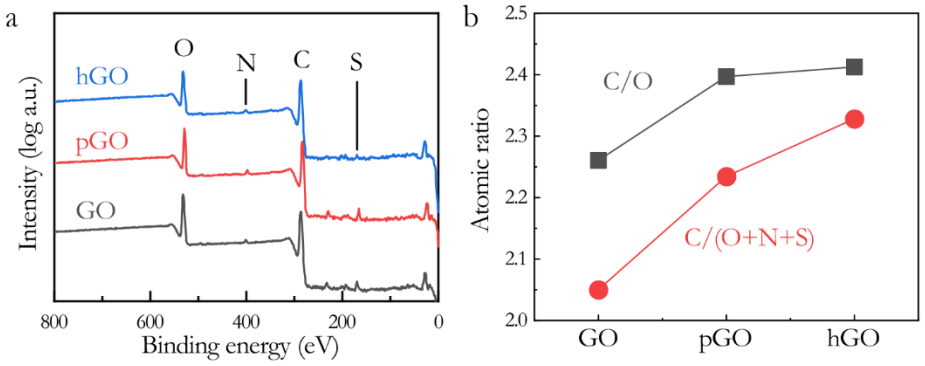

Figure 17. (a) XPS Spectra of Graphene Oxide, Pretreated Graphene Oxide, and Holey Graphene Oxide; (b) C/O and C/(O+N+S) Atomic Ratios Obtained from the XPS Spectra.

Raman spectroscopy was employed to characterize the disorder level of GO sheets, i.e., the distortion of sp^2 graphitic rings on the graphene lattice affected by both defects and functional groups.[119] Research has reported that the disorder level of GO grows with the full width at half-maximum (FWHM) of the G band, one of the characteristic peaks in the Raman spectra of graphitic structures.[120, 121] The FWHM(G) of GO (**Figure 18**a) decreases from 66 to 63 cm^{-1} after the pretreatment and increases to 73 cm^{-1} after the MACE, suggesting that the graphitic arrangements of the graphene lattice are first restored by the pretreatment and then distorted by the MACE. Although the pretreatment creates the vacancy defects that distort the graphene lattice, the disorder level of pGO is affected more by the removal of functional groups during the pretreatment. The MACE, on the other hand, significantly promotes the disorder level by forming the nanoholes that cause large lattice distortion on hGO sheets. In addition, the intensity ratio of the D to G band (I_D/I_G) is another commonly used indicator of the disorder level on GO sheets. Cançado et al. report that with the increase of FWHM(G), the I_D/I_G ratio of the single-layer graphene first grows within a low-disorder range and then reduces when entering the high-disorder range.[122] In this study, the correlations between FWHM(G) and I_D/I_G (**Figure 18**b) of all the GO, pGO, and hGO samples exhibit similar trends. The values of FWHM(G) and I_D/I_G

become lower from GO to pGO, while the hGO samples show mostly higher FWHM(G) and lower I_D/I_G than GO. It confirms that the pGO samples are in the low-disorder range where I_D/I_G increases with the disorder level, while the hGO samples are in the high-disorder range where I_D/I_G reduces with the disorder level. Also, it is found that FWHM(D) is a similar indicator as I_D/I_G to determine the disorder level of GO (**Figure 18**c,d).

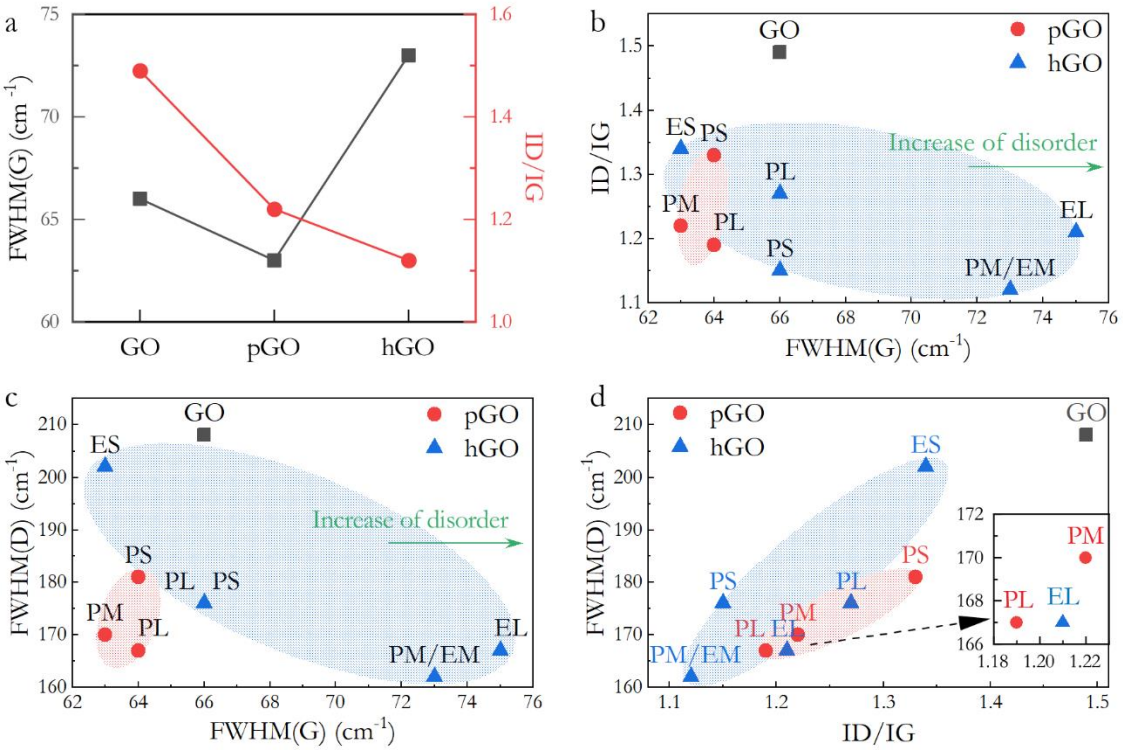

Figure 18. Raman Spectroscopy Results of Graphene Oxide, Pretreated Graphene Oxide, and Holey Graphene Oxide: (a) the Changes in Full Width at Half Maximum of the G Band FWHM(G) and Intensity Ratios of the D to G Band (I_D/I_G); Diagrams of (b) I_D/I_G vs. FWHM(G), (c) FWHM(D) vs. FWHM(G), and (d) FWHM(D) vs. I_D/I_G.

3 Controllable Formation and Growth of Nanoholes

3.1 Effect of Pretreatment Durations

Differed from most methods of solution-based holey graphene fabrication,[26, 27, 29, 38, 47, 118] the two-step approach in this study offers the controllability of the microstructural features of nanoholes by tuning the processing durations of the pretreatment and MACE. It

enables microstructural engineering of holey graphene to meet the requirements of various applications. To understand the effect of the pretreatment step on the size and population of nanoholes, a group of pGO samples were prepared with pretreatment durations of 90 (denoted as pGO-PS), 180 (denoted as pGO-PM), and 360 s (denoted as pGO-PL), respectively. After the MACE with the same condition (power: 50 W; duration: 90 s), the samples were denoted as hGO-PS, -PM, and -PL, respectively. **Figure 19**a–c presents the TEM images of the hGO sheets. **Figure 19**d–f displays the histograms of the nanohole diameter collected from the TEM images. The statistics data of the nanoholes in the TEM images, including the total area percentage, population, range of diameter, median diameter, and average diameter, are summarized in **Table 1** and illustrated in the radar chart (**Figure 19**g). The corresponding Raman and XPS results are shown in **Figure 19**h,i.

With the shortest pretreatment, hGO-PS (**Figure 19**a) displays the sparsely scattered nanoholes with diameters widely distributed from 7 to 22 nm (**Figure 19**d). The nanoholes of hGO-PS exhibit the lowest population (45 μm^{-2}) and area percentage (0.6%) because the 90-s pretreatment only creates a limited number of vacancy defects as the formation sites of nanoholes. The low defect density on the pGO-PS sheets is related to the low reduction level of pGO-PS indicated by the Raman (**Figure 19**h) and XPS results (**Figure 19**i) of pGO-PS: the C/O and C/(O+N+S) ratios of pGO-PS are the lowest among all the pGO-P samples; the decrease in I_D/I_G from GO (1.49) to pGO-PS (1.33) is also the smallest. As a result, the formation of nanoholes on the hGO-PS sheets is not prominent after the MACE. This can be confirmed by the negligible increase in FWHM(G) from 64 to 66 cm^{-1} (**Figure 19**h). Nevertheless, the nanoholes of hGO-PS have the largest average and median diameters (13.4 and 11 nm). During the MACE, the limited population of defect regions on the pGO-

PS sheets causes the constant etching of a few preferential locations on the lattice where more carbon atoms are removed compared to the other samples.

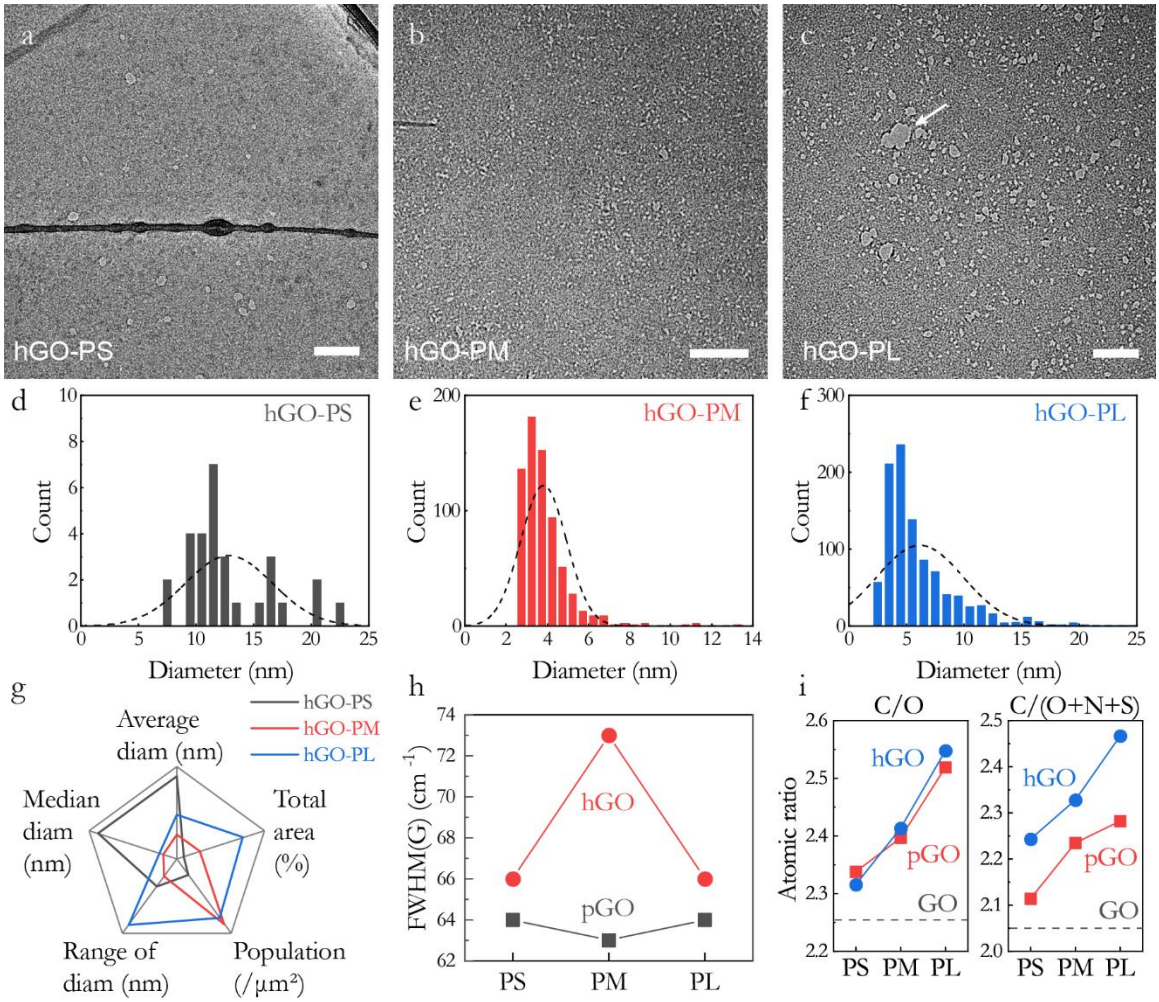

Figure 19. Holey Graphene Oxide (hGO) Sheets Prepared with Different Pretreatment Durations. TEM Images of hGO Pretreated for (a) 90, (b) 180, and (c) 360 s. Scale bars in a–c, 100 nm. (d–f) Histograms of the Nanohole Diameter Collected from a–c. (g) Radar Chart Comparing the Total Area Percentage, Population, Range of Diameter, Median Diameter, and Average Diameter of the Nanoholes in a–c. (h) FWHM(G) Obtained from the Raman Spectra of Pretreated Graphene Oxide (pGO) and hGO. (i) C/O and C/(O+N+S) Atomic Ratios Obtained from XPS Spectra of GO, pGO, and hGO.

Table 1. Statistics Data of the Nanoholes in Figure 19a–c.

Sample	Total area [%]	Population [μm^{-2}]	Range of diameter [nm]	Median diameter [nm]	Average diameter [nm]
hGO-PS	0.6	45	22	11	13.4
hGO-PM	2.1	1687	14	3.5	4.0
hGO-PL	6.0	1469	53	4	7.2

The nanohole population of hGO-PM (**Figure 19**b) drastically grows to 1687 μm^{-2}, bringing the high area percentage (2.1%) that generates the highest disorder level among all the samples (indicated by the largest FWHM(G) of 73 cm^{-1}, **Figure 19**h). The nanoholes of hGO-PM exhibit the smallest range of diameter (2.5–13.0 nm), average and median diameters (4.0 and 3.5 nm). As indicated by the lower FWHM(G) of pGO-PM relative to pGO-PS (**Figure 19**h), the longer pretreatment causes a higher reduction level of pGO-PM, meaning the formation of more vacancy defects on the pGO-PM sheets. During the MACE, the pGO-PM sheets can provide many chemically active sites for the etching reaction, resulting in a uniform formation of abundant nanoholes on the hGO-PM sheets.

As the pretreatment duration increases to 360 s, the total area percentage of nanoholes of hGO-PL surges significantly to 6.0%, with a large average diameter of 7.2 nm. As indicated by the largest C/O and C/(O+N+S) ratios (**Figure 19**i) among all the pGO-P samples, the highest reduction level of pGO-PL leads to large numbers of defects created during the pretreatment, promoting the nanohole formation on the hGO-PL sheets. Many nanoholes joined each other during the MACE, forming much larger nanoholes with diameters up to 53 nm (**Figure 19**c). The joining of nanoholes on hGO-PL leads to a slight drop in population and a broader range of diameter relative to hGO-PM. However, the diameters of most nanoholes are still smaller than 5 nm (**Figure 19**f). In fact, if we assume the average diameter of nanoholes is constant under the same processing condition during the MACE, a theoretical nanohole population (that has eliminated the effect of joining) of hGO-PL can be estimated using the average diameter of nanoholes of hGO-PM (4.0 nm) and the area percentage of hGO-PL (6.0%). The calculated value is 4775 μm^{-2}, much larger compared to hGO-PM (1687 μm^{-2}). It leads us to further consider the possibility of limiting the joining of nanoholes by varying the duration of MACE.

Figure 20 illustrates the effect of pretreatment duration on the microstructure of pGO and hGO sheets. For the pretreatment of 90 s, the density of vacancy defects on pGO is not high, so these vacancy defects are constantly etched and enlarged into nanoholes during MACE, leading to the relatively large average diameter but the low population of nanoholes. When the pretreatment duration is longer, more functional groups can be removed, and a higher density of vacancy defects can be generated on pGO. Therefore, more nanoholes can be obtained on the hGO sheet with the pretreatment of 180 s. When the pretreatment duration reaches 360 s, the defect density is the highest on pGO, resulting in the high population of nanoholes on dGO. Meanwhile, the crowded nanoholes join each other during MACE, so the further increase in populations is limited.

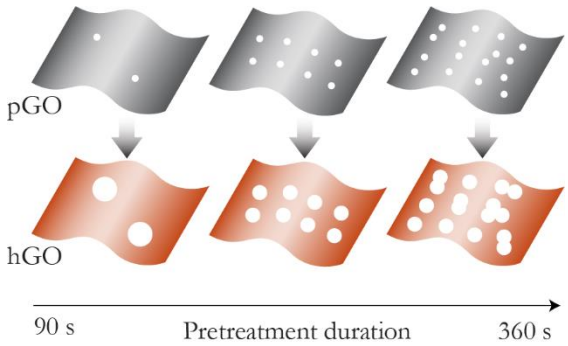

Figure 20. Schematic Showing the Effect of Pretreatment on the Microstructure of Pretreated Graphene Oxide and Holey Graphene Oxide.

3.2 Effect of Durations of Microwave-assisted Chemical Etching

Another group of hGO sheets were prepared to study the effect of MACE durations on the nanohole microstructure. The GO solutions were first pretreated under microwave for 180 s (the same as pGO-PM) to obtain a decent defect density on pGO, as demonstrated above. Then, the pGO samples were etched for 45 s (denoted as hGO-ES), 90 s (denoted as hGO-EM), and 180 s (denoted as hGO-EM), respectively. **Figure 21**a–c shows the TEM images of the samples. **Figure 21**d–f presents the histograms of the nanohole diameter in

the TEM images. The statistics data of the nanoholes are summarized in **Table 2** and illustrated in the radar chart (**Figure 21**g). The corresponding Raman and XPS results are shown in **Figure 21**h and **Figure 21**i.

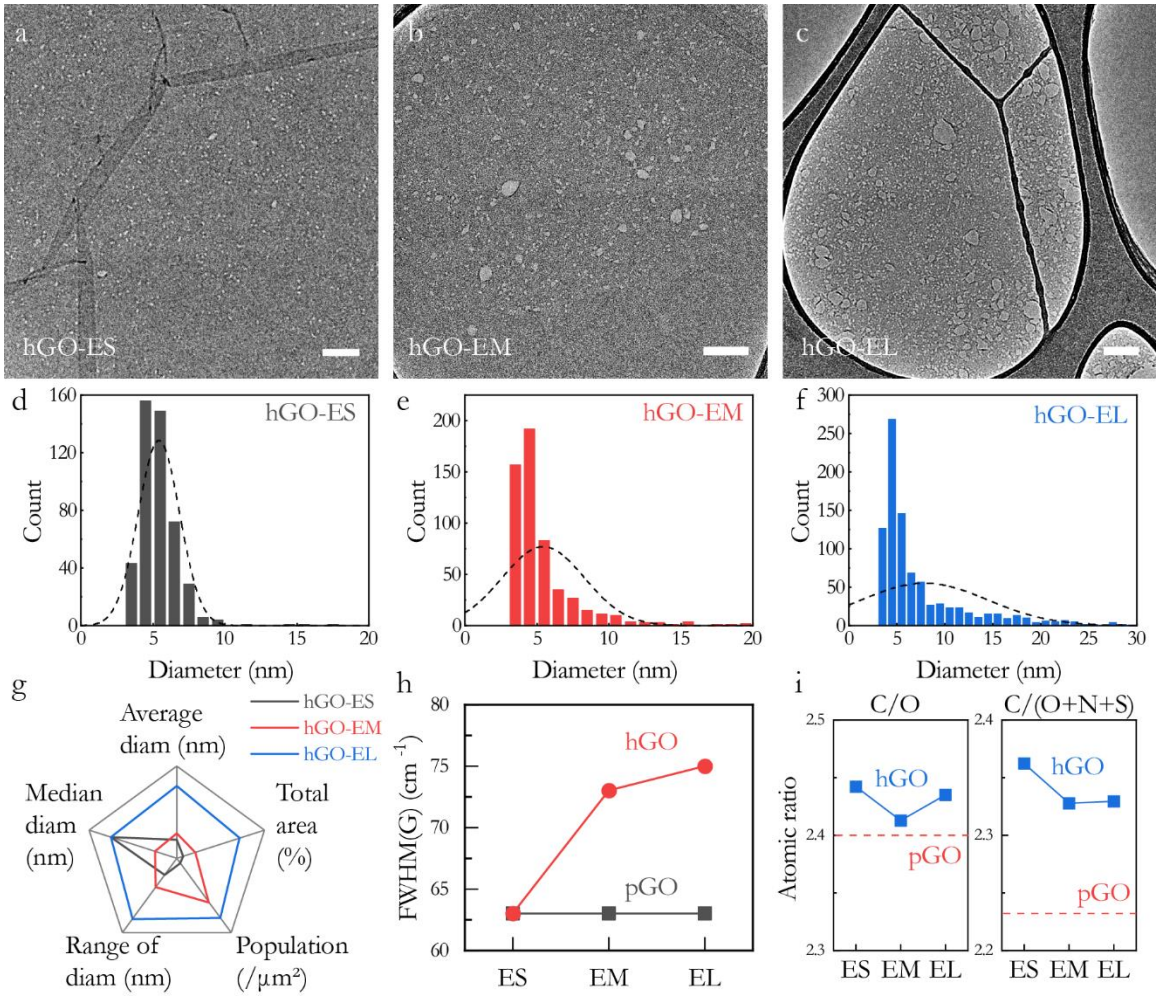

Figure 21. Holey Graphene Oxide (hGO) Prepared with Different Durations During Microwave-Assisted Chemical Etching. TEM Images of hGO Etched for (a) 45, (b) 90, and (c) 180 s. Scale Bars in a–c, 100 nm. (d–f) Histograms of the Nanohole Diameter Collected from a–c. (g) Radar Chart Comparing the Total Area Percentage, Population, Range of Diameter, Median Diameter, and Average Diameter of the Nanoholes in a–c. (h) FWHM(G) Obtained from the Raman Spectra of Pretreated Graphene Oxide (pGO) and hGO. (i) C/O and C/(O+N+S) Atomic Ratios Obtained from XPS Spectra of pGO and hGO.

Table 2. Statistics Data of the Nanoholes in Figure 21a–c.

Sample	Total area [%]	Population [μm^{-2}]	Range of diameter [nm]	Median diameter [nm]	Average diameter [nm]
hGO-ES	1.1	454	18	5	5.6
hGO-EM	3.1	1050	31	4	6.2
hGO-EL	10.7	1295	65	5	10.3

After the MACE of 45 s, small nanoholes (5.6 nm) are observed on hGO-ES (**Figure 21**a) with a relatively low population (454 μm^{-2}), while the range of diameter is narrow (3.5–18 nm). The emerging of nanoholes from vacancy defects is more obvious than the size growth of nanoholes. It is because that the short duration of MACE limits the etching of GO sheets. Both the FWHM(G) (**Figure 21**h) and C/O ratio (**Figure 21**i) show no apparent change caused by the short duration of MACE.

The MACE of 90 s brings a drastic growth in the population of nanoholes to 1050 μm^{-2} (**Table 2**). Compared to hGO-ES, hGO-EM (**Figure 21**b) shows a larger total area percentage of nanoholes (3.1%) and a higher disorder level with FWHM(G) of 73 cm^{-1} (**Figure 21**h). The range of nanohole diameter of hGO-PM becomes broader (3.5–31 nm) because of the joining and preferential growth of nanoholes during the 90-s MACE.

The MACE of 180 s results in a major boost both in the total area percentage (10.7%) and average diameter (10.3 nm) of nanoholes with a high population of 1295 μm^{-2}. The range of diameter further broadens (3.5–65 nm). Many joined holes with diameters over 20 nm are observed on the hGO-EL sheet (**Figure 21**c). The disorder level of hGO-EL is the highest among all hGO-E samples, as indicated by FWHM(G) (**Figure 21**h). The C/O ratio (**Figure 21**i) of hGO-EL abnormally increases after the MACE due to a higher reduction of GO induced by long-time irradiation.

The mechanism of MACE is illustrated in **Figure 22**. In contrast to the effect of pretreatment durations, which mainly changes the population of nanoholes on hGO, the MACE process affects both the formation and growth of nanoholes by coupling chemical etching and microwave irradiation. With a moderate defect density on the pGO sheets, the longer duration of MACE brings a larger nanohole population and the joining and preferential growth of nanoholes that increase the range of diameter and total area

percentage. Therefore, the short duration of MACE is favorable to form the nanoholes with relatively uniform diameters, while the long duration of MACE contributes most to the high population and total area percentage of nanoholes. By tuning the duration of both pretreatment and MACE, the microstructural features of nanoholes can be effectively controlled.

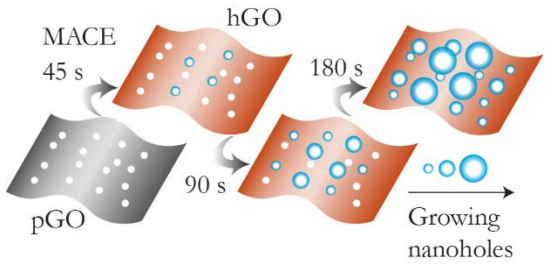

Figure 22. Schematic of the Effect of Durations of Microwave-assisted Chemical Etching on the Microstructure of Holey Graphene Oxide.

4 Thermal Chemical Mechanism for Microwave-assisted Chemical Etching

4.1 Oxidation of graphene by hydrogen peroxides

DFT calculations were performed to investigate the reactions between graphene and hydrogen peroxide. Before the calculation, a hydrogen peroxide molecule was placed on the centers of the graphene model. The effects of the functional groups and vacancy defects on the reactions were revealed by using four graphene models, i.e., pristine graphene (**Figure 23**a), GO (one epoxy group in each unit cell of the graphitic ring, **Figure 23**b), graphene with a vacancy defect (a six-atom ring is taken away from the graphene lattice, **Figure 23**c), and GO with a vacancy defect (**Figure 23**d). Each of the calculations ends until the global minimum of the system energy is achieved. According to the Bose–Einstein statistics, the energy change from the initial to the end of the calculation can determine the possibility of each reaction taking place.

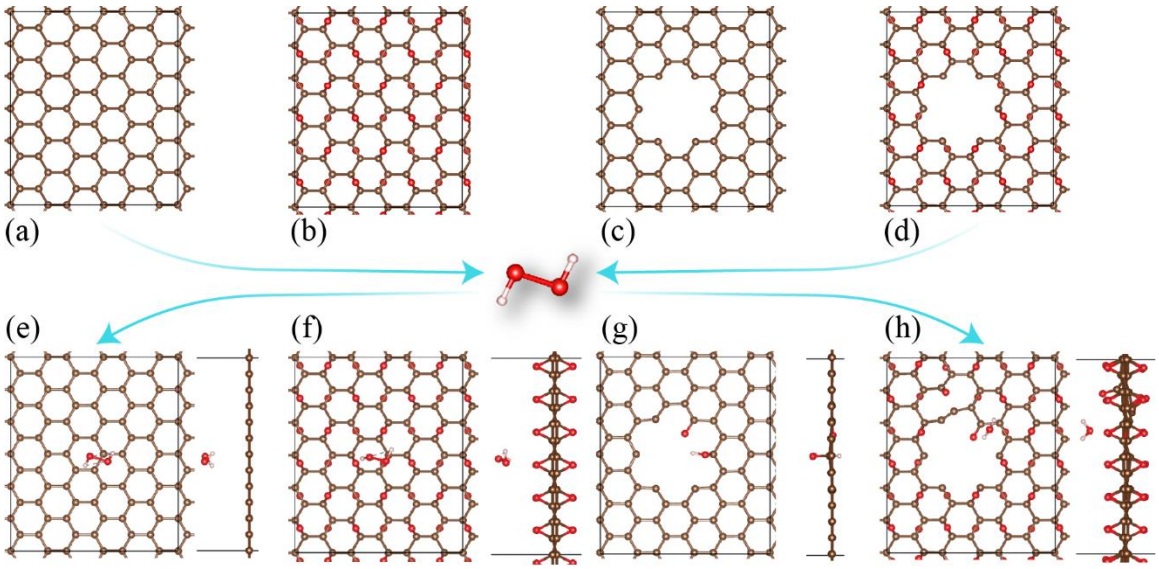

Figure 23. Models for Density Functional Theory Calculations of the Reactions between a Hydrogen Peroxide Molecule and (a) Graphene, (b) Graphene Oxide, (c) Graphene with A Vacancy Defect, and (d) Graphene Oxide with a Vacancy Defect, Respectively, and (e–h) the Corresponding Calculation Results of the Reactions.

The calculation results suggest that the reactions only occur when graphene and GO have the vacancy defect (**Figure 23**g,h), with the corresponding energy changes of −7.06 and −7.08 eV (**Table 3**), respectively. Interestingly, in both the reactions, the edge-site carbon atoms around the vacancy defect are the preferred targets attacked by the hydrogen peroxide molecule. For the graphene model with a vacancy defect (**Figure 23**g), the edge-site carbon atoms are anchored by a carbonyl, a hydrogen, and a hydroxyl group. For the GO model with a vacancy defect (**Figure 23**h), one edge-site carbon atom is anchored by a hydroxyl group, while a C–C bond is broken two atoms away from the anchoring location.

Table 3. Products and Energy Changes of the Reactions between Hydrogen Peroxide and Four Graphene Structures.

Start material	Products	Energy change
Graphene	\	\
GO	\	\
Graphene with a vacancy	C=O, C–H, C–OH	−7.06 eV
GO with a vacancy	C=O, H_2O	−7.03 eV

For all possible reactions, the results are the adsorption of oxygen-containing groups on the carbon atoms. There is no direct removal of carbon atoms, indicating that hydrogen peroxide can only oxidize the graphene sheets instead of directly taking away carbon atoms. In an actual reaction, a GO sheet may contain the features in local areas that similar to those four different graphene models. The areas with vacancy defects are more vulnerable to hydrogen peroxide than the conjugated areas on the GO sheet, and the hydrogen peroxide molecules prefer to oxidize the carbon atoms around the vacancy defects, forming mainly carbonyl and hydrogen groups. As demonstrated in the last section, in-plane holes can emerge on the GO sheets without inducing severe lattice degradation under heating at low temperatures, while the growth stops within a sufficient period of time. The DFT calculations demonstrate that by adding hydrogen peroxide into the system, oxygen-containing groups from the hydrogen peroxide molecules can anchor on the carbon atoms at the edges of the existing holes, causing the weakening of the C–C bonds selectively around those areas.

4.2 Formation of In-plane Holes under Annealing

Thermal annealing is a common method for reducing GO, which removes the functional groups from the graphene lattice and induces the removal of carbon atoms and the generation of in-plane vacancy defects.[123] The oxygen-containing functional groups such as the hydroxyl and epoxy groups weaken the π–π conjugations between the neighboring carbon atoms and increase their activity. During annealing, the hydroxyl and epoxy groups take carbon atoms from the graphitic lattice to form the gaseous species that eventually leave the system. Intuitively, thermal annealing could be used to generate in-plane holes on graphene sheets. The MD simulation was carried out to evaluate the hole formation process during thermal annealing GO sheets. In this simulation, a constant temperature increase (8

K fs^{-1}) was applied on a GO model until it reached the target temperature, and the temperature was held to the end. The gaseous productions, such as CO, CO_2, and H_2O, were removed immediately after generation during the whole process.

The initial structure of the GO model (**Figure 24**a) is a graphene sheet randomly anchored by the functional groups that are commonly found in experiments,[123, 124] i.e., the hydroxyl and epoxy groups. After annealing at 1000 K (**Figure 24**b), no carbon atom is removed from GO throughout the whole simulation (**Figure 24**h), but a few six-atom graphitic rings rich in functional groups are torn off due to the breakage of the sp^2 C–C conjugation, resulting in the emerging of the small in-plane holes in these locations. By increasing the target temperature to 1500 K (**Figure 24**c), the breakage of graphitic rings is more evident. The removal of carbon atoms (1%) is observed under this temperature. Temperatures of 2000 and 2500 K (**Figure 24**d,e) only cause slightly higher atom loss percentages (about 2%), but the sizes of in-plane holes become larger. The annealing at 3000 or 3500 K (**Figure 24**f,g) results in severe lattice degradation. The breakage of graphitic rings is not limited to the locations rich in functional groups but extends to the whole lattice. The atom loss percentage surges to about 8% at 3000 K and 18% at 3500 K, respectively. **Figure 24**h shows that the carbon atom loss percentages at different temperatures all stabilize with time. The continuous energy input to the GO sheet does not constantly induce the carbon atom removal and the breakage of graphitic rings, meaning the formation and growth of in-plane holes on graphene during heating are limited by the temperature. However, the annealing at high temperatures also leads to severe lattice degradation. It should be noted that this rule is tenable when the number of the pre-occupied oxygen-containing groups is a constant. The MD simulation results suggest that it is indeed that heating can cause the formation of in-plane holes on graphene. However, it cannot lead to

the continuous formation and growth of the in-plane holes without inducing severe degradation of the neighboring graphitic rings.

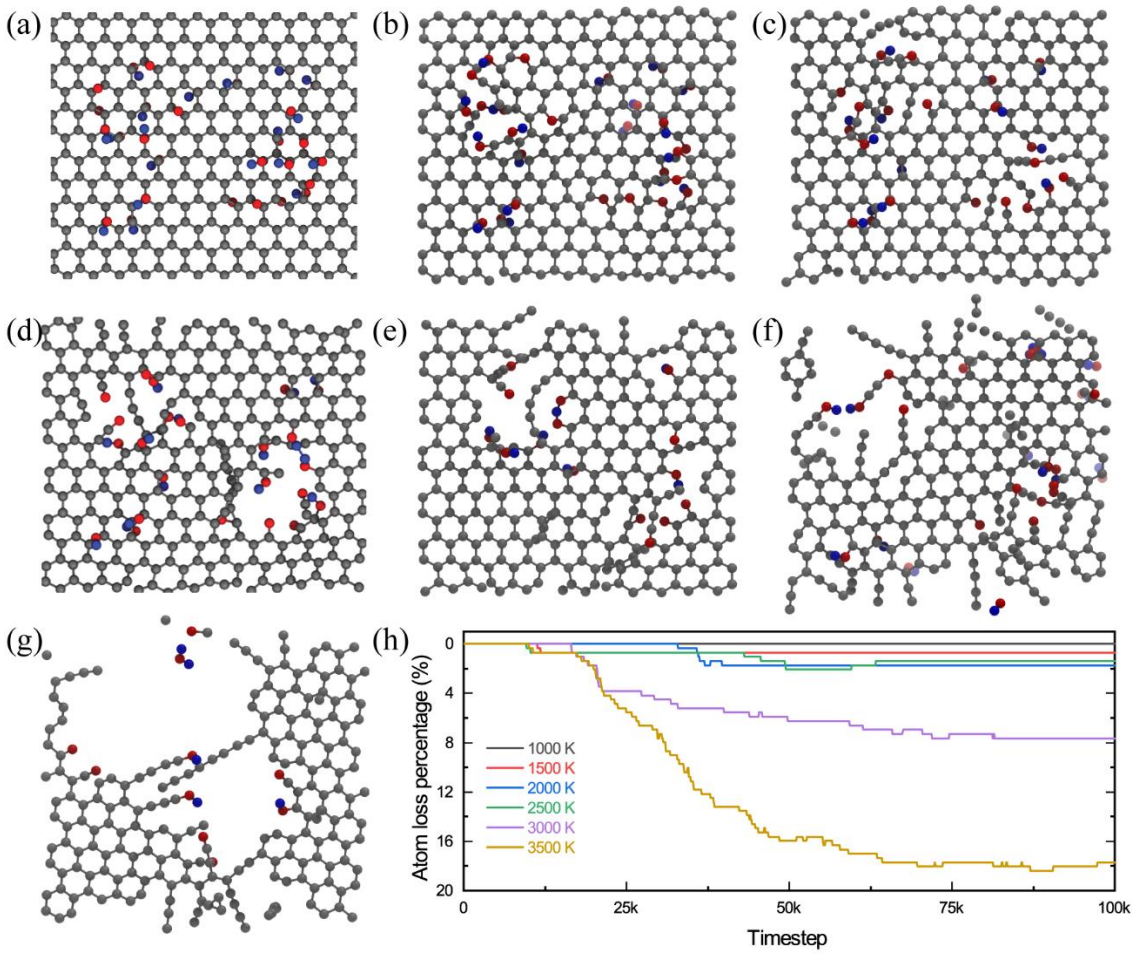

Figure 24. Molecular dynamics simulation of thermal annealing graphene oxide at various temperatures: (a) the initial model; (b–g) the models after annealing at 1000, 1500, 2000, 2500, 3000, and 3500 K; (h) the diagram of the carbon atom loss percentage of the graphene model with respect to the timestep of the simulation.

4.3 Continuous Growth of In-plane Holes

A possible solution to avoid the large-area degradation during the formation and growth of in-plane holes on graphene is to selectively remove the carbon atoms at the edge sites of the holes, promoting the continuous growth of the existing holes. This could be achieved by anchoring oxygen-containing functional groups on the edge-site carbon atoms to weaken the bonding strength at these locations. The success of the method using

hydrogen peroxide as the etchant for holey graphene manufacturing leads us to wonder if the hydrogen peroxide molecules can introduce such a process.

To confirm that hydrogen peroxide can induce the continuous growth of in-plane holes on graphene oxide, the MD simulation of graphene oxide under thermal annealing at 1000 K in Section 4.2 was adapted to mimic the etching process coupling the heating and the chemical reactions between hydrogen peroxide and graphene oxide. After each time the graphene model stabilizes under annealing, additional hydroxyl and epoxy groups were manually added to the carbon atoms in the defect areas to mimic the oxidation process brought by hydrogen peroxide, followed by another run of thermal annealing. For the whole simulation, the oxidation and annealing were repeated two and three times, respectively.

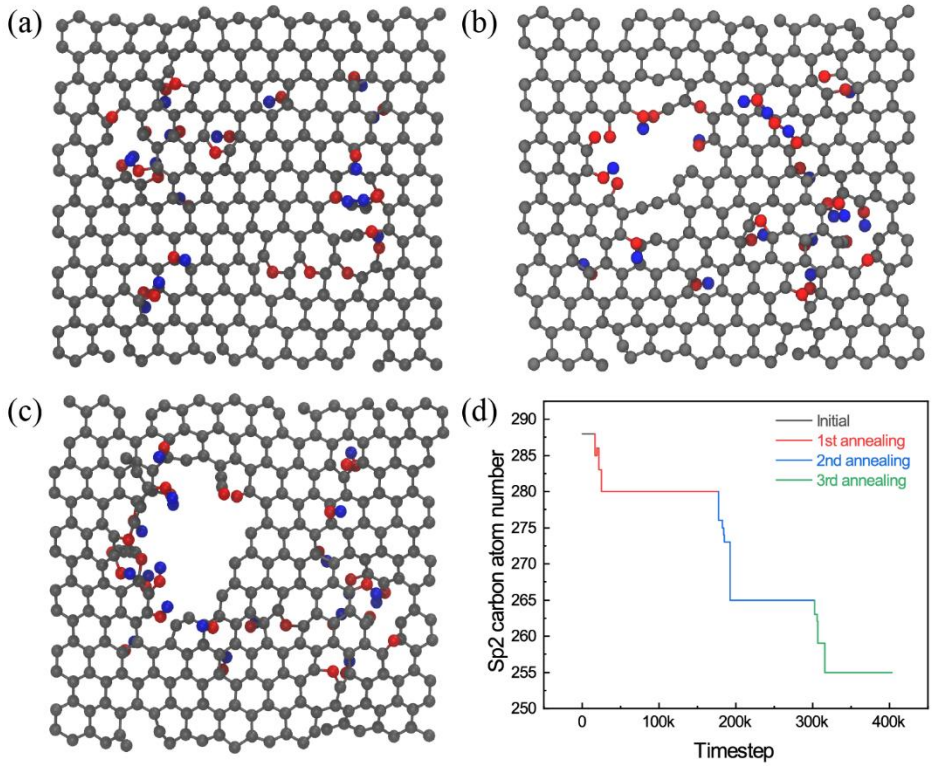

Figure 25. Molecular Dynamics Simulation of the Continuous Growth of In-plane Holes on Graphene Oxide under Cyclic Oxidation and Annealing at 1000 K. (a–c) Images of the Models after (a) the First, (b) Second, and (c) Third Annealing. (d) The Number of the Carbon Atoms in Graphitic Rings Changing with Respect to the Simulation Time.

After the first run of thermal annealing at 1000 K (**Figure 25**a), the graphene model with defect areas still stabilizes within a period of time. After oxidation and the second annealing (**Figure 25**b), the in-plane holes are enlarged, indicating the significance of oxidation for the continuous growth of the in-plane holes on graphene oxide. This can be confirmed by further repeating the oxidation and annealing processes (**Figure 25**c). **Figure 25**d shows that the removal of carbon atoms from graphitic rings on graphene oxide can be continued only when the oxidation process occurs. This result also suggests that even at a relatively low temperature (1000 K, which cannot bring large in-plane holes as demonstrated in the former Section), the oxidation can still promote the growth of holes.

5 Summary

This chapter first details the MACE method with a two-step strategy for manufacturing hGO. The products obtained in each step, pGO and hGO, are characterized by TEM, AFM, Raman, and XPS. The results are further used to evaluate the controllability of the MACE method. It is found that the durations of microwave pretreatment and MACE generate significant influences on the microstructural features of the nanoholes on hGO. The duration of pretreatment increases the defect density of pGO and the population of nanoholes on hGO. Meanwhile, the duration of MACE can be employed to control the diameter of nanoholes. To fully reveal the thermal chemical mechanism during MACE, DFT and MD calculations are carried out to study the reaction between GO and H_2O_2 and the formation process of in-plane holes on GO during heating. The calculation results help explain the continuous growth of in-plane holes on GO under the coupling effect of chemical etching and heating, and it is consistent with the experimental results.

CHAPTER 4

MICROWAVE-INDUCED SELECTIVE HEATING OF GRAPHENE OXIDE IN AQUEOUS SOLUTIONS

1 Introduction

Besides the controllability of the microstructural features of nanoholes, the MACE method for holey graphene manufacture achieves a significant reduction of processing time from hour-scale to minute-scale compared with the current solution-based methods. Microwave plays a vital role in this improvement. Therefore, this chapter aims to reveal the mechanism of the rapid processing brought by microwave. Section 2 investigates the temperature and pressure rises during microwave irradiation of various GO aqueous solutions. Section 3 reports the theoretical calculations on in situ heat generation and the dielectric properties of GO in aqueous solutions under microwave irradiation. Based on the results, Section 4 discusses the role of microwave in the MACE process for manufacturing holey graphene.

2 Microwave Heating of Graphene Oxide Aqueous Solutions

2.1 Microwave Heating of Water and Graphene Oxide Aqueous Solutions

Holey graphene manufacturing in this study is achieved in the solution environment. Therefore, to investigate the microwave heating of GO, it is crucial to compare the behaviors between water and GO aqueous solutions under microwave irradiation. To this end, deionized water and the 1 mg mL^{-1} GO aqueous solution with the same volume of 3 mL were treated by four cycles of 90-s microwave irradiation with an output power of 50 W, respectively, starting from room temperature. The cooling of each cycle ended when the temperature drops to 75 °C. It is found that the peak temperature of the GO solution (**Figure 26**a) at each end point is always higher than that of water. The pressure profiles

(**Figure 26**c) are consistent with this observation. Therefore, the heating of GO sheets in aqueous solutions under microwave irradiation is not mainly caused by the heat transfer from water molecules. The GO sheets absorb energy directly from the microwave as well. Moreover, the peak temperature of the GO solution gradually increases each cycle (neglecting the first cycle because its start temperature is 25 °C rather than 75 °C of the rest), while that of water stays at 140 °C for the rest three cycles. The consistency of the peak temperatures of water confirms the performance stability of the microwave reactor. For the GO solution, the increase of the peak temperatures suggests the microstructure of GO is affected under microwave irradiation and causes the change of its dielectric properties. According to B. Kuang et al.,[98] the higher reduction level of GO resulted in more vacancy defects and higher conductivities and thus enhanced its microwave absorbing and dielectric loss. Here, the microwave-induced mild reduction of GO (as demonstrated by XPS and Raman results in Chapter 3) also further boosts its microwave heating in the next cycle.

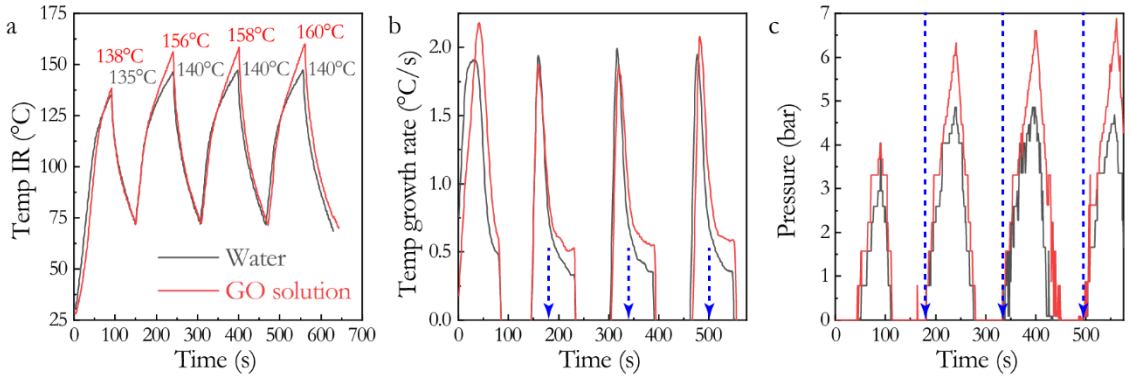

Figure 26. (a) Temperature, (b) Temperature Growth Rate, and (c) Pressure Profiles of Deionized Water (Black Curves) and the 3 mg mL^{-1} Graphene Oxide Solution (Red Curves) under Microwave Irradiation with an Output Power of 50 W. Blue dash lines indicate the start points of water evaporation.

The temperature growth rates (**Figure 26**b) of water and the GO solution both reduce to a lower level (around 0.5 °C s^{-1}) within each heating cycle, while the GO solution keeps a relatively higher rate. The critical points for the growth rate change coincide with the

start points of water evaporation, as indicated by the blue dash lines in the pressure profiles (**Figure 26**b). Thus, the drop in the temperature growth rate should be mainly attributed to the heat loss for water evaporation. Another factor causing the drop in the temperature growth rate could be the lower dielectric heating of water under higher temperatures.[125] Meanwhile, both the conduction loss and dielectric loss of GO significantly increase when the temperature reaches above 100 °C.[126] With higher temperatures, the microwave heating of water reduces, and that of GO increases, leading to the differentiation in the temperature growth rates.

2.2 Effect of Concentrations of Graphene Oxide on Microwave Heating

To investigate the effect of concentrations, three samples with the same volume (3 mL), including deionized water and two pGO aqueous solutions (obtained by microwave heating GO solutions at 50 W for 180 s) with concentrations of 1 and 3 mg mL^{-1}, were treated by microwave irradiation with the same power and duration (50 W and 120 s) starting at room temperature. No etchant was added in any of the samples to eliminate the influence of etching reactions. At 120 s, the final temperatures (**Figure 27**a) are 140, 145, and 156 °C for the deionized water, 1 mg mL^{-1}, and 3 mg mL^{-1} pGO solutions, respectively, and the final pressures (**Figure 27**b) of the three samples are 5.1, 5.7, and 7.7 bar, respectively. The addition of pGO in water enhances the total energy absorption from the electromagnetic wave, and a higher pGO concentration within the present range leads to greater energy absorption. This confirms the results from the study by B. Kuang et al.,[98] which suggested the higher mass loading of rGO enhanced the dielectric loss at the frequency around 2.45 GHz.

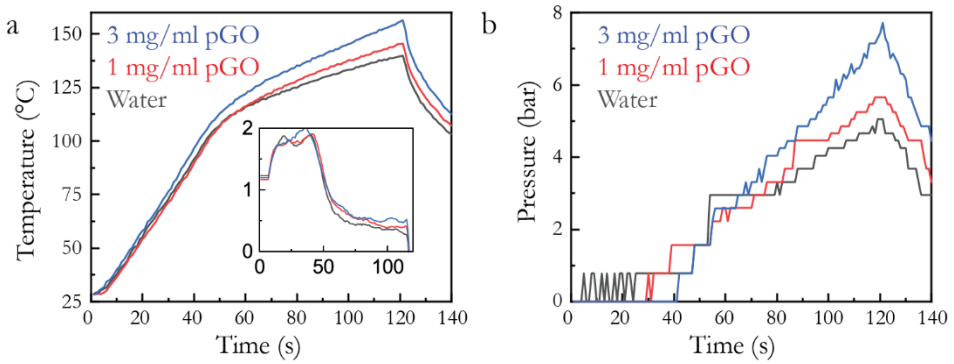

Figure 27. (a) Temperature and (b) Pressure Profiles of Deionized Water and the Pretreated Graphene Oxide Solutions with Concentrations of 1 and 3 mg mL^{-1} under Microwave Irradiation with an Output Power of 50 W. Inset in a, Temperature Growth Rate vs. Time.

2.3 Effect of Reduction Levels of Graphene Oxide on Microwave Heating

The reduction level of GO is an essential factor affecting microwave absorption. To study its effect on microwave heating of GO, the solutions of pGO and rGO with the same concentrations of 3 mg mL^{-1} were treated by microwave irradiation with an output power of 50 W for 120 s. Here, the pGO and rGO solutions were obtained by microwave heating GO solutions at 50 W for 180 s and 200 W for 180 s, respectively. The peak temperatures (**Figure 28**a) of the pGO and rGO solutions are 157 and 173 °C, respectively, and the peak pressures (**Figure 28**b) are about 7 and 11 bar. The differences should be attributed to the higher reduction level of rGO compared with pGO, because the former could allow more free electrons to move and scatter on the lattice, causing local Joule heating. As demonstrated in the introduction chapter, conduction loss-induced heating is different from polarization loss-induced heating. Here, both mechanisms could occur. The defects and functional groups of rGO can induce dipolar movements, and the regional π–π networks support electron movements. At 13 s of microwave irradiation, plasma arcs were observed in the rGO solution (**Figure 28**c). In the paper of D. Voiry et al.,[105] similar plasma arcs were observed during microwave heating rGO powder in the dry environment because free

electron movement causes local Joule heating and ionization of the surrounding molecules. The observation in this study suggests that the free electron movement can also occur when rGO sheets are dispersed in aqueous solutions. Plasma arcs were not observed in the pGO solution for the whole microwave treatment. Note that the plasma discharge is a microscopic and rapid process, which may not be observed all the time. However, the macroscopic observation adequately indicates that the intensity of the ionization process caused by the electron movement in rGO is higher than that in pGO. Therefore, the higher reduction level of GO can enhance conduction loss-induced heating.

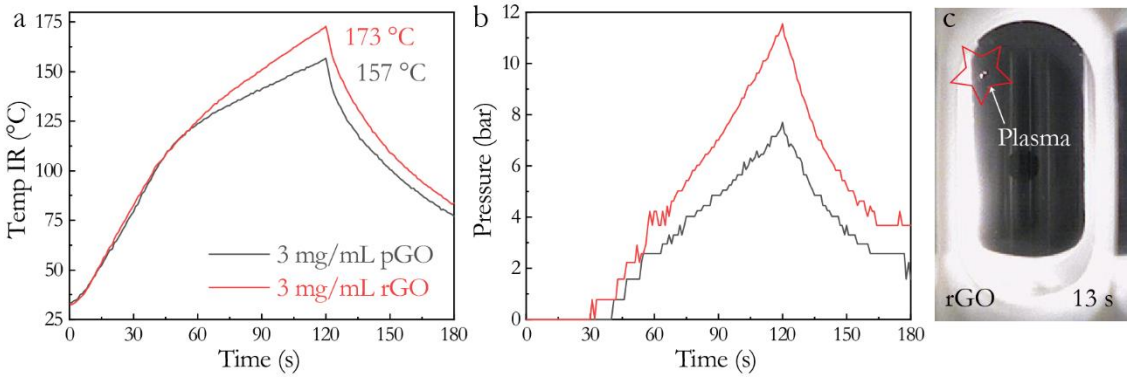

Figure 28. (a) Temperature and (b) Pressure Profiles of the Pretreated and Reduced Graphene Oxide Solutions with Concentrations of 3 mg mL^{-1} under Microwave Irradiation with an Output Power of 50 W. (c) Image of the Reduced Graphene Oxide Solution under Microwave Irradiation at 13 s, Showing the Plasma Arc Induced by the Free Electron Movement on Graphene Oxide Sheets.

3 In Situ Heat Generation and Microwave Absorption of Graphene Oxide

3.1 In Situ Heat Generation of Graphene Oxide in Aqueous Solutions

Based on the observations in the microwave irradiation experiments, GO sheets are selectively heated in aqueous solutions by the coupled heating mechanisms of the conduction loss and dielectric loss. Using the data of the temperature profiles, in situ heat generation of GO under microwave irradiation can be further calculated. The temperature rise of the GO solutions should be caused by microwave heating of water and GO. While

the real-time temperature of GO is difficult to be directly recorded under the current experimental conditions, the microwave absorption properties of GO can still be evaluated by eliminating the part of water.

Assuming that the GO solution is adiabatic (Assumption I), meaning no heat loss to the external environment, the temperature rise of the solution is only affected by dielectric heating of water and GO under microwave irradiation. The specific heat capacity of the GO solution is assumed to equal to that of pure water (Assumption II), considering the small weight percentage of GO in the solution. For simplification, the specific heat capacity of water is considered a constant within the temperature range (Assumption III). The relationship between the temperature change of the GO solution (ΔT_{sol}) and the total heat generated by the solution (Q_{sol}) is given by

$$Q_{\mathrm{sol}} = m_{\mathrm{sol}} C_{\mathrm{V,H_2O}} \Delta T_{\mathrm{sol}} \tag{13}$$

where m_{sol} is the total mass of the solution, which approximates the mass of water (m_{H2O}, 3.0 g), and $C_{V,H2O}$ is the specific heat capacity of pure water (4.19 J g^{-1} °C^{-1} at 25 °C)[127]. To calculate the total heats generated in pure water (Q_{H2O}), the pGO solutions with concentrations of 1 and 3 mg mL^{-1} ($Q_{sol\_pGO\_1}$ and $Q_{sol\_pGO\_3}$, respectively), and the rGO solution of 3 mg mL^{-1} (Q_{sol_rGO}), ΔT_{sol} is simultaneously replaced by the experimental value for water or each GO solution (shown in **Table 4**). The results are shown in the column "total heat" of **Table 4.**

Table 4. Heat Generated by Graphene Oxide in Aqueous Solutions.

Sample	Initial temp. [°C]	Final temp. [°C]	Total heat [J]	Heat from GO [J]
Water	25	140	1,445.6	\
1 mg mL^{-1} pGO solution	25	145	1,508.4	62.8
3 mg mL^{-1} pGO solution	25	156	1,646.7	201.1
3 mg mL^{-1} rGO solution	25	173	1860.4	418.8

Assuming that the heat generated by water is not affected by GO (Assumption IV), the heats solely generated by GO in these solutions can be extracted from the above results of the total heats of the solutions using the equations,

$$Q_{\mathrm{pGO\_1}} = Q_{\mathrm{sol\_pGO\_1}} - Q_{\mathrm{H_2O}} \quad (14)$$

$$Q_{\mathrm{pGO\_3}} = Q_{\mathrm{sol\_pGO\_3}} - Q_{\mathrm{H_2O}} \quad (15)$$

$$Q_{\mathrm{rGO}} = Q_{\mathrm{sol\_rGO}} - Q_{\mathrm{H_2O}} \quad (16)$$

The results are shown in the column "Heat from GO" of **Table 4.**

The specific heat capacity of rGO[128, 129] and GO[130], $C_{\mathrm{V,rGO}}$ and $C_{\mathrm{V,GO}}$, at room temperature is about 0.70 and 1.75 J g^{-1} $°C^{-1}$, respectively. In the following calculation, it is assumed that the specific heat capacity is a constant within the temperature range in the experiments (Assumption V). Therefore, the temperature growth of GO solely depending on the heat generated by itself can be estimated using the equation,

$$\Delta T_{\mathrm{GO}} = Q_{\mathrm{GO}}/m_{\mathrm{GO}}C_{\mathrm{V,GO}} \quad (17)$$

where m_{GO} is the mass of GO in the solution. The results are shown in **Table 5**.

Table 5. Temperature Rise of GO Solely Depending on the Heat from Itself.

Material	C_v a) [J g^{-1} $°C^{-1}$]	Weight [g]	Final temp. [°C]
pGO in 1 mg mL^{-1} solution	1.75	0.003	11,936
pGO in 3 mg mL^{-1} solution	1.75	0.009	12,743
rGO in 3 mg mL^{-1} solution	0.70	0.009	66,451

a) Specific heat capacity of GO and rGO. Data from ref[128, 129, 130].

Note that the temperature calculation only considers the heat generation of GO without heat conduction to water. Therefore, the results of the temperatures are dramatically high. Judging from another angle, the heating process of GO solutions involving these results can be regarded as the cases that the GO sheets and water are separately heated and then mixed together to achieve the final temperature (illustrated in **Figure 29**b). In the actual

case (**Figure 29**b), the heat generated by a GO sheet should be quickly conducted to the surrounding water molecules (**Figure 29**c), meaning there should be a temperature balance at the interface between a GO sheet and the water molecules.

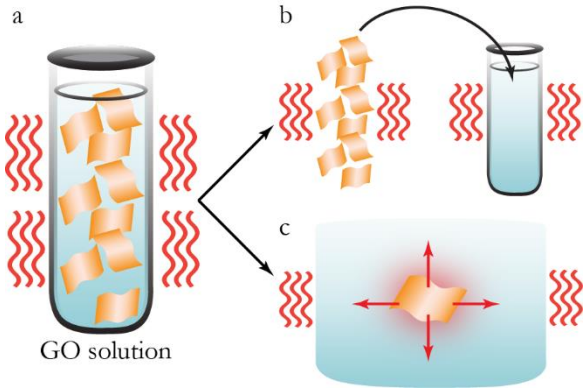

Figure 29. Calculation Models of the Microwave Heating of Graphene Oxide Solutions: (a) Schematic of the Real Case; (b) Graphene Oxide and Water are Separately Heated and Then Mixed; (c) Temperature Difference between Graphene Oxide and Water is Balanced While They are Separately Heated.

3.2 Temperature Difference between Graphene Oxide and Water under Microwave Irradiation

Now, the model illustrated in **Figure 29**c is employed to calculate the temperature difference between GO and water under microwave irradiation. Considering the uniform dispersion of GO sheets in the solutions, the temperatures of a GO sheet and the water molecules are assumed to be instantly balanced (Assumption VI). The heat generated by GO per unit time ($\partial Q_{GO}/\partial t$) is conducted to water and causes an instant decrease of GO temperature ($\partial \Delta T_{GO}/\partial t$). The relationship of the energy balance is given by

$$\partial Q_{GO}/\partial t = m_{GO} C_{V,GO} (\partial \Delta T_{GO}/\partial t) \quad (18)$$

With the constant output power of the microwave reactor, the heat generated by GO per unit time should be a constant ($\partial Q_{GO}/\partial t$ = constant) through the whole process of microwave irradiation. The heating power of GO (P_{GO}, J s^{-1}) can be written as

$$P_{\mathrm{GO}} = \partial Q_{\mathrm{GO}}/\partial t = \text{constant} = Q_{\mathrm{GO}}/t_{\mathrm{f}} \quad (19)$$

where t_f is the total time of microwave irradiation (120 s). The results are shown in **Table 6**.

Table 6. Temperature Difference between Graphene Oxide and Water.

Material	Heating power [W]	Temperature difference [°C]
Water	12.05	\
pGO in 1 mg mL^{-1} solution	0.52	99.8
pGO in 3 mg mL^{-1} solution	1.68	106.4
rGO in 3 mg mL^{-1} solution	3.49	554.0

It is found that the temperature decrease of GO per unit time is also a constant by combing Equation 18 and 19 to obtain the relationship,

$$\partial \Delta T_{\mathrm{GO}}/\partial t = P_{\mathrm{GO}}/m_{\mathrm{GO}} C_{V,\mathrm{GO}} = \text{constant} \quad (20)$$

It means that the temperature of GO reduces from a high value to the temperature of the surrounding water every second, and this instant temperature decrease does not change with time, expressed as

$$\partial \Delta T_{\mathrm{GO}}/\partial t = (T_{\mathrm{GO}} - T_{\mathrm{H_2O}})/\Delta t = \text{constant} \quad (21)$$

By combining Equation 20 and 21, the instant temperature difference between GO and water in each GO solution can be calculated from

$$\Delta T_{\mathrm{pGO\_1}} = T_{\mathrm{pGO\_1}} - T_{\mathrm{H_2O}} = Q_{\mathrm{pGO\_1}}/t_{\mathrm{f}} m_{\mathrm{pGO\_1}} C_{V,\mathrm{GO}} \quad (22)$$

$$\Delta T_{\mathrm{pGO\_3}} = T_{\mathrm{pGO\_3}} - T_{\mathrm{H_2O}} = Q_{\mathrm{pGO\_3}}/t_{\mathrm{f}} m_{\mathrm{pGO\_3}} C_{V,\mathrm{GO}} \quad (23)$$

$$\Delta T_{\mathrm{rGO}} = T_{\mathrm{rGO}} - T_{\mathrm{H_2O}} = Q_{\mathrm{rGO}}/t_{\mathrm{f}} m_{\mathrm{rGO}} C_{V,\mathrm{GO}} \quad (24)$$

The results are shown in **Table 6** and illustrated in **Figure 30**. Under microwave irradiation, the temperature of pGO is constantly 100 °C higher than water, and the temperature difference increases with the concentration. The temperature difference between rGO and water is significantly higher (554 °C) than that between pGO and water, confirming the heat generation of GO under microwave irradiation can be enhanced with a higher reduction

level. Note that the temperature elevation of pGO or rGO is not from the room temperature because this model assumes an instant temperature balance between GO and water, causing the temperature difference is independent with time.

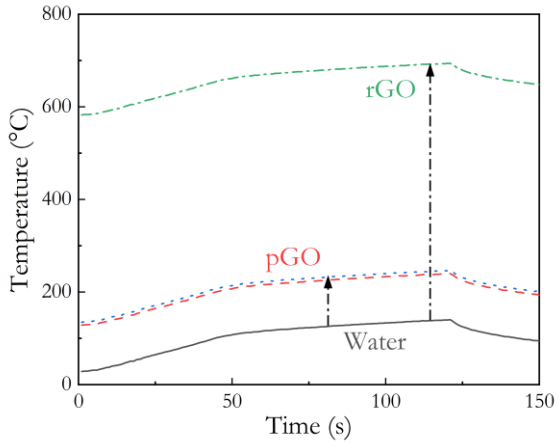

Figure 30. Temperature Difference of Graphene Oxide and Water. Demonstrated by the Temperature Profiles of Water (Black Curve), Pretreated Graphene Oxide in the Solutions with concentrations of 1 and 3 mg mL^{-1} (Red and Blue Curves), and Reduced Graphene Oxide (Green Curve).

3.3 Dielectric Loss of Graphene Oxide

The gravimetric and volumetric heating power (P_G and P_V) of GO and water can be calculated using

$$P_G = P/m \tag{25}$$

$$P_V = P/V \tag{26}$$

and the results are shown in **Table 7**.

Table 7. Heating Power and Dielectric Loss Factor of Graphene Oxide.

Material	Gravimetric power [W g^{-1}]	Volumetric power [W cm^{-3}]	Dielectric loss Factor
Water	4.02	4.02	12[a)]
pGO in 1 mg mL^{-1} solution	173	76	227
pGO in 3 mg mL^{-1} solution	186	82	244
rGO in 3 mg mL^{-1} solution	388	171	511

a) Using data from ref[131].

Using Equation 4 from the introduction chapter, the electric field strength of microwave irradiation, E_{MW}, can be calculated from

$$E_{\mathrm{MW}} = \sqrt{P_{\mathrm{V,H_2O}}/\pi f \varepsilon_0 \varepsilon''_{\mathrm{H_2O}}} \quad (27)$$

where ε_{H2O}" is the dielectric loss factor (the imaginary part of the complex permittivity) of water (12 at room temperature)[131]. The calculation result is E_{MW} = 2217.15 V m^{-1}. Then, the dielectric loss factors of pGO and rGO in various solutions can be calculated using the same relationship

$$\varepsilon''_{\mathrm{pGO\_1}} = P_{\mathrm{V,pGO\_1}}/\pi f \varepsilon_0 E^2_{\mathrm{MW}} \quad (28)$$

$$\varepsilon''_{\mathrm{pGO\_3}} = P_{\mathrm{V,pGO\_3}}/\pi f \varepsilon_0 E^2_{\mathrm{MW}} \quad (29)$$

$$\varepsilon''_{\mathrm{rGO}} = P_{\mathrm{V,rGO}}/\pi f \varepsilon_0 E^2_{\mathrm{MW}} \quad (30)$$

The results are shown in **Table 7**.

3.4 Microwave Absorption of Graphene Oxide Aqueous Solutions

The total output energy of the microwave reactor is W_{MW} = 50 W × 120 s = 6,000 J. Then, microwave absorption of pure water and the GO solutions can be calculated from the following equations,

$$\alpha_{\mathrm{H_2O}} = Q_{\mathrm{H_2O}}/W_{\mathrm{MW}} \quad (31)$$

$$\alpha_{\mathrm{sol\_pGO\_1}} = Q_{\mathrm{sol\_pGO\_1}}/W_{\mathrm{MW}} \quad (32)$$

$$\alpha_{\mathrm{sol\_pGO\_3}} = Q_{\mathrm{sol\_pGO\_3}}/W_{\mathrm{MW}} \quad (33)$$

$$\alpha_{\mathrm{sol\_rGO}} = Q_{\mathrm{sol\_rGO}}/W_{\mathrm{MW}} \quad (34)$$

The results are shown in the "microwave absorption" column of **Table 8**. The calculated microwave absorption of pure water is 0.241, which is smaller than the theoretical value at room temperature, $\alpha_{\mathrm{H_2O,theoretical}} = \pi\varepsilon''/\lambda\sqrt{\varepsilon'} = 0.349$. This should be correlated to the

Table 8. Microwave Absorption of Graphene Oxide Aqueous Solutions.

Solution	Heat [J]	Microwave absorption	Corrected heat [J]	Corrected volumetric heating power [W cm^{-3}]	Corrected microwave absorption
Water	1,445.6	0.241	2,094 [a)]	5.82 [a)]	0.349 [a)]
1 mg mL^{-1} pGO solution	1,508.4	0.251	2,156.9	5.99	0.359
3 mg mL^{-1} pGO solution	1,646.7	0.274	2,295.1	6.38	0.383
3 mg mL^{-1} rGO solution	1,860.4	0.310	2,508.8	6.97	0.418

a) Using data from ref[131].

heat loss of the solution or water to the external environment, causing the reduction in energy absorption. Now, Assumption I (the system is adiabatic) can be withdrawn, and the effect of the heat loss is considered for all solutions. The theoretical heat generated by water and the heat loss of water to the external environment can be calculated using the theoretical value of microwave absorption of water as shown below.

$$Q_{\mathrm{H_2O,theoretical}} = \alpha_{\mathrm{H_2O,theoretical}} W_{\mathrm{MW}} = 2{,}094\ \mathrm{J} \tag{35}$$

$$Q_{\mathrm{loss}} = Q_{\mathrm{H_2O,theoretical}} - Q_{\mathrm{H_2O}} = 648.4\ \mathrm{J} \tag{36}$$

Assuming the heat losses to the external environment for pure water and the GO solutions are the same (Assumption VII), the heat generated by the whole solution should be larger than the current calculation results. Therefore, the heat loss should be added to the actual heat generation of the GO solutions. The corrected heat generation, volumetric heating power, and microwave absorption of the GO solutions are shown in **Table 8**. Then, the volumetric heating power of water under microwave irradiation considering the heat loss is $P_{V,\mathrm{theoretical}} = Q_{\mathrm{H_2O,theoretical}}/t_{\mathrm{f}} V_{\mathrm{water}} = 5.82\ \mathrm{W\ cm^{-3}}$, and the corrected electric field strength of microwave irradiation is $E_{\mathrm{MW,corrected}} = \sqrt{P_{V,\mathrm{theoretical}}/\pi f \varepsilon_0 \varepsilon''} = 2667.74\ \mathrm{V\ m^{-1}}$. Now, the dielectric loss factors of the GO solutions can be calculated using the following equations,

$$\varepsilon''_{\mathrm{sol\_pGO\_1}} = P_{\mathrm{V,sol\_pGO\_1,corrected}}/\pi f \varepsilon_0 E^2_{\mathrm{MW,corrected}} \tag{37}$$

$$\varepsilon''_{\text{sol\_pGO\_3}} = P_{\text{V,sol\_pGO\_3,corrected}}/\pi f \varepsilon_0 E^2_{\text{MW,corrected}} \quad (38)$$

$$\varepsilon''_{\text{sol\_rGO}} = P_{\text{V,sol\_rGO,corrected}}/\pi f \varepsilon_0 E^2_{\text{MW,corrected}} \quad (39)$$

The results are shown in the "dielectric loss factor" column of **Table 9**. Since now we have the dielectric loss factors and microwave absorption of the GO solutions, the dielectric constant (the real part of the complex permittivity) of the GO solutions can be calculated using the relationship,

$$\varepsilon'_{\text{sol\_GO}} = \left(\pi \varepsilon''_{\text{sol\_GO}}/\lambda\right)^2/\alpha_{\text{sol\_GO}} \quad (40)$$

The results are shown in **Table 9**.

Table 9. Dielectric Properties of Graphene Oxide Aqueous Solutions.

Solution	Dielectric loss factor	Dielectric constant
1 mg mL^{-1} pGO solution	12.35	2,202
3 mg mL^{-1} pGO solution	13.15	2,340
3 mg mL^{-1} rGO solution	14.37	2,560

4 Discussion on Microwave-assisted Chemical Etching of Graphene Oxide

The results above can be employed to demonstrate the mechanism involved in the rapid fabrication of holey graphene via MACE. The selective heating of GO sheets by microwave irradiation is the essential advantage of the MACE method over the conventional one. As shown in **Figure 31**, the conventional heating method strongly depends on heat conduction and convection within the solution. The heating of a GO sheet is achieved after the heating of its surrounding molecules. In this case, the hydrogen peroxide molecules used as the etchant for holey graphene manufacturing can be decomposed before they can react with GO. In contrast, the microwave irradiation during MACE directly interacts with GO sheets, which quickly become the hot spots dispersed in the solution due to in situ heat generation, providing constant energy to facilitate the etching reaction with the surrounding

hydrogen peroxide molecules. This also implies that both the process efficiency and controllability could be modulated by microwave irradiation during the MACE process.

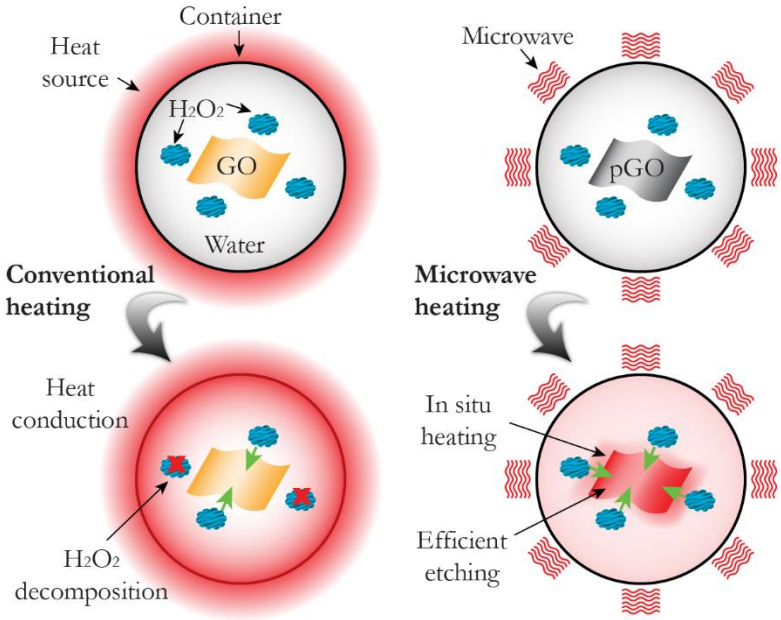

Figure 31. Role of Microwave Heating in Holey Graphene Manufacturing.

5 Summary

The MACE method was demonstrated as a promising solution for scalable manufacturing of holey graphene by reducing the total processing time. The rapid process was attributed to the in situ heat generation and selective heating of GO sheets under microwave irradiation. By the comparison studies, Section 2 demonstrated the selective heating process of GO in aqueous solutions under microwave irradiation due to the coupling effect of polarization and conduction losses. Higher concentrations and reduction levels enhanced the microwave heating of GO in aqueous solutions. The theoretical calculations in Section 3 suggested that microwave irradiation caused in situ heat generation of GO in aqueous solutions, resulting in the temperature difference between GO and its surrounding water molecules. The calculation results on the dielectric loss factors of GO or its solutions confirmed the contributions of concentrations and reduction level to microwave heating.

CHAPTER 5

HIGH-PERFORMANCE ELECTROCHEMICAL ENERGY STORAGE AND ELECTROCATALYSIS ENABLED BY HOLEY GRAPHENE

1 Introduction

To demonstrate the electrochemical property improvements of holey graphene manufactured via MACE, this chapter offers evaluations on its capacitive energy storage performance and electrocatalytic activity, two main fields of the holey 2D material research. Section 2 reports the performance of holey graphene in supercapacitors, starting with the three-electrode measurements to investigate the capacitor-related properties of the rhGO electrode. Besides the comparison study with the non-holey rGO electrode, the rhGO electrodes manufactured with different durations of pretreatment and MACE are also compared with each other to reveal the effects of processing and microstructure on electrochemical properties of holey graphene. To test the performance in practical devices, the SSCs are assembled using rhGO as the electrodes. Comparison studies are performed as well. In Section 3, the electrocatalytic activity of rhGO is evaluated using the three-electrode method to demonstrate the application potential of holey graphene manufacture via MACE in electrocatalytic devices.

2 Holey Graphene for Supercapacitors

2.1 Electrode Property

The capacitive performance of rhGO was measured in the 1 M Na_2SO_4 aqueous electrolyte with a three-electrode setup. Five samples were used to prepare the rhGO electrodes with different processing parameters, which are rhGO-PS (pretreated for 90 s and etched for 90 s), -PL (pretreated for 360 s and etched for 90 s), -M (pretreated for 180 s and etched for 90 s), -ES (pretreated for 180 s and etched for 45 s), and -EL (pretreated for 180 s

and etched for 180 s). The reduction is achieved by microwave irradiation at 220 °C for 90 s without any reduction agent. For comparison, rGO was also prepared with the same reduction process.

2.1.1 Cyclic Voltammetry

Figure 32a,b shows the CV curves of the rGO and rhGO-M electrodes obtained at scan rates of 5–50 mV s^{-1} and a potential window from −0.2 to 0.8 V. Both the EDLC and pseudocapacitance mechanisms contribute to the capacitive energy storage behavior of the rGO and rhGO-M electrodes. The redox peaks induced by the pseudocapacitance of the functional groups on graphene sheets are observed in the CV curves of the rGO and rhGO-M electrodes at a potential range from −0.2 to 0.2 V. At higher potentials, the current is relatively stable in response with potential scanning, which is the typical EDLC behavior.

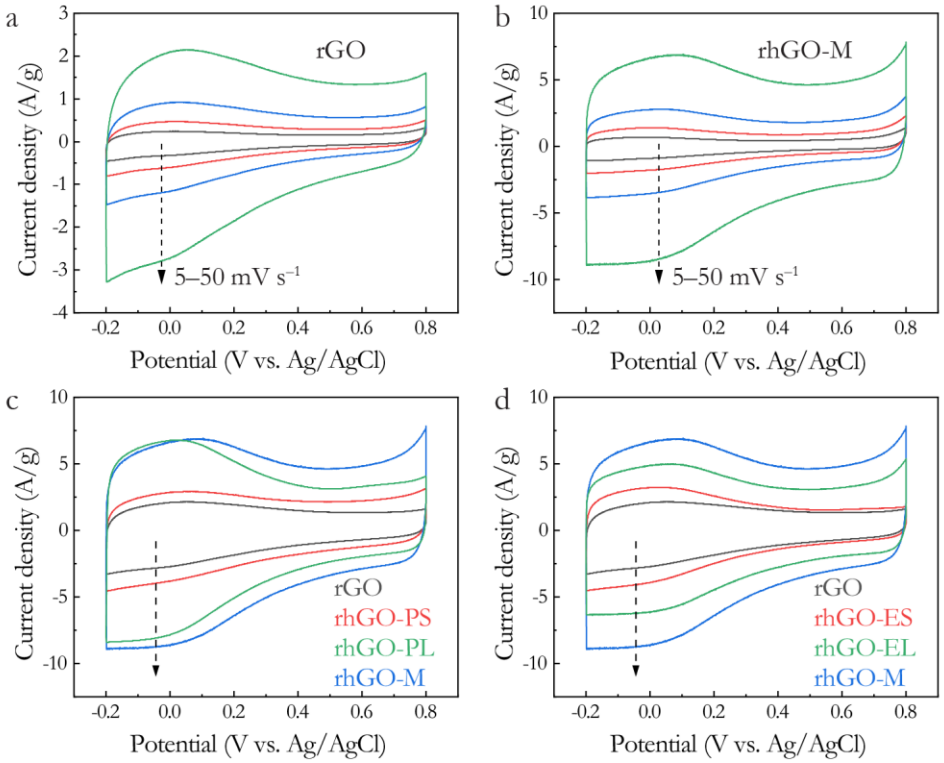

Figure 32. Cyclic Voltammetry Curves of (a) Reduced Graphene Oxide (rGO) and (b) Holey rGO (rhGO) in 1 M Sodium Sulfide at Scan Rates of 5–50 mV s^{-1}. Curves of rhGO with Different Durations of (c) Pretreatment and (d) MACE at a Scan Rate of 50 mV s^{-1}.

As indicated by the enclosed areas of the CV curves, the specific capacitances of the rhGO-M electrode at all scan rates are higher than those of the rGO electrode. At a scan rate of 50 mV s^{-1}, the specific capacitance of rhGO-M calculated from CV curves is 111 F g^{-1} (**Table 10**), about 3.5 times that of rGO (32 F g^{-1}). Note that the capacitance of rGO here is relatively low compared to existing reports,[1] owing to the mild reduction level of GO prepared without any reduction agent. Nevertheless, this reduction level is enough to exhibit the significant improvement in capacitive performance brought by the nanoholes. Compared with rGO, rhGO provides a larger accessible surface area for double-layer electrolyte adsorption and more electrochemically active sites to promote the pseudocapacitance.

Table 10. Electrochemical Properties of Reduced Holey Graphene Oxide.

Material	$C_{S,CV}$ [a] [F g^{-1}]	$C_{S,GCD}$ [b] [F g^{-1}]	R_{CT} [Ω]	D_W [× 10^{-9} cm^2 s^{-1}]
rGO	32	25	18	0.17
rhGO-M	111	112	17	3.83
rhGO-PS	48	46	17	1.84
rhGO-PL	91	84	17	2.52
rhGO-ES	44	42	17	1.05
rhGO-EL	77	72	16	2.62

[a] $C_{S,CV}$ is calculated from the CV curve measured at 50 mV s^{-1}; [b] $C_{S,GCD}$ is calculated from the GCD curve measured at 10 A g^{-1}.

The electrodes of rhGO fabricated with different durations of pretreatment or MACE all show higher specific capacitance than that of the GO electrode (**Figure 32**c,d). Among rhGO, rhGO-M featuring a high population and moderate area percentage of nanoholes shows the highest specific capacitance. In the group of rhGO with different pretreatment durations (**Figure 32**c), i.e., rhGO-PS, -M, and -PL, the increase of pretreatment duration from 90 to 180 s significantly improves the specific capacitance, while the increase from 180 to 360 s leads to a small drop of the specific capacitance. By checking the microstructure features of these rhGO sheets, the improvement should be mainly attributed to the higher nanohole population, which can benefit both ion diffusion and

charge transfer. The drop of capacitive performance should relate to the area percentage of nanoholes, which could be too high on rhGO-PL. The high area percentage of nanoholes brings more active sites adsorbed by functional groups and thus hinders the reduction process. This can be confirmed by the high redox peak in the CV curve of rhGO-PL. Its capacitance from the EDLC part at high potentials is lower than that of rhGO-M, so its pseudocapacitance should be higher than that of rhGO-M to result in the redox peak with the same height relative to rhGO-M. In the group of rhGO with different MACE durations (**Figure 32**d), i.e., rhGO-ES, -M, and -EL, a similar trend is observed. Although rhGO-EL has a nanohole population over 1000 μm^{-2}, its specific capacitance is still lower than that of rhGO-M.

2.1.2 Galvanostatic Charge and Discharge

Figure 33a shows the specific capacitance obtained from the GCD results of the rGO and rhGO electrodes at current densities of 0.5–100 A g^{-1} and a potential window from −0.2 to 0.8 V. At a current density of 0.5 A g^{-1}, the specific capacitance of rhGO-M is 137 F g^{-1}, 4 times of that of rGO (33.8 F g^{-1}). The specific capacitance of both electrodes decreases with a higher current density, while the drop of rhGO-M's specific capacitance is slower than the rest of them. When the current density increases to as high as 100 A g^{-1}, the rhGO-M electrode retains a large fraction (69%) of its initial specific capacitance, while the specific capacitance retention of rGO is lower (54%). This result implies the better rate capability of rhGO, contributed by the better electrode kinetics of rhGO. Among the rhGO electrodes, all GCD curves at a current density of 10 A g^{-1} (**Figure 33**b) are near triangular. The specific capacitance data (**Table 10**) agree well with the CV results. The lower slopes in the low-voltage range should be caused by the enhancement from rhGO's pseudocapacitance, which relates to the functional groups and nanoholes.

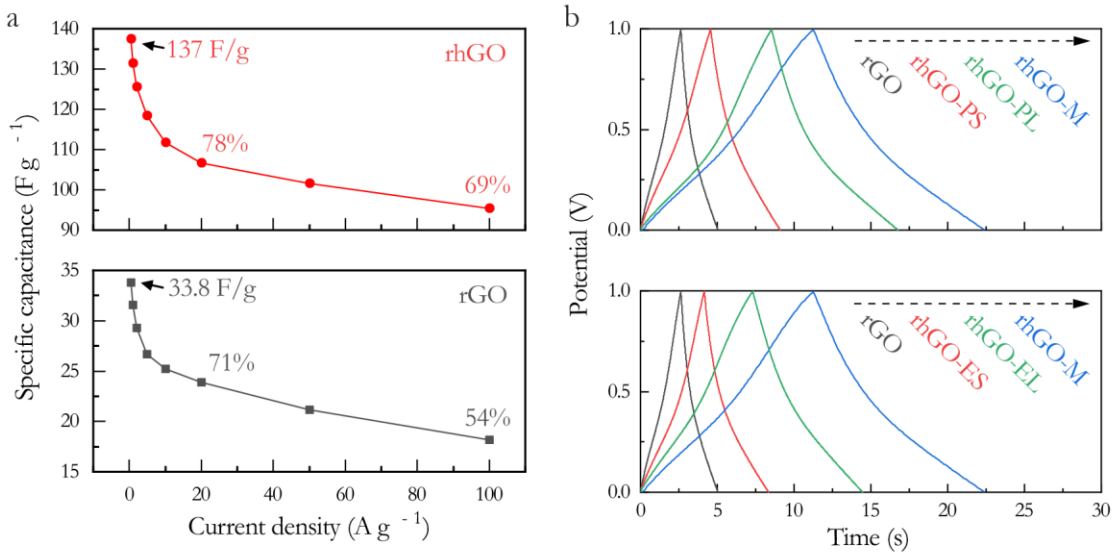

Figure 33. (a) Specific Capacitance Obtained from Galvanostatic Charge and Discharge Curves of Reduced Graphene Oxide (rGO) and Holey rGO (rhGO) in 1 M Sodium Sulfide at Current Densities of 0.5–100 A g^{-1}. (b) Galvanostatic Charge and Discharge Curves of rGO and rhGO with Different Durations of Pretreatment and MACE at a Current Density of 10 A g^{-1}.

2.1.3 Electrochemical Impedance Spectroscopy

The EIS measurements were employed to analyze the kinetic process of ion diffusion and charge transfer at the electrode–electrolyte interface. In the Nyquist plot (**Figure 34**a), the radius of the semicircle in the high-frequency range is proportional to the heterogeneous-charge-transfer resistance (R_{CT}) at the electrode–electrolyte interface. The slope of the curve in the low-frequency range increase reversely with the Warburg resistance (W) reflecting the ion diffusion process.[132, 133] The curves were fitted using the modified Randles circuit[134] (inset in **Figure 34**a) that includes a resistor for the equivalent series resistance (R_S) composed of the solution, contact, and intrinsic resistance of the electrode, a constant phase element due to the limit capacitance (CPE_L), a CPE caused by EDLC (CPE_{DL}), a resistor for R_{CT}, and a Warburg impedance element (W). The R_S values of the rhGO and rGO electrodes are within a small range of 2.3–2.4 Ω, because the solution and

contact resistances and the reduction level of all samples are very close to each other. The rhGO and rGO electrodes also have similar R_{CT} values of 16–18 Ω (**Table 10**), while the rhGO electrode displays a faster diffusion-controlled process as indicated by the higher slope in the low-frequency range (**Figure 34**a).

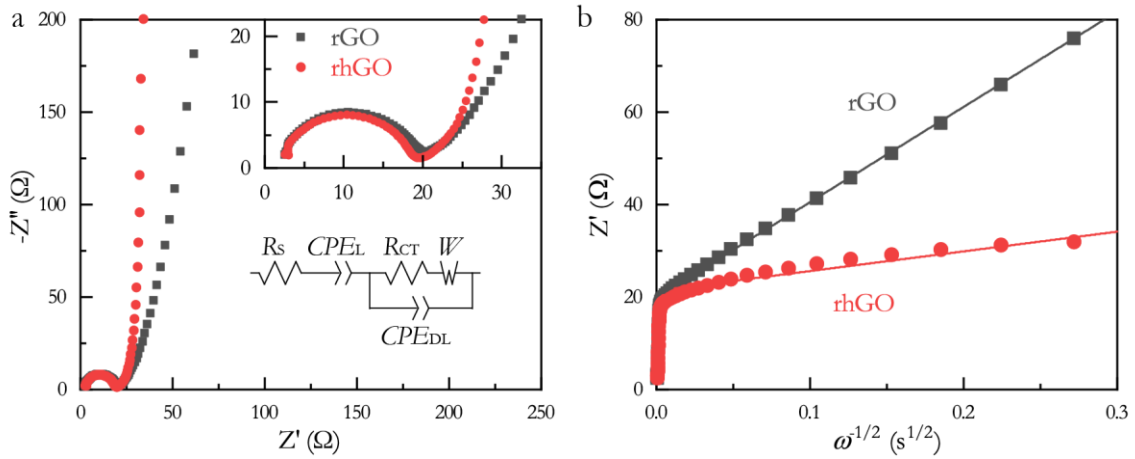

Figure 34. (a) Nyquist Plot and (b) Warburg Plot of Reduced Graphene Oxide (rGO) and Holey rGO (rhGO) in 1 M Sodium Sulfide. Insets in a Are the Equivalent Circuit and the Magnified Plot in the High-frequency Range.

To quantify the ion diffusion rate in the rhGO and rGO electrodes, the ion diffusion coefficient is calculated via the equation,[27, 118, 132]

$$D_W = [RT/(n^2F^2Ac\sigma_W)]^2/2 \quad (41)$$

where D_W is the ion diffusion coefficient ($cm^2\ s^{-1}$) calculated using the Warburg coefficient σ_W ($\Omega\ s^{-1/2}$), R is the gas constant (8.314 J K^{-1} mol^{-1}), T is the temperature (K), n is the number of electron transfer (here is 1), F is the Faraday constant (96,485.332 C mol^{-1}), A is the geometric surface area of the electrode (cm^2), and c is the concentration of Na^+ ions (mol mL^{-1}). σ_W can be further obtained from the equation,[132]

$$Z' = (R_S + R_{CT}) + \sigma_W\omega^{-1/2} \quad (42)$$

where Z' is the real part of the impedance (Ω) and ω is the frequency (s^{-1}). By plotting Z' versus $\omega^{-1/2}$ (i.e., the Warburg plot), σ_W can be calculated from the slope of the curve in the

low-frequency range. Per Equations 41 and 42, a lower slope in the Warburg plot results in a smaller σ_W and higher D_W. As shown in **Figure 34**b and **Figure 35**a,b, the rhGO electrodes all have lower slopes relative to the rGO counterpart. The calculation results (**Table 10**) show that all the D_W values of rhGO are generally an order of magnitude higher than that of rGO. Among them, rhGO-M exhibits the highest value of 3.83×10^{-9} cm^2 s^{-1}, about 20 times that of rGO (0.17×10^{-9} cm^2 s^{-1}). It demonstrates that the nanoholes significantly facilitate the ion diffusion kinetics by providing abundant ion transport shortcuts through the rhGO sheets. Among the rhGO electrodes with different duration of pretreatment and MACE, the trend of D_W agrees well with that of specific capacitance calculated from both the CV and GCD curves. The large population and moderate area percentage of nanoholes on rhGO are favorable to obtain a high ion diffusion rate.

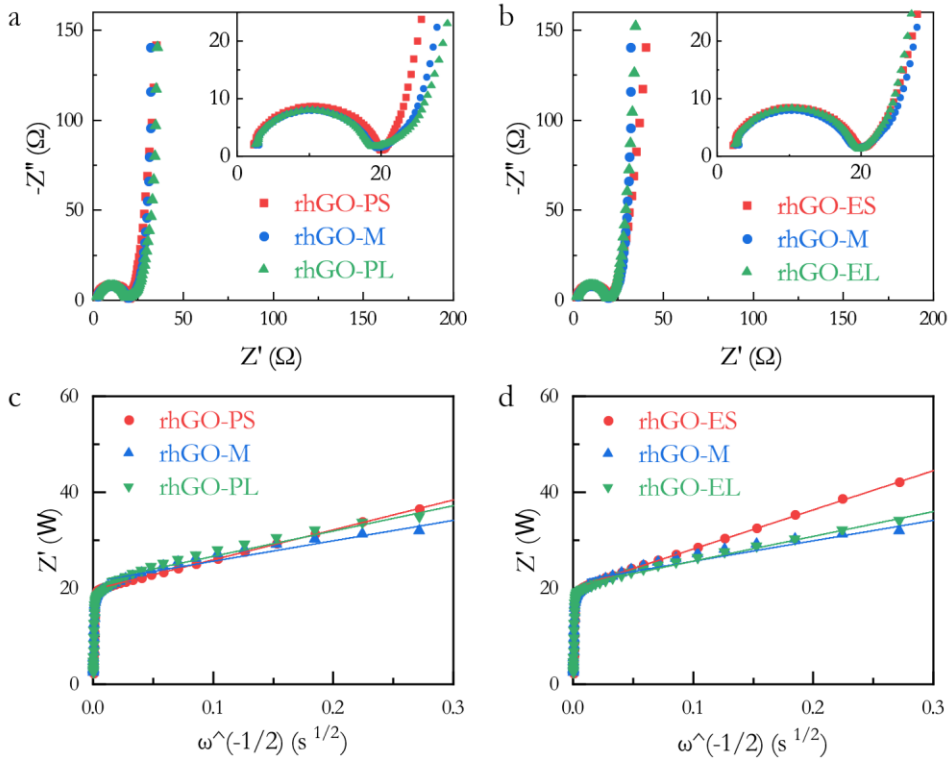

Figure 35. (a,b) Nyquist Plots and (c,d) Warburg Plots of (a,c) rhGO-P and (b,d) rhGO-E Measured in 1 M Sodium Sulfide.

2.2 Performance of Symmetric Supercapacitors

The electrochemical performance of the SSC using rhGO as the electrodes was measured with 1 M H_2SO_4 as the electrolyte and compared with that using rGO (reduced from GO with the same parameters by the hydrazine method described in Chapter 2). Due to the high reduction level of rGO and rhGO sheets, the CV curves of the SSCs (**Figure 36**a,b) are more rectangular than those reported in the last subsection. The CV curves of rGO show smaller enclosed areas at all scan rates than those of rhGO, indicating the relatively higher capacitance of the rhGO SSC. The curve shape of rGO is highly symmetric, showing the typical EDLC behavior, while that of rhGO has an enhanced current plateau in the potential range of 0.2–0.4 V, which relates to the pseudocapacitance of rhGO. At the same scan rate of 100 mV s^{-1} (blue curves), the current density of rhGO shows faster responses than that of rGO during positive or negative scanning. This should be caused by the faster electrode kinetics (including ion transport and charge transfer) of the rhGO electrode. By converting the current density into the specific capacitance per unit potential using Equation 9 in Chapter 2, it is more convenient to compare the capacitive behavior under different scan rates. With higher scan rates, it is more difficult for the ion diffusion rate to catch up with the potential change rate. Therefore, CV at high scan rates assists in revealing the ion diffusion kinetics of the SSC. For the rGO SSC (**Figure 36**c), the capacitance in the full potential range decreases with the scan rate. For the rhGO SSC (**Figure 36**d), besides the drops around the reversal potentials, the capacitance shows much better stability concerning the potential change. The specific capacitance of the SSCs of rGO and rhGO calculated from the CV curves are shown in **Table 11**. At a scan rate of 20 mV s^{-1}, the rhGO SSC exhibits a specific capacitance of 160 F g^{-1}, 1.6 times that of the rGO

SSC. Moreover, the specific capacitance of the rhGO SSC drops much slower with the scan rate relative to that of the rGO SSC.

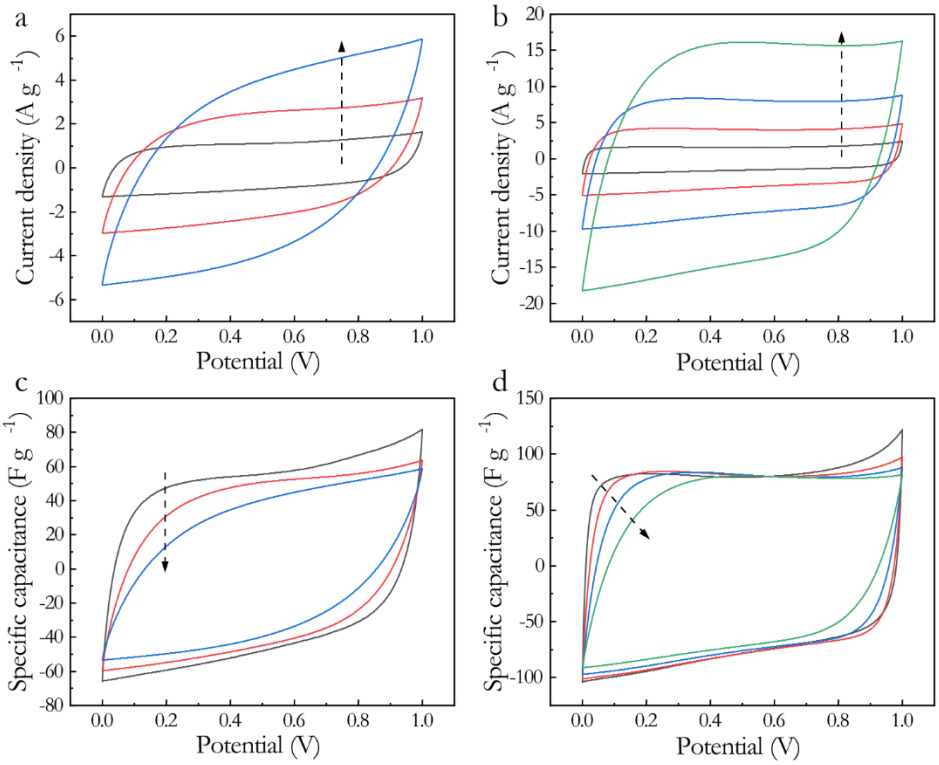

Figure 36. Cyclic Voltammetry of Symmetric Supercapacitors using Reduced Graphene Oxide (rGO) and Holey rGO (rhGO) as the Electrodes, respectively. Current Density vs. Potential of (a) rGO and (b) rhGO. Specific Capacitance Per Unit Potential vs. Potential of (c) rGO and (d) rhGO. Arrows Indicate the Direction of the Scan Rate Increase: 20 (Black), 50 (Red), 100 (Blue), and 200 (Green) mV s^{-1}.

Table 11. Specific Capacitance of the Reduced Graphene Oxide (rGO) and Holey rGO (rhGO) Electrodes in Symmetric Supercapacitors Calculated from Cyclic Voltammetry Curves.

SSC	$C_{S,CV}$ at 20 mV s^{-1} [F g^{-1}]	$C_{S,CV}$ at 50 mV s^{-1} [F g^{-1}]	$C_{S,CV}$ at 100 mV s^{-1} [F g^{-1}]
rGO	100	86	73
rhGO	160	157	149

GCD curves of the SSC devices were measured to study the energy storage performance. Besides rGO, the SSC electrode materials included two rhGO samples with a low (rhGO-LP) and high (rhGO-HP) density of in-plane nanoholes, which was achieved by changing pretreatment parameters as demonstrated in Chapter 3. The GCD results in

Figure 37a and **Table 12** suggest that the rhGO SSCs have much better specific capacitance at any current density than the rGO SSC. As the current density increases from 1 to 20 A g^{-1}, the specific capacitance of the rhGO-HP SSC shows the lowest decrease. While the rhGO-LP SSC has a comparable value (170 F g^{-1}) to rhGO-HP (171 F g^{-1}) at a relatively low current density of 1 A g^{-1}, its specific capacitance drops faster with higher current densities. At a current density of 20 A g^{-1}, the rhGO-HP SSC still maintains a specific capacitance of 141 F g^{-1}, and that of rhGO-LP SSC drops to 125 F g^{-1}. This result indicates the faster electrode kinetics of the rhGO-HP SSC relative to the rhGO-LP SSC. **Figure 37**b shows the EIS Nyquist plot of the rhGO-LP and rhGO-HP SSCs, showing obvious different behaviors in the high-frequency range. The charge transfer resistance (R_{CT}) of the rhGO-HP SSC calculated from the half-circle in the Nyquist plot is 0.6 Ω, much lower than the value of the rhGO-LP SSC (2.5 Ω). The lower R_{CT} relates to the faster charge transfer at the interface between the electrolyte ions and electrode materials. The higher density of nanoholes on the rhGO-HP sheet should be the reason for the faster charge transfer since they can offer more electrochemically active sites from the nanoholes.

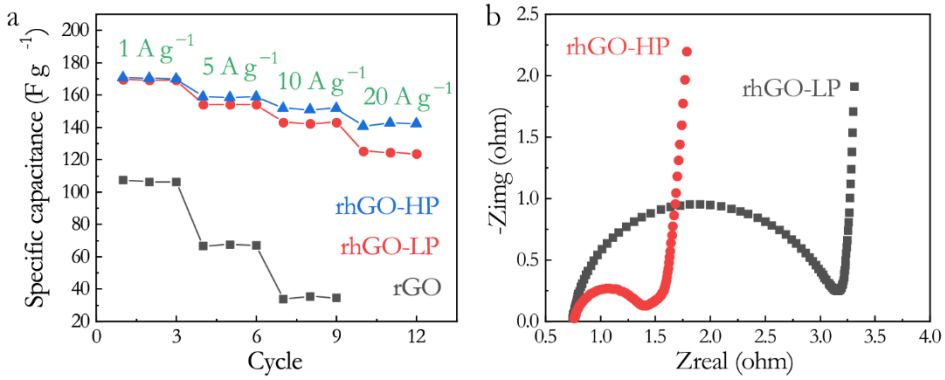

Figure 37. (a) Galvanostatic Charge and Discharge Results at Current Densities of 1, 5, 10, and 20 A g^{-1} for Symmetric Supercapacitors using Reduced Graphene Oxide (rGO), Holey rGO with Low (rhGO-LP) and High (rhGO-HP) Porosities as the Electrodes, Respectively. Specific Capacitance. (b) Nyquist Curves from Electrochemical Impedance Spectroscopy of rhGO-LP and rhGO-HP Symmetric Supercapacitors.

Table 12. Specific Capacitance of the Reduced Graphene Oxide (rGO) and Holey rGO (rhGO) Electrodes in Symmetric Supercapacitors Calculated from Galvanostatic Charge and Discharge Curves.

SSC	$C_{S,GCD}$ at 1 A g^{-1} [F g^{-1}]	$C_{S,GCD}$ at 5 A g^{-1} [F g^{-1}]	$C_{S,GCD}$ at 10 A g^{-1} [F g^{-1}]	$C_{S,GCD}$ at 20 A g^{-1} [F g^{-1}]
rGO	107	67	34	\
rhGO-LP	170	154	143	125
rhGO-HP	171	159	152	141

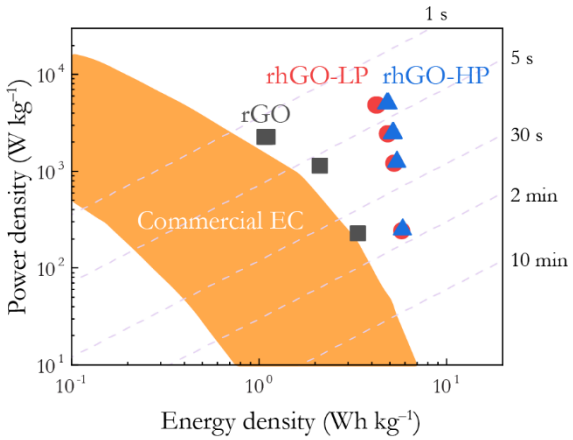

Figure 38. Ragone Plot Showing the Gravimetric Energy and Power Densities for the Symmetric Supercapacitors Using rGO (Black), rhGO-LP (Red), and rhGO-HP (Blue) as the Electrodes and the Commercial Electrochemical Capacitors (Yellow Region, Data are Extracted from Ref[135]. Dash Lines with Time Labels Indicates the Charge or Discharge Duration of Devices.

The Ragone plot in **Figure 38** shows the gravimetric energy and power densities of the rGO, rhGO-LP, and rhGO-HP SSCs and compares them with the commercial electrochemical capacitors (data from ref[135]). Similar to the trend of the GCD specific capacitance, the rhGO SSCs show prominent performance improvements compared with the rGO SSC. The highest energy density of the rhGO-HP SSC is 5.9 Wh kg^{-1} at a power density of 248 W kg^{-1}, and this device maintains an energy density of 4.9 Wh kg^{-1} at a high power density of 4,950 W kg^{-1}. The rhGO-LP SSC exhibits small differences in the energy density relative to the rhGO-HP SSC at low power densities, while the difference becomes more evident when the power density is above 10^3 W kg^{-1}. Compared with commercial

electrochemical capacitors, while the rGO SSC can compete with the best products, the rhGO SSCs present an obvious superiority in performance.

3 Holey Graphene for Electrocatalysis

3.1 Cyclic Voltammetry

To study the electrocatalytic activity of rhGO in redox reactions, the rhGO electrodes were measured in the aqueous electrolyte mixed by 5 mM $K_3[Fe(CN)_6]$ and 0.1 M KCl using the three-electrode cell. The same rhGO samples for capacitor electrode measurements were used here to prepare the working electrodes.

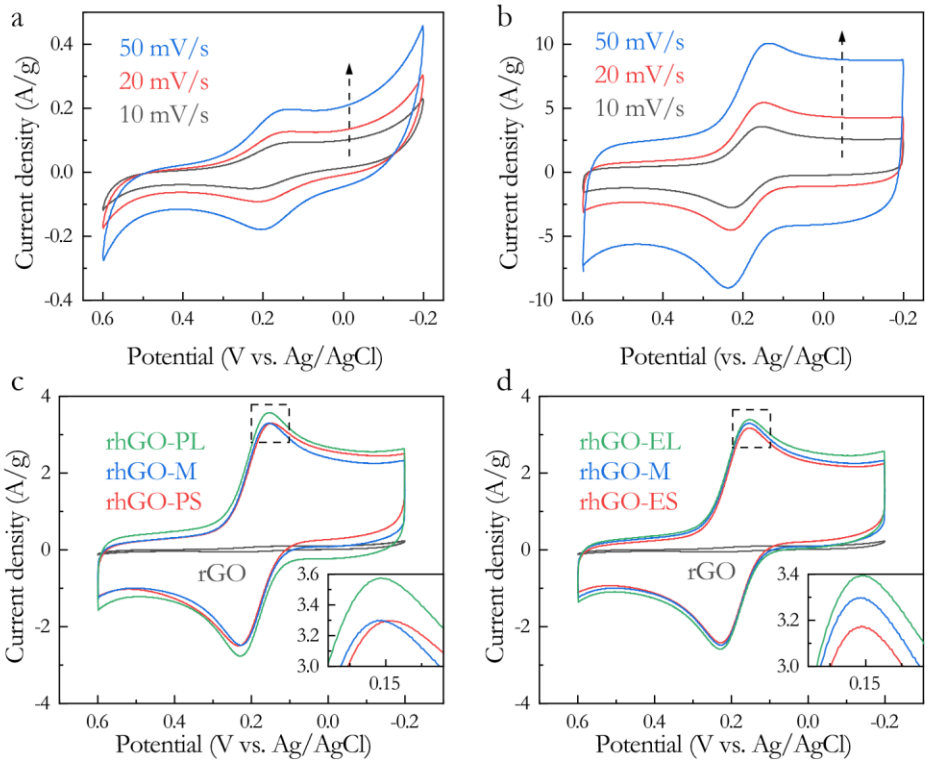

Figure 39. Cyclic Voltammetry Curves of (a) rGO and (b) rhGO-PL in the Aqueous Electrolyte Mixed by 5 mM $K_3[Fe(CN)_6]$ and 0.1 M KCl at Scan Rates of 10, 20, and 50 mV s^{-1}. Curves of rhGO with Different Durations of (c) Pretreatment and (d) MACE. Dash Lines in a,b Indicate the Direction of Scan Rate Increases. Insets in c,d Magnify the Redox Peaks Indicated by the Dash Squares.

Redox peaks near 0.2 V are observed in all the CV curves of rGO (**Figure 39**a) and rhGO (**Figure 39**b) at scan rates of 10–50 mV s^{-1}. During a negative scan of CV,

$[Fe(CN)_6]^{3-}$ ions are reduced to $[Fe(CN)_6]^{4-}$ ions by capturing electrons from the electrode, causing a cathodic current peak; during a positive scan, $[Fe(CN)_6]^{4-}$ ions are oxidized to $[Fe(CN)_6]^{3-}$ ions, generating an anodic current peak.[136] The rhGO electrodes exhibit remarkably higher catalytic activity compared to the rGO counterpart, as indicated by the 40 times higher redox peaks in the CV curves at a scan rate of 10 mV s^{-1}. It demonstrates the significant contribution of the in-plane nanoholes to electrocatalytic activity. Among the rhGO electrodes (**Figure 39**c,d), the redox peak grows with the area percentage of nanoholes, although the changes are not as obvious as the difference between rhGO and rGO.

The remarkable improvement of rhGO in the electrocatalytic activity compared with rGO should result from faster redox kinetics and diffusion kinetics. Firstly, more electrochemically active sites around the nanoholes contribute to faster redox kinetics by providing a larger electronic density of states of the electrode material.[137] It can be confirmed by the variation of peak-to-peak separation (ΔE_P) in the CV curves of different rhGO electrodes (**Table 13**). The rhGO electrodes with a higher area percentage of nanoholes tend to have smaller ΔE_P, meaning that a lower driving potential is required to trigger the redox reactions. Thus, the high area percentage of nanoholes is beneficial to the faster heterogeneous electron transfer. Secondly, the nanoholes on rhGO provide abundant

Table 13. Electrochemical Properties of Holey Graphene in 5 mM $K_3[Fe(CN)_6]$ and 0.1 M KCl.

Sample	ΔE_P [mV]	R_{CT} [Ω]	$D_{R\text{-}S}$ [$\times 10^{-6}$ cm^2 s^{-1}]	D_W [$\times 10^{-6}$ cm^2 s^{-1}]
rGO	91	125	2.12×10^{-3}	4.20×10^{-4}
rhGO-M	72	98	9.52	8.25
rhGO-PS	83	107	7.03	8.14
rhGO-PL	74	96	9.94	8.35
rhGO-ES	73	104	7.92	7.57
rhGO-EL	75	99	9.49	9.55

shortcuts for ion transportation, leading to faster diffusion kinetics. When ions participate in redox reactions, a diffusion layer gradually forms, where redox reactants are depleted, and further redox reactions are controlled by the ion diffusion rate.[136] In rhGO, ions transport via nanoholes and thus can deliver charges on the rhGO sheets located deeper from the electrode surface, causing a part of the diffusion layer overlapped by the depth of the rhGO electrode. Therefore, compared to the rGO counterpart, the diffusion layer above the surface of the rhGO electrode should be thinner, which facilitates ion diffusion. The ion diffusion coefficient can be given by the Randles-Sevcik equation,[115, 132, 133, 136]

$$i_p = 0.4463\, n^{\frac{3}{2}} F^{\frac{3}{2}} A c (v D_{\mathrm{R-S}}/RT)^{1/2} \quad (43)$$

where i_p is the peak current (A), n is the number of electron transfer (here is 1), c is the concentration of $[Fe(CN)_6]^{3-}$ ions (mol mL^{-1}), v is the scan rate (V s^{-1}), and $D_{\mathrm{R-S}}$ represents the diffusion coefficient (cm^2 s^{-1}) of $[Fe(CN)_6]^{3-}$ ions calculated from the Randles-Sevcik equation. By plotting i_P versus $v^{1/2}$ (i.e., the Randles-Sevcik plot), the ion diffusion coefficient can be obtained by fitting the slope of the curve and putting it to Equation 43. As shown in **Figure 40**a–c, good linear correlations between i_P and $v^{1/2}$ are observed in all samples. The calculation results (**Table 13**) based on Equation 43 show that the ion diffusion coefficients

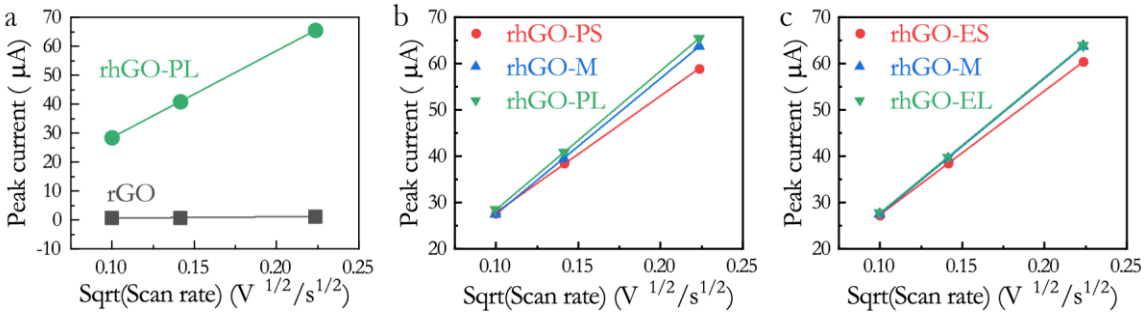

Figure 40. (a) Randles-Sevcik Plot of rGO and rhGO-PL Calculated from Cyclic Voltammetry Curves Measured at Scan Rates of 10–50 mV s^{-1} in 5 mM $K_3[Fe(CN)_6]$ and 0.1 M KCl. Randles-Sevcik Plots of rhGO with Different Durations of (b) Pretreatment and (c) MACE

in rhGO are at least three orders of magnitude higher than that in rGO (2.12×10^{-9} cm^2 s^{-1}). The rhGO-PL electrode has the highest ion diffusion coefficients of 9.94×10^{-6} cm^2 s^{-1}. The ion diffusion rate increases with the area percentage of nanoholes on rhGO, except for rhGO-EL that shows a slight drop compared with rhGO-M.

3.2 Electrochemical Impedance Spectroscopy

The Nyquist plot of the EIS results of rGO and rhGO-PL (**Figure 41**a) further demonstrates the distinct redox kinetics and diffusion kinetics, as different behaviors are observed in both the high- and low-frequency ranges. In the high-frequency range, the semicircle related to the charge transfer process is smaller in the rhGO curve, suggesting the lower R_{CT} in the rhGO electrode. The fitted values of R_{CT} (**Table 13**) of rhGO are all at least 20 Ω smaller than that in rGO, confirming the faster heterogeneous electron transfer of rhGO relative to rGO. In the low-frequency range, the rhGO electrode shows a smaller slope in the Warburg plot (**Figure 41**b) than the rGO counterpart, meaning the former has a lower Warburg coefficient and thus a higher ion diffusion coefficient. The fitting results (**Table 13**) using Equation 41 and 42 show that the ion diffusion coefficients in all the rhGO electrodes are four magnitudes higher than that in the rGO electrode.

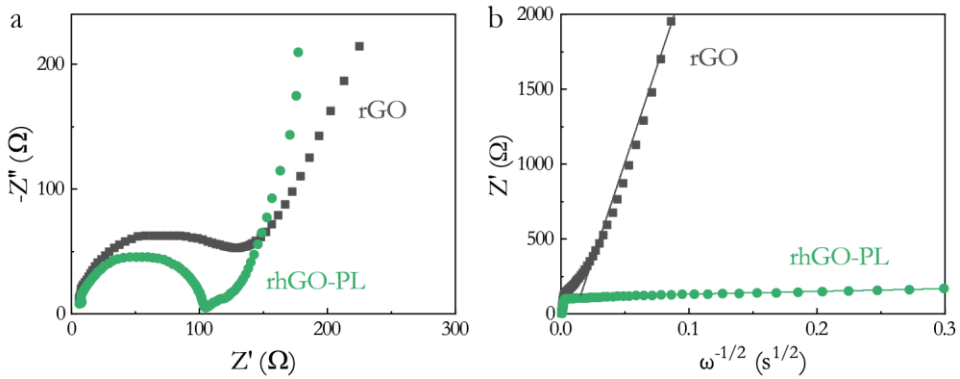

Figure 41. (a) Nyquist Plot and (b) Warburg Plot of the Electrode Impedance Spectroscopy Results of the rGO and rhGO-PL Electrodes Measured in 5 mM $K_3[Fe(CN)_6]$ and 0.1 M KCl.

Among the rhGO electrodes (**Figure 42**), the EIS results do not show significant changes with the processing parameters, while the subtle differences can still be measured. Indicated by the fitting results of R_{CT} (**Table 13**), the heterogeneous electron transfer becomes faster with a larger area percentage of nanoholes, and the only exception is rhGO-EL, which shows a slight increase in R_{CT}. This is consistent with the trend of the diffusion coefficients obtained using the Randles-Sevcik equation and CV data. The Warburg plot in **Figure 42**c,d suggests the similar behavior of the rhGO electrodes in the low-frequency region. Within a small variation range, rhGO-EL shows the highest ion diffusion coefficient of 9.55×10^{-6} cm^2 s^{-1}, while most of them have the ion diffusion coefficients of about 8×10^{-6} cm^2 s^{-1}. These results confirm again that a high area percentage of nanoholes is favorable to the electrocatalytic activity by providing more electrochemically active sites.

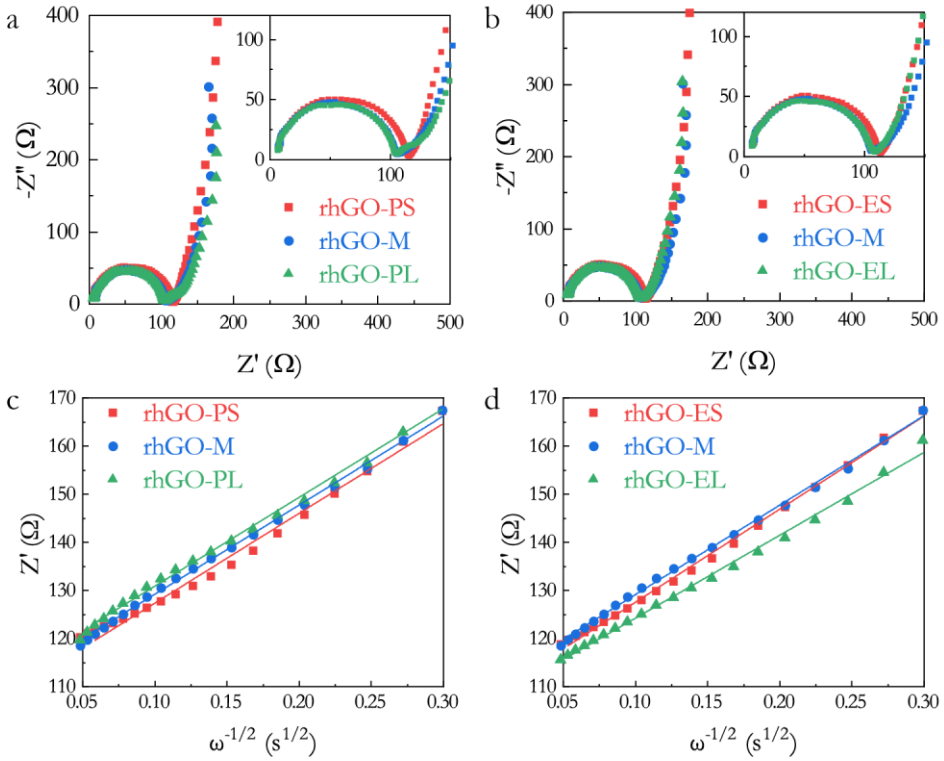

Figure 42. (a,b) Nyquist Plot and (c,d) Warburg Plot of the EIS Results of the rhGO Electrodes with Different Durations of (a,c) Pretreatment and (b,d) MACE Measured in 5 mM $K_3[Fe(CN)_6]$ and 0.1 M KCl.

4 Summary

Holey graphene manufactured via MACE exhibited notable improvements in electrochemical energy storage and electrocatalysis compared with the non-holey counterpart. As the electrode material in supercapacitors, both EDLC and pseudocapacitance exist in the energy storage process of rhGO, and the two mechanisms were enhanced by the faster ion diffusion and charge transfer in the rhGO electrode. By adjusting the manufacturing parameters, the capacitive performance of the rhGO electrode was optimized with a high nanohole population and a moderate area percentage, resulting in a high specific capacitance of 137 F g^{-1} at a current density of 0.5 A g^{-1}. Moreover, it maintained 69% of its initial specific capacitance when the current density increased to 100 A g^{-1}. After assembled into SSC devices, the rhGO electrode displayed a specific capacitance of 171 F g^{-1} at a current density of 1 A g^{-1}, remarkably higher than that measured in the rGO SSC (107 F g^{-1}). The higher nanohole density enhanced the rate performance of the SSC. The highest energy density of the rhGO SSC was 5.9 Wh kg^{-1} at a power density of 248 W kg^{-1}, and this device maintained an energy density of 4.9 Wh kg^{-1} at a high power density of 4,950 W kg^{-1}, demonstrating the high potential of holey graphene manufactured via MACE in the fast energy storage devices. The rhGO electrode also exhibited high electrocatalytic activity in the redox reactions. The in-plane nanoholes on graphene brought more electrochemically active sites to improve the charge transfer process at the electrolyte–electrode interface, and it also facilitated the ion diffusion kinetics by offering more mass transport channels. The peak current of the rhGO electrode in CV measurements was 40 times that of the non-holey counterpart, and the ion diffusion coefficient of the former could be 3–4 magnitudes higher than that of the latter.

CHAPTER 6

CONCLUSION

The fabrication of holey graphene with excellent capacitive performance and electrochemical catalytic activity was achieved within a few minutes via the MACE method, which was much faster than the conventional hour-scale approaches. Moreover, a two-step strategy combining pretreatment and MACE effectively controlled the population, average diameter, area percentage of nanoholes on holey graphene sheets, assisting the further promotion of the electrochemical properties. This microwave-assisted method was fast, controllable, fully solution-based, and thus favorable to be employed in large-scale manufacturing for various applications.

The structural characterizations provided insights into the formation and growth of nanoholes during each step of fabrication. The pretreatment caused a partial reduction of GO sheets with an increased defect density. DFT and MD simulations confirmed that the vacancy defects could grow into nanoholes in the MACE process due to the coupling effect of microwave irradiation and hydrogen peroxide oxidation.

The mechanism of the rapid fabrication process was also elucidated. During the MACE, the microwave-induced selective heating of GO sheets, by both local Joule heating and dielectric heating, facilitated the effective etching of GO sheets and limited the decomposition of hydrogen peroxide during processing.

In electrochemical measurements, the nanoholes on holey graphene significantly improved the accessible surface area of the electrode, heterogeneous electron transfer, and ion diffusion kinetics, demonstrating the excellent application potential of the microwave-fabricated holey graphene in both electrochemical energy storage and electrocatalysis.

REFERENCES

1. Bonaccorso F, Colombo L, Yu G, Stoller M, Tozzini V, Ferrari AC*, et al.* Graphene, related two-dimensional crystals, and hybrid systems for energy conversion and storage. *Science* 2015, **347**(6217)**:** 1246501.

2. Novoselov KS, Mishchenko A, Carvalho A, Castro Neto AH. 2D materials and van der Waals heterostructures. *Science* 2016, **353**(6298)**:** aac9439.

3. Raccichini R, Varzi A, Passerini S, Scrosati B. The role of graphene for electrochemical energy storage. *Nature Materials* 2015, **14**(3)**:** 271.

4. Zhu H, Gan X, McCreary A, Lv R, Lin Z, Terrones M. Heteroatom doping of two-dimensional materials: From graphene to chalcogenides. *Nano Today* 2020, **30:** 100829.

5. Georgakilas V. *Functionalization of Graphene*. John Wiley & Sons, Incorporated: Somerset, GERMANY, 2014.

6. Cao Y, Fatemi V, Fang S, Watanabe K, Taniguchi T, Kaxiras E*, et al.* Unconventional superconductivity in magic-angle graphene superlattices. *Nature* 2018, **556**(7699)**:** 43-50.

7. Rhodes D, Chae SH, Ribeiro-Palau R, Hone J. Disorder in van der Waals heterostructures of 2D materials. *Nature Materials* 2019, **18**(6)**:** 541-549.

8. Yang J, Ma M, Li L, Zhang Y, Huang W, Dong X. Graphene nanomesh: new versatile materials. *Nanoscale* 2014, **6**(22)**:** 13301-13313.

9. Chen Z, An X, Dai L, Xu Y. Holey graphene-based nanocomposites for efficient electrochemical energy storage. *Nano Energy* 2020**:** 104762.

10. Lokhande AC, Qattan IA, Lokhande CD, Patole SP. Holey graphene: an emerging versatile material. *Journal of Materials Chemistry A* 2020, **8**(3)**:** 918-977.

11. Nazarian-Samani M, Haghighat-Shishavan S, Nazarian-Samani M, Kashani-Bozorg SF, Ramakrishna S, Kim K-B. Perforated two-dimensional nanoarchitectures for next-generation batteries: Recent advances and extensible perspectives. *Progress in Materials Science* 2020**:** 100716.

12. Novoselov KS, Fal'ko VI, Colombo L, Gellert PR, Schwab MG, Kim K. A roadmap for graphene. *Nature* 2012, **490**(7419)**:** 192-200.

13. Wang H, Maiyalagan T, Wang X. Review on Recent Progress in Nitrogen-Doped Graphene: Synthesis, Characterization, and Its Potential Applications. *ACS Catalysis* 2012, **2**(5)**:** 781-794.

14. Li F, Jiang X, Zhao J, Zhang S. Graphene oxide: A promising nanomaterial for energy and environmental applications. *Nano Energy* 2015, **16:** 488-515.

15. Wang T, Huang D, Yang Z, Xu S, He G, Li X*, et al.* A Review on Graphene-Based Gas/Vapor Sensors with Unique Properties and Potential Applications. *Nanomicro Lett* 2016, **8**(2)**:** 95-119.

16. Higgins D, Zamani P, Yu A, Chen Z. The application of graphene and its composites in oxygen reduction electrocatalysis: a perspective and review of recent progress. *Energy & Environmental Science* 2016, **9**(2)**:** 357-390.

17. Kong W, Kum H, Bae SH, Shim J, Kim H, Kong L*, et al.* Path towards graphene commercialization from lab to market. *Nat Nanotechnol* 2019, **14**(10)**:** 927-938.

18. Bai J, Zhong X, Jiang S, Huang Y, Duan X. Graphene nanomesh. *Nature Nanotechnology* 2010, **5**(3)**:** 190-194.

19. Zhao X, Hayner CM, Kung MC, Kung HH. Flexible Holey Graphene Paper Electrodes with Enhanced Rate Capability for Energy Storage Applications. *ACS Nano* 2011, **5**(11)**:** 8739-8749.

20. Poonam, Sharma K, Arora A, Tripathi SK. Review of supercapacitors: Materials and devices. *Journal of Energy Storage* 2019, **21:** 801-825.

21. Yang C-H, Huang P-L, Luo X-F, Wang C-H, Li C, Wu Y-H*, et al.* Holey Graphene Nanosheets with Surface Functional Groups as High-Performance Supercapacitors in Ionic-Liquid Electrolyte. *ChemSusChem* 2015, **8**(10)**:** 1779-1786.

22. Sammed KA, Pan L, Asif M, Usman M, Cong T, Amjad F*, et al.* Reduced holey graphene oxide film and carbon nanotubes sandwich structure as a binder-free electrode material for supercapcitor. *Sci Rep* 2020, **10**(1)**:** 2315.

23. Xu Y, Lin Z, Zhong X, Huang X, Weiss NO, Huang Y*, et al.* Holey graphene frameworks for highly efficient capacitive energy storage. *Nat Commun* 2014, **5:** 4554.

24. Pan Z, Zhi H, Qiu Y, Yang J, Xing L, Zhang Q*, et al.* Achieving commercial-level mass loading in ternary-doped holey graphene hydrogel electrodes for ultrahigh energy density supercapacitors. *Nano Energy* 2018, **46:** 266-276.

25. Du P, Dong Y, Kang H, Wang Q, Niu J. Synthesis of holey graphene networks functionalized with p-phenylene diamine monomers for superior performance flexible solid-state supercapacitors. *Electrochimica Acta* 2019, **320:** 134610.

26. Liu J, Du P, Wang Q, Liu D, Liu P. Mild synthesis of holey N-doped reduced graphene oxide and its double-edged effects in polyaniline hybrids for supercapacitor application. *Electrochimica Acta* 2019, **305:** 175-186.

27. Zhai S, Wang C, Karahan HE, Wang Y, Chen X, Sui X*, et al.* Nano-RuO2-Decorated Holey Graphene Composite Fibers for Micro-Supercapacitors with Ultrahigh Energy Density. *Small* 2018, **14**(29)**:** 1800582.

28. Chen x, Han J, Lv X, Lv W, Pan Z-Z, Luo C*, et al.* Dense yet highly ion permeable graphene electrodes by capillary-drying of holey graphene oxide assembly. *Journal of Materials Chemistry A* 2019.

29. Kotal M, Kim H, Roy S, Oh I. Sulfur and Nitrogen Co-Doped Holey Graphene Aerogel for Structurally Resilient Solid-State Supercapacitors under High-Compressions. *Journal of Materials Chemistry A* 2017, **5**(33)**:** 17253-17266.

30. Ye X, Zhu Y, Jiang H, Yue Z, Wang L, Wan Z*, et al.* Constructing molecules supported holey graphene sheets framework in compact graphene film to achieve synergistic effect for ion transport and high gravimetric/volumetric capacitances. *Journal of Power Sources* 2019, **441:** 227167.

31. Fan Z, Cheng Z, Feng J, Xie Z, Liu Y, Wang Y. Ultrahigh volumetric performance of a free-standing compact N-doped holey graphene/PANI slice for supercapacitors. *Journal of Materials Chemistry A* 2017, **5**(32)**:** 16689-16701.

32. Fan Z, Wang Y, Xie Z, Wang D, Yuan Y, Kang H*, et al.* Modified MXene/Holey Graphene Films for Advanced Supercapacitor Electrodes with Superior Energy Storage. *Advanced Science* 2018**:** 1800750.

33. Stoller MD, Ruoff RS. Best practice methods for determining an electrode material's performance for ultracapacitors. *Energy & Environmental Science* 2010, **3**(9)**:** 1294-1301.

34. Xu Y, Chen C-Y, Zhao Z, Lin Z, Lee C, Xu X*, et al.* Solution Processable Holey Graphene Oxide and Its Derived Macrostructures for High-Performance Supercapacitors. *Nano Letters* 2015, **15**(7)**:** 4605-4610.

35. Fan Z, Yan J, Wei T, Zhi L, Ning G, Li T*, et al.* Asymmetric Supercapacitors Based on Graphene/MnO2 and Activated Carbon Nanofiber Electrodes with High Power and Energy Density. *Advanced Functional Materials* 2011, **21**(12)**:** 2366-2375.

36. Lu A-K, Li H-Y, Yu Y. Holey graphene synthesized by electrochemical exfoliation for high-performance flexible microsupercapacitors. *Journal of Materials Chemistry A* 2019.

37. Lokhande AC, Teotia S, Qattan IA, Anjum D, Liao K, Patole SP. Green chemistry based fabrication of holey graphene electrodes for high-performance supercapacitors. *Materials Letters* 2020, **271:** 127793.

38. Wang C, Zhai S, Yuan Z, Chen J, Zhang X, Huang Q*, et al.* A core-sheath holey graphene/graphite composite fiber intercalated with MoS2 nanosheets for high-performance fiber supercapacitors. *Electrochimica Acta* 2019, **305:** 493-501.

39. Jeong JH, Lee G-W, Kim YH, Choi YJ, Roh KC, Kim K-B. A holey graphene-based hybrid supercapacitor. *Chem Eng J* 2019, **378:** 122126.

40. Bai Y, Yang X, He Y, Zhang J, Kang L, Xu H*, et al.* Formation process of holey graphene and its assembled binder-free film electrode with high volumetric capacitance. *Electrochimica Acta* 2016, **187:** 543-551.

41. Jiang Z-j, Jiang Z, Chen W. The role of holes in improving the performance of nitrogen-doped holey graphene as an active electrode material for supercapacitor and oxygen reduction reaction. *Journal of Power Sources* 2014, **251:** 55-65.

42. Walsh ED, Han X, Lacey SD, Kim J-W, Connell JW, Hu L*, et al.* Dry-Processed, Binder-Free Holey Graphene Electrodes for Supercapacitors with Ultrahigh Areal Loadings. *ACS Applied Materials & Interfaces* 2016, **8**(43)**:** 29478-29485.

43. Sun H, Mei L, Liang J, Zhao Z, Lee C, Fei H*, et al.* Three-dimensional holey-graphene/niobia composite architectures for ultrahigh-rate energy storage. *Science* 2017, **356**(6338)**:** 599-604.

44. Xiang Y, Zhang W, Chen B, Jin Z, Zhang H, Zhao P*, et al.* Nano-Li4Ti5O12 particles in-situ deposited on compact holey-graphene framework for high volumetric power capability of lithium ion battery anode. *Journal of Power Sources* 2020, **447:** 227372.

45. Xu P, Gao Q, Ma L, Li Z, Zhang H, Xiao H*, et al.* A high surface area N-doped holey graphene aerogel with low charge transfer resistance as high performance electrode of non-flammable thermostable supercapacitor. *Carbon* 2019.

46. Wu D, Wang C, Wu H, Wang S, Wang F, Chen Z*, et al.* Synthesis of hollow Co3O4 nanocrystals in situ anchored on holey graphene for high rate lithium-ion batteries. *Carbon* 2020, **163:** 137-144.

47. Zhao J, Zhang Y-Z, Zhang F, Liang H, Ming F, Alshareef HN*, et al.* Partially Reduced Holey Graphene Oxide as High Performance Anode for Sodium-Ion Batteries. *Advanced Energy Materials* 2019, **9**(7)**:** 1803215.

48. Kirsch DJ, Lacey SD, Kuang Y, Pastel G, Xie H, Connell JW*, et al.* Scalable Dry Processing of Binder-Free Lithium-Ion Battery Electrodes Enabled by Holey Graphene. *ACS Applied Energy Materials* 2019, **2**(5)**:** 2990-2997.

49. Han X, Yang Z, Zhao B, Zhu S, Zhou L, Dai J*, et al.* Compressible, Dense, Three-Dimensional Holey Graphene Monolithic Architecture. *ACS Nano* 2017, **11**(3)**:** 3189-3197.

50. Huang Y-R, Chen C-L, Pu N-W, Wu C-H, Liu Y-M, Chen Y-H*, et al.* Experimental and Modeling Analysis of Holey Graphene Electrodes for High-Power-Density Li-Ion Batteries. *Crystals* 2020, **10**(11)**:** 1063.

51. Yu D, Wei L, Jiang W, Wang H, Sun B, Zhang Q*, et al.* Nitrogen doped holey graphene as an efficient metal-free multifunctional electrochemical catalyst for hydrazine oxidation and oxygen reduction. *Nanoscale* 2013, **5**(8)**:** 3457-3464.

52. Bian Y, Wang H, Hu J, Liu B, Liu D, Dai L. Nitrogen-rich holey graphene for efficient oxygen reduction reaction. *Carbon* 2020, **162:** 66-73.

53. Du P, Hu K, Lyu J, Li H, Lin X, Xie G*, et al.* Anchoring Mo single atoms/clusters and N on edge-rich nanoporous holey graphene as bifunctional air electrode in Zn−air batteries. *Applied Catalysis B: Environmental* 2020, **276:** 119172.

54. Kong W, Yao K, Duan X, Liu Z, Hu J. Holey Co, N-codoped graphene aerogel with in-plane pores and multiple active sites for efficient oxygen reduction. *Electrochimica Acta* 2018, **269:** 544-552.

55. Shu X, Chen S, Chen S, Pan W, Zhang J. Cobalt nitride embedded holey N-doped graphene as advanced bifunctional electrocatalysts for Zn-Air batteries and overall water splitting. *Carbon* 2020, **157:** 234-243.

56. Wu P, Wu J, Si H, Zhang Z, Liao Q, Wang X*, et al.* 3D Holey-Graphene Architecture Expedites Ion Transport Kinetics to Push the OER Performance. *Advanced Energy Materials* 2020, **10**(22)**:** 2001005.

57. Qie L, Lin Y, Connell JW, Xu J, Dai L. Highly Rechargeable Lithium-CO2 Batteries with a Boron- and Nitrogen-Codoped Holey-Graphene Cathode. *Angewandte Chemie International Edition* 2017, **56**(24)**:** 6970-6974.

58. Hu C, Gong L, Xiao Y, Yuan Y, Bedford NM, Xia Z*, et al.* High-Performance, Long-Life, Rechargeable Li–CO2 Batteries based on a 3D Holey Graphene Cathode Implanted with Single Iron Atoms. *Advanced Materials* 2020, **32**(16)**:** 1907436.

59. Ito Y, Ohto T, Hojo D, Wakisaka M, Nagata Y, Chen L*, et al.* Cooperation between holey graphene and NiMo alloy for hydrogen evolution in an acidic electrolyte. *ACS Catalysis* 2018, **8**(4)**:** 3579-3586.

60. Kumatani A, Miura C, Kuramochi H, Ohto T, Wakisaka M, Nagata Y*, et al.* Chemical Dopants on Edge of Holey Graphene Accelerate Electrochemical Hydrogen Evolution Reaction. *Advanced Science* 2019, **6**(10)**:** 1900119.

61. Savaram K, Li M, Tajima K, Takai K, Hayashi T, Hall G*, et al.* Dry microwave heating enables scalable fabrication of pristine holey graphene nanoplatelets and their catalysis in reductive hydrogen atom transfer reactions. *Carbon* 2018, **139:** 861-871.

62. Li G, Dong D, Hong G, Yan L, Zhang X, Song W. High-Efficiency Cryo-Thermocells Assembled with Anisotropic Holey Graphene Aerogel Electrodes and a Eutectic Redox Electrolyte. *Advanced Materials* 2019.

63. Kong W, Duan X, Ge Y, Liu H, Hu J, Duan X. Holey graphene hydrogel with in-plane pores for high-performance capacitive desalination. *Nano Research* 2016, **9**(8)**:** 2458-2466.

64. Mi M, Liu X, Kong W, Ge Y, Dang W, Hu J. Hierarchical composite of N-doped carbon sphere and holey graphene hydrogel for high-performance capacitive deionization. *Desalination* 2019, **464:** 18-24.

65. Yang Y, Yang X, Liang L, Gao Y, Cheng H, Li X*, et al.* Large-area graphene-nanomesh/carbon-nanotube hybrid membranes for ionic and molecular nanofiltration. *Science* 2019, **364**(6445)**:** 1057-1062.

66. Jiang J, Cui D, Yan T, Guo F, Gu W. Holey graphene layers as promising drug delivery systems. *Physica E: Low-dimensional Systems and Nanostructures* 2020, **124:** 114303.

67. Liu J, Cai H, Yu X, Zhang K, Li X, Li J*, et al.* Fabrication of Graphene Nanomesh and Improved Chemical Enhancement for Raman Spectroscopy. *The Journal of Physical Chemistry C* 2012, **116**(29)**:** 15741-15746.

68. Liang X, Jung YS, Wu S, Ismach A, Olynick DL, Cabrini S*, et al.* Formation of bandgap and subbands in graphene nanomeshes with sub-10 nm ribbon width fabricated via nanoimprint lithography. *Nano Lett* 2010, **10**(7)**:** 2454-2460.

69. Zeng Z, Huang X, Yin Z, Li H, Chen Y, Li H*, et al.* Fabrication of Graphene Nanomesh by Using an Anodic Aluminum Oxide Membrane as a Template. *Advanced Materials* 2012, **24**(30)**:** 4138-4142.

70. Yang D-P, Wang X, Guo X, Zhi X, Wang K, Li C*, et al.* UV/O3 Generated Graphene Nanomesh: Formation Mechanism, Properties, and FET Studies. *The Journal of Physical Chemistry C* 2013, **118**(1)**:** 725-731.

71. Akhavan O. Graphene Nanomesh by ZnO Nanorod Photocatalysts. *ACS Nano* 2010, **4**(7)**:** 4174-4180.

72. Singh D, Shukla V, Ahuja R. Optical excitations and thermoelectric properties of 2D holey graphene. *arXiv.org*. May 19, 2020 ed; 2020.

73. Wang X, Jiao L, Sheng K, Li C, Dai L, Shi G. Solution-processable graphene nanomeshes with controlled pore structures. *Scientific reports* 2013, **3:** 1996.

74. Patel M, Feng W, Savaram K, Khoshi MR, Huang R, Sun J*, et al.* Microwave Enabled One-Pot, One-Step Fabrication and Nitrogen Doping of Holey Graphene Oxide for Catalytic Applications. *Small* 2015, **11**(27)**:** 3358-3368.

75. Hummers Jr WS, Offeman RE. Preparation of graphitic oxide. *Journal of the American Chemical Society* 1958, **80**(6)**:** 1339-1339.

76. Radich JG, Kamat PV. Making Graphene Holey. Gold-Nanoparticle-Mediated Hydroxyl Radical Attack on Reduced Graphene Oxide. *ACS Nano* 2013, **7**(6)**:** 5546-5557.

77. Han X, Funk MR, Shen F, Chen Y-C, Li Y, Campbell CJ*, et al.* Scalable Holey Graphene Synthesis and Dense Electrode Fabrication toward High-Performance Ultracapacitors. *ACS Nano* 2014, **8**(8)**:** 8255-8265.

78. Lin Y, Han X, Campbell CJ, Kim J-W, Zhao B, Luo W*, et al.* Holey Graphene Nanomanufacturing: Structure, Composition, and Electrochemical Properties. *Advanced Functional Materials* 2015, **25**(19)**:** 2920-2927.

79. Zang P, Gao S, Dang L, Liu Z, Lei Z. Green synthesis of holey graphene sheets and their assembly into aerogel with improved ion transport property. *Electrochimica Acta* 2016, **212:** 171-178.

80. Zhao Y, Hu C, Song L, Wang L, Shi G, Dai L*, et al.* Functional graphene nanomesh foam. *Energy & Environmental Science* 2014, **7**(6)**:** 1913-1918.

81. Kim H-K, Bak S-M, Lee SW, Kim M-S, Park B, Lee SC*, et al.* Scalable fabrication of micron-scale graphene nanomeshes for high-performance supercapacitor applications. *Energy & Environmental Science* 2016, **9**(4)**:** 1270-1281.

82. Lv R, Wang H, Yu H, Peng F. Controllable Preparation of Holey Graphene and Electrocatalytic Performance for Oxygen Reduction Reaction. *Electrochimica Acta* 2017, **228:** 203-213.

83. Wang Y, Adekoya D, Sun J, Tang T, Qiu H, Xu L*, et al.* Manipulation of Edge-Site Fe–N2 Moiety on Holey Fe, N Codoped Graphene to Promote the Cycle Stability and Rate Capacity of Li–S Batteries. *Advanced Functional Materials* 2018, **0**(0)**:** 1807485.

84. Zhang L, Yue J, Wei T, Liu Z, Zhou J, Liu C*, et al.* Densely pillared holey-graphene block with high-level nitrogen doping enabling ultra-high volumetric capacity for lithium ion storage. *Carbon* 2019, **142:** 327-336.

85. Wang J, Park T, Yi JW, Ding B, Henzie J, Chang Z*, et al.* Scalable synthesis of holey graphite nanosheets for supercapacitors with high volumetric capacitance. *Nanoscale Horizons* 2019, **4**(2)**:** 526-530.

86. Lin Y, Watson KA, Kim J-W, Baggett DW, Working DC, Connell JW. Bulk preparation of holey graphene via controlled catalytic oxidation. *Nanoscale* 2013, **5**(17)**:** 7814-7824.

87. Guo C, Zhang Y, Zeng T, Huang D, Wan Q, Yang N. High-performance asymmetric supercapacitors using holey graphene electrodes and redox electrolytes. *Carbon* 2020, **157:** 298-307.

88. Alsharaeh E, Ahmed F, Aldawsari Y, Khasawneh M, Abuhimd H, Alshahrani M. Novel synthesis of holey reduced graphene oxide (HRGO) by microwave irradiation method for anode in lithium-ion batteries. *Scientific Reports* 2016, **6:** 29854.

89. Datta SS, Strachan DR, Khamis SM, Johnson ATC. Crystallographic Etching of Few-Layer Graphene. *Nano Letters* 2008, **8**(7)**:** 1912-1915.

90. Campos LC, Manfrinato VR, Sanchez-Yamagishi JD, Kong J, Jarillo-Herrero P. Anisotropic Etching and Nanoribbon Formation in Single-Layer Graphene. *Nano Letters* 2009, **9**(7)**:** 2600-2604.

91. Zhang Y, Li Z, Kim P, Zhang L, Zhou C. Anisotropic Hydrogen Etching of Chemical Vapor Deposited Graphene. *ACS Nano* 2012, **6**(1)**:** 126-132.

92. Peng Y-Y, Liu Y-M, Chang J-K, Wu C-H, Ger M-D, Pu N-W*, et al.* A facile approach to produce holey graphene and its application in supercapacitors. *Carbon* 2015, **81:** 347-356.

93. Schneider GF, Kowalczyk SW, Calado VE, Pandraud G, Zandbergen HW, Vandersypen LM*, et al.* DNA translocation through graphene nanopores. *Nano Lett* 2010, **10**(8)**:** 3163-3167.

94. Mahmood J, Lee EK, Jung M, Shin D, Jeon IY, Jung SM*, et al.* Nitrogenated holey two-dimensional structures. *Nat Commun* 2015, **6:** 6486.

95. Menéndez JA, Arenillas A, Fidalgo B, Fernández Y, Zubizarreta L, Calvo EG*, et al.* Microwave heating processes involving carbon materials. *Fuel Processing Technology* 2010, **91**(1)**:** 1-8.

96. Wang C, Han X, Xu P, Zhang X, Du Y, Hu S*, et al.* The electromagnetic property of chemically reduced graphene oxide and its application as microwave absorbing material. *Applied Physics Letters* 2011, **98**(7)**:** 072906.

97. National Research Council, Division on Engineering and Physical Sciences, National Materials Advisory Board, Commission on Engineering and Technical Systems, Technology aCoMPoMAEI. *Microwave Processing of Materials*. National Academies Press: Washington, D.C., UNITED STATES, 1994.

98. Kuang B, Song W, Ning M, Li J, Zhao Z, Guo D*, et al.* Chemical reduction dependent dielectric properties and dielectric loss mechanism of reduced graphene oxide. *Carbon* 2018, **127:** 209-217.

99. Qin F, Brosseau C. Comment on "The electromagnetic property of chemically reduced graphene oxide and its application as microwave absorbing material" [Appl. Phys. Lett. 98, 072906 (2011)]. *Applied Physics Letters* 2012, **100**(4)**:** 046101.

100. Rybakov KI, Semenov VE, Egorov SV, Eremeev AG, Plotnikov IV, Bykov YV. Microwave heating of conductive powder materials. *Journal of Applied Physics* 2006, **99**(2)**:** 023506.

101. Khattak HK, Bianucci P, Slepkov AD. Linking plasma formation in grapes to microwave resonances of aqueous dimers. *Proceedings of the National Academy of Sciences* 2019, **116**(10)**:** 4000-4005.

102. Meng F, Wang H, Huang F, Guo Y, Wang Z, Hui D*, et al.* Graphene-based microwave absorbing composites: A review and prospective. *Composites Part B: Engineering* 2018, **137:** 260-277.

103. Zhu Y, Murali S, Stoller MD, Velamakanni A, Piner RD, Ruoff RS. Microwave assisted exfoliation and reduction of graphite oxide for ultracapacitors. *Carbon* 2010, **48**(7)**:** 2118-2122.

104. Hu H, Zhao Z, Zhou Q, Gogotsi Y, Qiu J. The role of microwave absorption on formation of graphene from graphite oxide. *Carbon* 2012, **50**(9)**:** 3267-3273.

105. Voiry D, Yang J, Kupferberg J, Fullon R, Lee C, Jeong HY*, et al.* High-quality graphene via microwave reduction of solution-exfoliated graphene oxide. *Science* 2016, **353**(6306)**:** 1413-1416.

106. Jiang W-S, Yang C, Chen G-X, Yan X-Q, Chen S-N, Su B-W*, et al.* Preparation of high-quality graphene using triggered microwave reduction under an air atmosphere. *Journal of Materials Chemistry C* 2018, **6**(7)**:** 1829-1835.

107. Kang S, Choi H, Lee SB, Park SC, Park JB, Lee S*, et al.* Efficient heat generation in large-area graphene films by electromagnetic wave absorption. *2D Materials* 2017, **4**(2)**:** 025037.

108. Marcano DC, Kosynkin DV, Berlin JM, Sinitskii A, Sun Z, Slesarev A*, et al.* Improved Synthesis of Graphene Oxide. *ACS Nano* 2010, **4**(8)**:** 4806-4814.

109. Kresse G, Furthmüller J. Efficiency of ab-initio total energy calculations for metals and semiconductors using a plane-wave basis set. *Computational Materials Science* 1996, **6**(1)**:** 15-50.

110. Perdew JP, Burke K, Ernzerhof M. Generalized Gradient Approximation Made Simple. *Physical Review Letters* 1996, **77**(18)**:** 3865-3868.

111. Kresse G, Joubert D. From ultrasoft pseudopotentials to the projector augmented-wave method. *Physical Review B* 1999, **59**(3)**:** 1758-1775.

112. Blöchl PE. Projector augmented-wave method. *Physical Review B* 1994, **50**(24)**:** 17953-17979.

113. Bagri A, Mattevi C, Acik M, Chabal YJ, Chhowalla M, Shenoy VB. Structural evolution during the reduction of chemically derived graphene oxide. *Nature Chemistry* 2010, **2:** 581.

114. Banerjee S, Shim J, Rivera J, Jin X, Estrada D, Solovyeva V*, et al.* Electrochemistry at the Edge of a Single Graphene Layer in a Nanopore. *ACS Nano* 2013, **7**(1)**:** 834-843.

115. Yuan W, Zhou Y, Li Y, Li C, Peng H, Zhang J*, et al.* The edge- and basal-plane-specific electrochemistry of a single-layer graphene sheet. *Scientific Reports* 2013, **3:** 2248.

116. Chen WF, Yan LF, Bangal PR. Preparation of graphene by the rapid and mild thermal reduction of graphene oxide induced by microwaves. *Carbon* 2010, **48**(4)**:** 1146-1152.

117. Zhu Y, Stoller MD, Cai W, Velamakanni A, Piner RD, Chen D*, et al.* Exfoliation of Graphite Oxide in Propylene Carbonate and Thermal Reduction of the Resulting Graphene Oxide Platelets. *ACS Nano* 2010, **4**(2)**:** 1227-1233.

118. Zhu C, Hui Z, Pan H, Zhu S, Zhang Q, Mao J*, et al.* Ultrafast Li-ion migration in holey-graphene-based composites constructed by a generalized ex situ method towards high capacity energy storage. *Journal of Materials Chemistry A* 2019, **7**(9)**:** 4788-4796.

119. Kudin KN, Ozbas B, Schniepp HC, Prud'homme RK, Aksay IA, Car R. Raman Spectra of Graphite Oxide and Functionalized Graphene Sheets. *Nano Letters* 2008, **8**(1)**:** 36-41.

120. Ferrari AC, Basko DM. Raman spectroscopy as a versatile tool for studying the properties of graphene. *Nat Nano* 2013, **8**(4)**:** 235-246.

121. Dresselhaus MS, Jorio A, Hofmann M, Dresselhaus G, Saito R. Perspectives on Carbon Nanotubes and Graphene Raman Spectroscopy. *Nano Letters* 2010, **10**(3)**:** 751-758.

122. Cançado LG, Jorio A, Ferreira EHM, Stavale F, Achete CA, Capaz RB*, et al.* Quantifying Defects in Graphene via Raman Spectroscopy at Different Excitation Energies. *Nano Letters* 2011, **11**(8)**:** 3190-3196.

123. Dreyer DR, Park S, Bielawski CW, Ruoff RS. The chemistry of graphene oxide. *Chemical Society Reviews* 2010, **39**(1)**:** 228-240.

124. Cai W, Piner RD, Stadermann FJ, Park S, Shaibat MA, Ishii Y*, et al.* Synthesis and Solid-State NMR Structural Characterization of ^{13}C-Labeled Graphite Oxide. 2008, **321**(5897)**:** 1815-1817.

125. Tanaka M, Sato M. Microwave heating of water, ice, and saline solution: Molecular dynamics study. *The Journal of Chemical Physics* 2007, **126**(3)**:** 034509.

126. Huang X, Zhi C, Jiang P, Golberg D, Bando Y, Tanaka T. Temperature-dependent electrical property transition of graphene oxide paper. *Nanotechnology* 2012, **23**(45)**:** 455705.

127. Chase MW, Jr. CAD, J.R. Downey J, Frurip DJ, McDonald RA, Syverud AN. *NIST-JANAF Thermochemical Tables*. National Institute of Standards and Technology: Gaithersburg, MD 20899, 1998.

128. Pop E, Varshney V, Roy AK. Thermal properties of graphene: Fundamentals and applications. *MRS Bulletin* 2012, **37**(12)**:** 1273-1281.

129. Ma F, Zheng HB, Sun YJ, Yang D, Xu KW, Chu PK. Strain effect on lattice vibration, heat capacity, and thermal conductivity of graphene. *Applied Physics Letters* 2012, **101**(11)**:** 111904.

130. Jin S, Gao Q, Zeng X, Zhang R, Liu K, Shao X*, et al.* Effects of reduction methods on the structure and thermal conductivity of free-standing reduced graphene oxide films. *Diamond and Related Materials* 2015, **58:** 54-61.

131. Hippel ARv. *Dielectric Materials and Applications*. MIT Press: Cambridge, MA, 1954.

132. Bard AJ, Faulner LR. *Electrochemical methods: fundamentals and applications*, 2rd edn. Wiley: New York, 2001.

133. Zanello P. *Inorganic Electrochemistry: Theory, Practice and Application*. The Royal Society of Chemistry: Cambridge, UK, 2003.

134. Randles JEB. Kinetics of rapid electrode reactions. *Discussions of the Faraday Society* 1947, **1**(0)**:** 11-19.

135. Simon P, Gogotsi Y. Perspectives for electrochemical capacitors and related devices. *Nat Mater* 2020, **19**(11)**:** 1151-1163.

136. Elgrishi N, Rountree KJ, McCarthy BD, Rountree ES, Eisenhart TT, Dempsey JL. A Practical Beginner's Guide to Cyclic Voltammetry. *Journal of Chemical Education* 2018, **95**(2)**:** 197-206.

137. Shang NG, Papakonstantinou P, McMullan M, Chu M, Stamboulis A, Potenza A*, et al.* Catalyst-Free Efficient Growth, Orientation and Biosensing Properties of Multilayer Graphene Nanoflake Films with Sharp Edge Planes. *Advanced Functional Materials* 2008, **18**(21)**:** 3506-3514.

138. He Y, Bai Y, Yang X, Zhang J, Kang L, Xu H*, et al.* Holey graphene/polypyrrole nanoparticle hybrid aerogels with three-dimensional hierarchical porous structure for high performance supercapacitor. *Journal of Power Sources* 2016, **317:** 10-18.

139. Tian X, Tang K, Jin H, Wang T, Liu X, Yang W*, et al.* Boosting capacitive charge storage of 3D-Printed micro-pseudocapacitors via rational holey graphene engineering. *Carbon* 2019.

140. Chai Y, Li Z, Wang J, Mo Z, Yang S. Construction of hierarchical holey graphene/MnO2 composites as potential electrode materials for supercapacitors. *Journal of Alloys and Compounds* 2019, **775:** 1206-1212.

141. Bai Y, Yan Z, Kang L, Liu Z-H. Preparation and capacitance of V2O5/holey graphene hybrid aerogel electrode with high performance. *Journal of Alloys and Compounds* 2019, **780:** 792-799.

142. Zhao J, Zhang Y-Z, Chen J, Zhang W, Yuan D, Chua R*, et al.* Codoped Holey Graphene Aerogel by Selective Etching for High-Performance Sodium-Ion Storage. *Advanced Energy Materials* 2020, **10**(18)**:** 2000099.

143. Wang B, Jin F, Xie Y, Luo H, Wang F, Ruan T*, et al.* Holey graphene modified LiFePO4 hollow microsphere as an efficient binary sulfur host for high-performance lithium-sulfur batteries. *Energy Storage Materials* 2019.

144. Jiao X, Hao Q, Xia X, Yao D, Ouyang Y, Lei W. Boosting long-cycle-life energy storage with holey graphene supported TiNb2O7 network nanostructure for lithium ion hybrid supercapacitors. *Journal of Power Sources* 2018, **403:** 66-75.

145. Stolyarova SG, Koroteev VO, Shubin YV, Plyusnin PE, Makarova AA, Okotrub AV*, et al.* Pressure-Assisted Interface Engineering in MoS2/Holey Graphene Hybrids for Improved Performance in Li-ion Batteries. *Energy Technology* 2019.

146. Yang D, Xu B, Zhao Q, Zhao XS. Three-dimensional nitrogen-doped holey graphene and transition metal oxide composites for sodium-ion batteries. *Journal of Materials Chemistry A* 2019.

147. Liu X, Jiang L, Zhu Z, Chen S, Dou Y, Liu P*, et al.* Wet-chemistry grafted active pyridinic nitrogen sites on holey graphene edges as high performance ORR electrocatalyst for Zn-Air batteries. *Materials Today Energy* 2019, **11:** 24-29.

148. Seo W, White DL, Star A. Fabrication of Holey Graphene: Catalytic Oxidation by Metalloporphyrin-Based Covalent Organic Framework Immobilized on Highly Ordered Pyrolytic Graphite. *Chemistry – A European Journal* 2017, **23**(24)**:** 5652-5657.

149. Lacey SD, Walsh ED, Hitz E, Dai J, Connell JW, Hu L*, et al.* Highly compressible, binderless and ultrathick holey graphene-based electrode architectures. *Nano Energy* 2017, **31:** 386-392.

150. Lin Y, Moitoso B, Martinez-Martinez C, Walsh ED, Lacey SD, Kim J-W*, et al.* Ultrahigh-Capacity Lithium–Oxygen Batteries Enabled by Dry-Pressed Holey Graphene Air Cathodes. *Nano Letters* 2017, **17**(5)**:** 3252-3260.

151. Wang D, Dai R, Zhang X, Liu L, Zhuang H, Lu Y*, et al.* Scalable and controlled creation of nanoholes in graphene by microwave-assisted chemical etching for improved electrochemical properties. *Carbon* 2020, **161:** 880-891.

152. White DL, Burkert SC, Hwang SI, Star A. Holey Graphene Metal Nanoparticle Composites via Crystalline Polymer Templated Etching. *Nano Letters* 2019.

APPENDIX A

SUPERCAPACITOR PROPERTIES OF HOLEY GRAPHENE VS. PRISTINE GRAPHENE

Material	Surface area [$m^2 g^{-1}$]	Conductivity [$S m^{-1}$]	Capacitance [$F g^{-1}$]	Charge transfer resistance [Ω]	Energy density [$Wh kg^{-1}$]	Power density [$W kg^{-1}$]	Cycling life[a)]	Electrode density [$mg cm^{-2}$]
Holey graphene[77]	658 (471)	\	45 (40) at 3 A g^{-1}	\	12^{V} ($\sim 2^{V}$) SSC	\	96% @100,000	0.14–0.42
Holey graphene[42]	~600–700 (~500)	\	43 at 0.25 A g^{-1}	\	3.8–9.1 SSC	310–974 SSC	65% @2,000	30
Holey graphene[37]	\	\	226 (104) at 4 mA cm^{-2}	3.33 (4.54)	9.25–10.37 SSSC	1,388–4,166 SSSC	93% @5,000	\
Holey graphene[21]	750 (550)	\	330 (235) at 5 mV s^{-1}	5.5	124 (86) at 25°C; 140 at 60°C SSC	18.0 (17.5) at 25°C; 52.5 at 60°C SSC	90% @2,000	0.5
Holey graphene[36]	42.4	\	30^{V} at 0.05 mA cm^{-2}	\	2.43–4.24^{V} MSC	120–$21,840^{V}$ MSC	88.6% @10,000	\
Holey graphene[40]	763 (552)	1,786 (3,287)	251 (188) at 1 A g^{-1}	1.15 (5.58)	\	\	94% @ 6,000	0.86 g cm^{-3}
Holey graphene[92]	592 (520)	\	211 (142) at 0.5 A g^{-1}	\	\	\	99.9% @10,000	3
Holey graphene[28]	347 (~250)	0.124 (1.46)	110 or 165^{V} at 5 A g^{-1}	\	\	\	85.5% @ 7,000	1.5 g cm^{-3}
Holey graphene[22]	560.8 (254.6)	\	329 (208) at 0.5 A g^{-1}	\	\	\	\	\
Holey graphene[81]	261 (210)	\	253 (158) at 1 A g^{-1}	\	\	\	91% @50,000	0.54 g cm^{-3}
Holey graphene[39]	290 (250)	\	243 (180) at 0.1 A g^{-1}	\	43.1–117.3 HSC	100–19,700 HSC	81.7% @2,000	\
Holey graphene aerogel[79]	528 (305)	\	178 (151) at 0.2 A g^{-1}	\	\	\	\	1
Holey graphene hydrogel[34]	MB 1,330 (990)	2,030	283 (205) at 1 A g^{-1}	\	116 (77) or 86^{V} Organic SSC	\	94% @20,000	1.12 g cm^{-3}
Holey graphene framework[23]	830 (260); MB 1,560 (1,030); 810 after compression	1,000 (1,400)	310 (208) at 1 A g^{-1} in aqueous solutions; 298 at 1 A g^{-1} in $EMIMBF_4$/AN	\	112 or 79^{V} Aqueous SSC; 123 or 87^{V} Organic SSC	10^2–10^3 SSC	91% @10,000	10
Holey N-graphene[45]	446	0.028	318.3 at 0.5 A g^{-1}	0.4	60.5 SSC	900 SSC	98.4% @10,000	1.5–2.0
Holey N-graphene[41]	1,216 (630)	\	343 (296) at 0.3 A g^{-1}	4.8 (6.5)	\	\	>100% (~80%) @ 10,000	\
Holey N,S-graphene aerogel[29]	395 (183)	22.66 (12.43); 1,215 (865) compressed	807^{V} (556^{V}) at 1 mA cm^{-2}	0.19 (0.45)	0.409^{V} SSSC	102^{V} SSSC	95.4% @1,100	\

Holey B,N,P-graphene hydrogel[24]	980 (498)	39.7 (42.1)	362 (318) at 1 A g^{-1}	\	38.5 SSC	83,000 SSC	81.3% @50,000	10
p-phenylenediamine doped holey graphene[30]	67.32 (26.88)	3927 (4021)	300 (235) or 516^{V} (357.2^{V}) at 0.5 A g^{-1}	0.23	2.18–2.72^{V} FSSC	146.5–3,313.6^{V} FSSC	88% @12,000	\
p-phenylenediamine doped holey graphene[25]	98.34 (83.56)	24.2 (33.5)	375.5 (311.8) at 0.5 A g^{-1}	\	5.59–11.71 FSSC	249–20,110 FSSC	75% @10,000	\
Polyaniline@holey N-graphene[26]	\	\	746 (618) at 1 A g^{-1}	\	24.7 SSC	329.5 SSC	74% @2,000	0.8
Polyaniline@holey graphene framework[31]	185	\	730 or 1058^{V} at 0.5 A g^{-1}	\	26.5^{V} SSC	175.3^{V} SSC	81.5% @5000	1.45 g cm^{-3}
Polypyrrole@holey graphene aerogel[138]	278 (131)	\	418 at 0.5 A g^{-1}	2.0 (2.5)	\	\	74% @2,000	1.6
CNT@holey graphene[22]	\	\	557 at 0.5 A g^{-1}	\	\	\	90% @5,000	\
CoO/Co@holey graphene[139]	\	\	241.3 (136.6) mF cm^{-2} at 0.5 A g^{-1}	\	\	\	91% @11,000	\
MnO_2@holey graphene aerogel[140]	134.8 (39.7)	\	192.2 at 0.5 A g^{-1}	\	\	\	79% @5,000	\
V_2O_5@holey graphene aerogel[141]	417 (149) for HGA (GA); 76 (35) for composite	\	316 (268) for HGA (GA); 264 for composite	1.74	\	\	98% for HGA; 85% @1,000	1–1.5
RuO_2@holey graphene fiber[27]	\	\	693 or 1054^{V} at 2 mV s^{-1}	67.4	15.9–27.3^{V} FMSC	147.7–2,954.1^{V} FMSC	78.7% @10,000	1.52 g cm^{-3}
MoS_2@holey graphene fiber[38]	\	\	421^{V} (141^{V}) at 5 mV s^{-1}	\	4.1–8.2^{V} FMSC	40–2,000^{V} FMSC	92% @3,000	\
MXene@holey graphene[32]	68	1,770	438 or 1445^{V} at 2 mV s^{-1}	\	31.3–38.6^{V} SSC	206–8,245^{V} SSC	93% @10,000	1

Note:

[a)] Capacity or capacitance retention percentage at certain cycles (indicated by the value after @).

^{V} Volumetric properties: the originally denoted unit of g^{-1} and kg^{-1} should be replaced by cm^{-3} and L^{-1}, respectively.

ASC: asymmetric supercapacitor; SSC: symmetric supercapacitor; FSSC: flexible symmetric supercapacitor; MSC: micro-supercapacitor; FMSC: fiber-based micro-supercapacitor; SSSC: solid-state supercapacitor; HSC: hybrid supercapacitor.

APPENDIX B

METAL-ION BATTERY PROPERTIES OF HOLEY GRAPHENE VS. PRISTINE GRAPHENE

Material	Surface area [m^2 g^{-1}]	Conductivity [S m^{-1}]	Capacity [mAh g^{-1}]	Charge transfer resistance [Ω]	Warburg coefficient [Ω $s^{-1/2}$]	Ion diffusion coefficient [cm^2 s^{-1}]	Energy density [Wh kg^{-1}]	Power density [W kg^{-1}]	Cycling life[a)]	Electrode density [mg cm^{-2}]
Holey graphene[39]	290 (250)	\	170.4 (169.4) at 0.1 A g^{-1}; 117.0 (5.6) at 30 A g^{-1};	\	\	\	43.1–117.3 HSC	100–19,700 HSC	81.7% @2,000	\
Holey graphene[19]	15 (25)	10,000 (20,000)	819 (504) at 0.14 C	516 (551)	4,200 (9,100)	\	10^1–10^2 //Li	10^1–10^4 //Li	100% @1,000 at 26.6 C	0.2–0.3
Holey graphene[47]	84 (156)	5 (7)	365 (251) at 0.1 A g^{-1}	\	\	\	\	\	45% @3,000	1.23
Holey graphene[88]	457 (275) BET 945 MB	\	423 (164) at 0.1 A g^{-1}	37.4	\	\	\	\	95% @100	\
Holey Fe,N-graphene[83]	370.5 (202.5)	\	1255 at 0.1 C	33.07 (40.14)	1.09 (8.82)				75.1% (64.3%) @300	
Holey N-GO aerogel[142]	260 (74)	\	446 (153) at 0.1 A g^{-1}	\	\	\	\	\	40% @2,000	1.3
$LiFePO_4$@holey graphene[143]	183.1	25.83	1507[b)] at 0.1 C	8.75 (11.76)	\	\	\	\	78%@500	4.3[b)]
Co_3O_4@holey graphene[46]	130.1	\	631 at 10 A g^{-1}; 1015 at 0.2 A g^{-1}			\	352.5 //LFP	1369.6 //LFP	89.6% @100	
$TiNb_2O_7$@holey graphene[144]	181	\	276 at 0.05 A g^{-1}				83.6 //AC	237.7 //AC	90.2% @3,000	
MoS_2@holey graphene[145]	\	\	596 at 0.1 A g^{-1}; 912 at 0.1 A g^{-1} with super P; 1200 at 0.5 A g^{-1} after 1,000 cycles with super P	71.8	\	\	\	\	133% @1,000	\

$Li_4Ti_5O_{12}$@holey graphene[44]	154.2	\	200 or 161[V] at 0.035 A g^{-1}	17.1 (71.1)	16.4 (129.6)	188 (3.02) × 10^{-12}	\	\	84% @1,000	1.1 g cm^{-3}
$NiCo_2O_4$@holey N-graphene[146]	\	\	510 (221) at 0.1 A g^{-1}	63 (128)	\	\	\	\	85.7% @500	1
Mo_2C@holey N-graphene[84]	70.8 (29.2)		1221 at 0.1 A g^{-1}	314.5					58% @300	
Nb_2O_5@holey graphene aerogel[43]	83		139 at 10C						90% @10,000	
Fe_3O_4@holey graphene aerogel[118]	204 (242)	\	1107 (862) at 0.1 A g^{-1}	33.42 (82.38)	\	1.02 × 10^{-10} (2.35 × 10^{-12})	\	\	85.4% @100	\

[a] Capacity or capacitance retention percentage at certain cycles (numbers after @).

[b] Based on the weight of sulfur.

//AC: pair with active carbon; //LFP: pair with lithium iron phosphate.

APPENDIX C

HOLEY 2D MATERIAL MANUFACTURING METHODS AND THE PROPERTIES OF THE OBTAINED IN-PLANE HOLES

Treatment	Hole-formation mechanism	Dry/Wet	Size /nm	Pattern
Solution-based etching	Oxidative etching: H_2O_2 etching[22, 23, 24, 25, 26, 27, 28, 29, 30, 31, 32, 34, 40, 43, 44, 45, 47, 54, 56, 62, 64, 118, 138, 139, 141, 143, 146, 147]	W	2–3[34] 2–5[24] 2–4[54] 1–3.5[146] 2–10[47] 2[118]	Random
	Oxidative etching: HNO_3 etching[19, 51, 73]	W	7–600[19] 2–5[51] 0–90[73]	Random
	Sulfate radical etching[36]	W	1–10	Random
	Lithography: COF lithography[148]	W	4–50	Periodic
Calcination	Oxidative etching: O_2 etching[42, 48, 49, 52, 57, 58, 77, 78, 142, 149, 150]	D	5–10[77] 10–20[49] 5–20[58]	Random
	Catalyzed etching: AgNP-catalyzed O_2 etching[37, 86, 87, 88]	D	10^1–10^2[86] 5–150[87]	Random
	Oxidative etching: Fe_2O_3 etching[80]	D	2–50	Random
	Oxidative etching: SnO_2 etching[81]	D	5–10	Random
	Oxidative etching: ZnO etching[85]	D	1.5–5	Random
	Oxidative etching: CoO etching[82]	D	\	Random
	Oxidative etching: $FeN_{0.056}$ etching[83]	D	20–30	Random
	Oxidative etching: MoO_2 etching[84]	D	2–50	Random
Microwave-assisted etching	Oxidative etching: O_2 etching[61]	D	2–5	Random
	Oxidative etching: H_2O_2 etching[151]	W		Random
	Oxidative etching: $KMnO_4$ + HNO_3 etching[74]	W	\	Random
UV irradiation	O_2 etching[70]	D	20	Random
	Catalyzed etching: AuNP-mediated, photocatalyzed OH• etching[76]	W	5–100	Random
	Catalyzed etching: Templated, ZnO-mediated, photocatalyzed etching[71]	D	200	Random
Annealing	Catalyzed etching: Cu-catalyzed hydrogenation[67]	D	Nanoscale	Random
Ball mill-assisted etching	KOH etching[41]	W		Random
Hydrothermal synthesis	Oxidative etching: O_2 etching[79]	W	2–5	Random
O_2 plasma etching	Lithography: Templated O_2 plasma etching[18, 65, 68, 69] Lithography: COF lithogrpahy[152]	D	17.7–31.9[18] 67[69] 0.63[65]	Periodic
Rapid heating	High-energy shock: Local pressure damage[21, 92]	D	10–250[98] 50–100[23]	Random
Focused electron beam bombarding	Focused electron beam[93]	D	2–40	Single
CVD	Templated assembly[59, 60]	D	10–15	Random

APPENDIX D

LIST OF PUBLICATIONS DURING THE STUDY TOWARDS THE DOCTORAL DEGREE

Journal Articles

1. Dini Wang, Rui Dai, Xing Zhang, Lei Liu, Houlong Zhuang, Yongfeng Lu, Yan Wang, Yiliang Liao, and Qiong Nian. 2020. "Scalable and controlled creation of nanoholes in graphene by microwave-assisted chemical etching for improved electrochemical properties." Carbon 161:880-891. doi: https://doi.org/10.1016/j.carbon.2020.01.076.

2. Ling Ding, Huan He, Jin Zhou, Dini Wang, Qiong Nian, Shiqian Li, Shihui Qian, Wenbing Li, Cui Liu, and Zhengyong Liang. 2021. "Preparation of high-quality graphene oxide-carbon quantum dots composites and their application for electrochemical sensing of uric acid and ascorbic acid." Nanotechnology 32 (13):135501. doi: https://doi.org/10.1088/1361-6528/abd12a.

3. Rui Dai, Meng Wang, Dini Wang, Zengrong Hu, Matthew D. Green, and Qiong Nian. 2020. "Understanding mechanical behavior of metallic foam with hollow struts using the hollow pentagonal dodecahedron model." Scripta Materialia 182:114-119. doi: https://doi.org/10.1016/j.scriptamat.2020.03.001.

4. Zengrong Hu, Dini Wang, Changjun Chen, Xiaonan Wang, Xiaming Chen, and Qiong Nian. 2019. "Bulk titanium–graphene nanocomposites fabricated by selective laser melting." Journal of Materials Research 34 (10):1744-1753. doi: https://doi.org/10.1557/jmr.2019.65.

5. "Manufacturing holey two-dimensional materials: a review" in preparation.

6. "Growth of atomic vacancies into nanoholes on graphene oxide during holey graphene manufacturing" in preparation.